Génération dynamiques de formes spatiales de vibrations en utilisant la décomposition modale : application à la surface haptique

Ehsan Enferad

Université de Lille

L2EP Laboratoire d'électrotechnique et d'électronique de puissance de Lille

Thèse présentée pour obtenir le grade de docteur

Université de Lille

Faculté des Sciences Et Technologies
École doctorale Sciences pour l'ingénieur (SPI 072)

Discipline : Génie Électrique

Dynamic Spatial Vibration Form Generation Using Modal Decomposition

Application to Haptic Surface

Par : **ENFERAD Ehsan**

Membres du jury:

Rapporteur : Skandar BASROUR, Prof. Université Grenoble-Alpes

Rapporteur : Nazih MECHBAL, Prof. Ensam Arts & Métiers Paris tech

Examinateur : Eric SEMAIL, Prof .Ensam Arts & Métiers Paris tech

Encadrant : Christophe GIRAUD-AUDINE, MCF, Ensam Arts & Métiers Paris tech

Directeur : Frédéric GIRAUD, MCF HDR, & Université de Lille

Examinatrice : Christine PRELLE, Prof. UTC Compiégne

Date de soutenance : 12 November 2018

ABSTRACT

Currently, the haptic interaction on screens is visual, although it has been demonstrated that tactile feedback enhances the experience and improves the productivity by relieving the visual load. Most of the haptic feedback technologies available today are based on global stimulation which limit their use for collaborative device interfaces or control panels for instance. This work address this problem by developing a method that uses elastic waves to realize localized out of plane bending deformations on a thin plate. In this study modal decomposition is proposed to realized controlled local deformation (haptic stimulation). The approach only necessitates the knowledge of the modal behavior of the structure which can be extracted from finite elements analysis or identified. By this prior knowledge arbitrary shapes can be defined using its projection on the mode shapes. For practical considerations, a model reduction criterion is proposed as well. A method to define the driving forces is developed which consists in setting the modes transients in the modal space. Actual voltages to be applied to the actuators are then deduced. The methodology is validated on several demonstrators with different geometries. The ability to control in open loop simultaneously over ten modes using a single actuator is validated by focalizing a predefined shape at different locations. To avoid voltage limitation, a prototype with several actuators was realized to create more elaborated shapes with higher velocities. The results confirm the versatility of the method. The robustness towards identification uncertainties and truncation is evaluated, and improvements with regards to identification errors and transient control in relation to the haptic experience are proposed. Preliminary haptic tests, with contrasted and localized velocity fields are presented, showing tangible results as for the differentiation and the localization of the stimuli by the user.

Génération Dynamiques de Formes Spatiales de Vibrations en Utilisant de la Décomposition Modale:

Application à la Surface Haptique

RÉSUMÉ

Actuellement, l'interaction haptique est visualisée, il a été démontré que le retour tactile améliore l'expérience et améliore la productivité en allégeant la charge visuelle. La plupart des technologies de retour haptique disponibles aujourd'hui sont basées sur une vision globale du monde. Ce travail aborde ce problme en développant une méthode utilisant des ondes élastiques pour réaliser des déformations de flexion planes hors plan sur une plaque mince. Dans cette étude, la décomposition modale est proposée pour obtenir une déformation contrlée localement (stimulation haptique). L'approche nécessite seulement la connaissance du comportement modal de la structure. Cette connaissance peut tre définie en utilisant sa projection sur les formes de mode. Pour des considérations pratiques, Une méthode pour définir les forces motrices dans l'espace modal. Les tensions réelles à appliquer aux actionneurs sont ensuite déduites. La méthodologie est validée sur plusieurs démonstrateurs de géométries différentes. La possibilité de contrler lun des deux modes de fonctionnement à l'aide dun seul actionneur est validée en focalisant une forme prédéfinie à différents endroits. Pour éviter la limitation de la tension, un prototype à plusieurs actionneurs a été développé avec plus de vitesses. Les résultats confirment la polyvalence de la méthode. La robustesse face à l'identification des incertitudes et de la troncature est évaluée et proposée. Des tests haptiques préliminaires, avec des champs de vitesse contrastés et localisés sont présentés, montrant des résultats tangibles pour la différenciation et la localisation des stimuli par l'utilisateur.

Contents

List of Symbols and Abbreviations

$\boldsymbol{\epsilon}$	Strain Matrix	1
ϵ_{ij}	Strain component in i and j direction	1
$\boldsymbol{\sigma}$	Stress Matrix	$kg/(ms^2)$
σ_{ij}	Stress component in i and j direction	$kg/(ms^2)$
$\boldsymbol{C}$	Elastic stiffness matrix	kg/s^2
C_{ij}	Elastic stiffness coefficient in i and j direction	kg/s^2
$\boldsymbol{S}$	Elastic compliance (flexibility) matrix	s^2/kg
S_{ij}	Elastic compliance (flexibility) coefficient in i and j direction	s^2/kg
E	Young's modulus	$kg/(ms^2)$
G	the shear modulus	$kg/(ms^2)$
ν	the Poisson ratio	1
$x \quad y \quad z$	axis of cartesian coordinate system	1
$u_x \quad u_y \quad u_z$	displacement of the beam in x, y and z direction	1
$p_{(x_p,y_p,t)}$	External Force (Piezoelectric Force) applied in point $(x_p \quad y_p)$	N
A		n
C_p	Capacitance of PT	F
D	Flexural Rigidity	$Pa.m^4$
d_E	External Damping of Beam	n
i_{pt}	Current of PT	A
L	External inductor included to the PT drive circuite	H
N_{mm}	Number of modelled modes	
$\boldsymbol{w}_{(x,y,z)}$	Transverse deflection field of beam	m
$M_{x,t}$	Bending moment of beam	$kg.m/s$

$I_{(x)}$	Second moment of beam	
ρ	Density of beam or plate	kg/m^3
V	Shear force	N
ϕ	Rotation of cross section	
κ	Shear coefficient	
$I_{(x)}$	Second moment of beam	
ρ	Density of beam or plate	kg/m^3
V	Shear force	N
ϕ	Rotation of cross section	
κ	Shear coefficient	
γ	Electromechanical coupling ratio	N/v
$q_{(x,y,t)}$	External (Focused) transverse force density	N
R_p	Resistance of PT	Ω
$v_{p(t)}$	Voltage on the PT	v
$v_{in(t)}$	Excitation voltage of PT supplied by a voltage source	v
$\boldsymbol{w}_{(x,y,t)}$	Out of plane displacement on beam or plate	m
x_p, y_p	Coordinates of PT location	m
$\varphi_{k(x,y)}$	k^{th} mode shape by Gram-Schmidt	
$\varphi^{\dagger}_{k(x,y)}$	k^{th} Orthogonalized mode shape by Gram-Schmidt	
$\overline{\varphi^{\dagger}_{k}}$	k^{th} Normalized orthogonalized mode shape by Gram-Schmidt	
ODE	**O**rdinary **D**ifferential **E**quation	
DOF	**D**egree **O**f **F**reedom	
I/O	**I**nput **O**utput	
FEM	**F**inite **E**lement **M**odel	
FE	**F**inite **E**lement	
TR	**T**ime **R**eversal	
PT	**P**iezoelectric **T**ransducer	
FRF	**F**requency **R**esponse **F**unction	

General Introduction

Past few years have seen the emergence of the capacitive touchscreens to interact with computers, and they are now introduced into a lot of consumer products like smartphones, tablets, dashboards of car, vending machines. And they are cost-effective replacement solutions to physical buttons or knobs in these applications. However, because a touchscreen is always felt as a flat, smooth and hard surface, users receive no feedback from this surface when they push on virtual buttons and knobs as opposed to the real ones. Therefore, most of users actually rely on the visual feedback to operate their machines, leading to two major issues using touchscreens. First, users are less precise in pointing tasks, like writing text with a virtual keyboard, generating frustration and increased task completion time. Second, they cannot remove their eyes from the display, a major issue in automotive applications. This is why, the introduction of capacitive touchscreens has now reached a plateau, and solution have to be found to solve the aforementioned issues.

In this context, some researchers propose to synthesize the physical interaction with a touchscreen by using haptic stimulators. In fact, existing devices can change how we perceive the surface of a touchscreen, by modifying the contact forces between the users fingerpulp and the surface. They can render it textured as if a grating pattern was engraved, when the finger slides on the surface. Others can achieve localized stimulation of the finger with a set of actuators located at the periphery of the display. The advantage is that there is no occlusion of the actuators on the active area of the display, the mechanical deformation of the surface being conveyed by the touchscreen itself with vibration.

To be effective, a tactile stimulator has to provide a calibrated stimulation which is felt by a large number of users. To match the industrial requirements, it also has to be robust besides the environment factors, among which we have the discrepancies in the size of the material, as well as the effect of the finger on the vibration. However, so far,

devices which can produce localized tactile stimulation without occlusion need specific implementation to adapt to the environmental factors, or have lack of performances. Therefore, this thesis aims at proposing a solution to focus the vibration on a spot on the touchscreen in order to produce localized haptic feedback. We make the hypothesis that closed loop control will be beneficial to increase the robustness. Therefore, we propose the concept of the modal decomposition, which consists in projecting a predefined vibration pattern onto the natural vibration modes of the touchscreen. By implementing the closed loop control of all the required modes, the performances of the system will be time independent. Moreover, since the method relies on the modal deformation of the surface, which depends more on geometry than environment, the performances will be guaranteed.

The main difficulties of the thesis is to be able to focus the energy of vibration at a precise location and at a precise focusing time, with a sufficiently high amplitude to generate the haptic feedback. The thesis is then organized into five chapters. The first chapter is an introduction to the science of haptic, and presents the main examples of haptic stimulators. We introduce the methodology followed in this thesis and we detail the main objectives. In the second chapter, we present the modal projection of a given deformation shape on a surface. For the purpose of simplification, the method is developed and illustrated on a simple beam, but it can be applied to rectangular plates as well. In particular, we show that a limited number of modes is required to synthesize the vibration form. We also present the function which describes the evolution of the voltage in order to obtain the required modal decomposition. The methodology needs the identification of parameters and the vibrating modes. The third chapter details our methods used in this work in the frequency domain. Specifically, the algorithm which create an orthogonal base is presented and applied on the beam.

The experimental validation of the modal decomposition is described in the chapter four. We extensively study the effect of the shape of the vibration pattern on the number of required modes to be controlled. The results of the experiment are compared with theory. Here, the control of the modes is achieved in open-loop, paving the way toward the closed loop control in future work. Finally, an experimental psychophysical study has been conducted in the last chapter. To calibrate the stimulation, and to come closer to the case of a single stimulation spot on the surface, the dynamic of the transient and post-transient of the modes are modified.

Chapter 1

Introduction

Since 1965 researchers have been trying to include one more dimension to Human Machine Interfacing by providing touch feeling with force feedback to the user. This new branch of science is called Haptics, from the Greek origin name (haptesthai), which means '*of or relating to the sense of touch*'. Haptics refer to the science of mutual sensing and manipulation of surrounding objects and environments through the sense of touch and it has brought different branches of the science like as; psychology, neurophysiology, biomechanics, electrical engineering and computer science, in order to study the human touch and force feedback with machine. The product of haptics science are haptic interfaces.

The haptic interfaces enable users to touch the items which are virtual or distant. This would be clearer if haptic interfaces are compared with commonplace visual interfaces. In visual interfaces, an image of real or imaginary content is generated and displayed on screen or transmitted from one computer to another. In haptic interface a digital/analog simulation of a surface is detected and a virtual model of the surface is stimulated to the finger of users. The stimulation of haptic interface can be related to real object/surface or imaginary object/ surface. Like as visual interface, the simulated object can be transferred from one computer to another.

Integration of sense of touch to the computer and digital world, can cause the experience become more participatory and more immediate, more tangible and more similar to real world. Moreover such integration can open a new chapter in front of science and technology. There is progressive research in haptics fields and because of wide scientific background, a categorization of study fields is very practical to implement. The broad multidisciplinary haptic field is divided into four categories; human haptics, machine

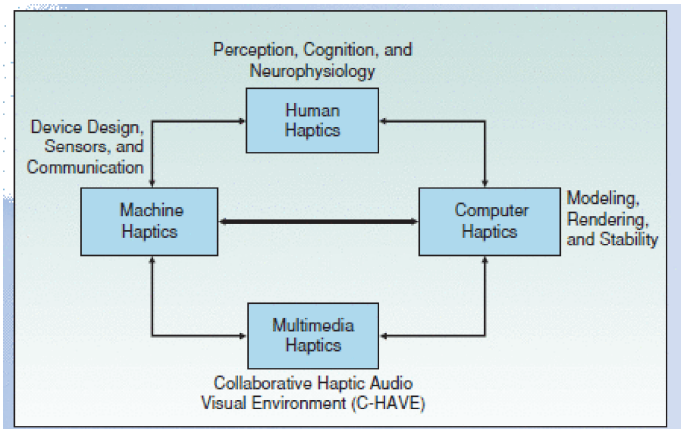

FIGURE 1.1: Interrelation of haptic science branches [1].

haptics, computer haptics and multimedia haptics. The general overview of haptic subfield and their interaction is illustrated in Fig. 1.1. All haptics subfields are briefly described in coming subsections.

1.1 Haptic Interface

1.1.1 Human haptic

The human haptics is referred to science of human sensing through tactile sense. This branch mostly includes neuroscience and psychology where the human haptic system is investigated by its functionality, starting from receptors on the hand to information analysis on the brain and associated psychological behaviors. The human sensorimotor loop and human perception of sense of touch are two main concerns of human haptics. The human haptics is subdivided into four main subcategories [1]; mechanical, sensory, motor and cognitive.

- The mechanical component is the hand and arm which in overall contain more than 28 degrees of freedom
- The sensory system includes all type of mechanoreceptors in the hand and the nerves ending to them, joints and tendons (the afferent neural network to the central nervous system)
- The brain is the cognitive subsystem of human haptics which analyze and perceives the information of mechanoreceptors and issues corresponding motor commands to activate the muscles. It is responsible for psychological conception of touch

- The motor subsystem comprises contractile organs by which movement of various organs and parts are achieved

1.1.2 Machine haptic

Machine haptics deals with designing, building and developing Haptic Interfaces which are in direct contact to human body. The haptic interfaces have bidirectional communication with human body. They receive the location information of body (finger) then render appropriate haptic signals and send them to human nervous system. Machine haptics mostly deals with mechanical system whose input is finger location (more generally body location) and its output is haptic information (more generally haptic signals to mechanoreceptors). The challenging issue in designing haptic interfaces is to develop a machine which sends well perceivable haptic signals to human mechanoreceptors. Additionally, machine haptics have to overcome this challenge with existing limits in computer science and engineering. Hence, machine haptics plays key role in linking both neuroscience and computer science (engineering) aiming to make appropriate human machine haptic communication. Systematically, haptic interfaces consist of two parts [2], Haptic sensor (the input of system) and Haptic display (the output of system).

- **Haptic sensor** are devices which are utilized to receive the position, motion and force feedback of finger or part of human body which is in contact with Haptic display. The use of haptic sensor is parallel to the use of keyboard, mouse or touch screen in the computer.
- **Haptic displays** are devices or actuators which generate the simulation of touch feeling. In other term, haptic displays render the haptic image on a surface tangible by human. The use of Haptic display is parallel to computer screen and audio speaker.

Indeed haptic interface is the place where human and machine exchange mechanical energy. Fig. 1.2 illustrates the virtual human-machine interfacing in haptic. As it is seen in this figure, the mid-point is the haptic display where human gets in touch with machine. The left side is human and the right side is machine. In this haptic system, at first haptic interface get feedback of location of the hand by using sensors, then the input signal for machine haptic is analyzed and sent to the process in computer haptic. The appropriate haptic signal is generated in computer haptic section and is sent to the actuator in haptic interface , and consequently related haptic image is

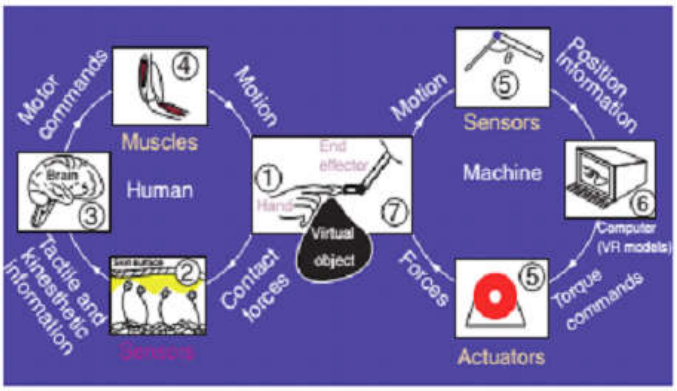

FIGURE 1.2: Human-Machine haptic interaction [3].

rendered on the haptic display. Human fingers recognize this haptic signal thanks to the mechanoreceptors existing under the hand skin. The mechanoreceptor signals are sent to the brain. After information analyze in the brain the motion command are sent from mind to arm muscle.

1.1.3 Computer haptics

The computer haptics is the programming area of haptics research where algorithms and softwares are developed in order to generate and render the touch signals. Likewise what is happening in visual interface of computer where the software science is used to function machine to output visually understandable photos, the same work is done with computer haptics to the finger and sense of touch. Meanwhile, the computer haptics branch is responsible of making the appropriate connection between visual interface and haptic interface for the sake of more realistic interfacing of touch and vision. Since haptics information signal are rich, hence the main challenges of this field is processing of information [1], latency and bandwidth for haptic teleoperation, for instance.

1.1.4 Multimedia haptics

Multimedia haptics integrates haptic interface with visual or audio feedback. The objective is to give more realistic feeling to user by giving visio-haptic, audio-haptic or both of them. Indeed, advances in neuroscience point out complex interaction between auditory, visual, haptic processings. This suggests that a deep immersion into virtual reality should take into account this multi-modal interaction [4].

1.2 Human sense of touch

Skin is the largest sensory organ of human, which has surface area of almost $1.6m^2$ and contains variety of receptors. Human recognize the surface of objects by tactile information like as pressure, vibration and temperature of the object's surface.

Since the aim of this thesis is to design haptic display with effective and robust human-machine communication, consequently, in this section, the human tactile sensory system or more precisely the mechanoreceptors are investigated. Mechanoreceptors afferent neu-

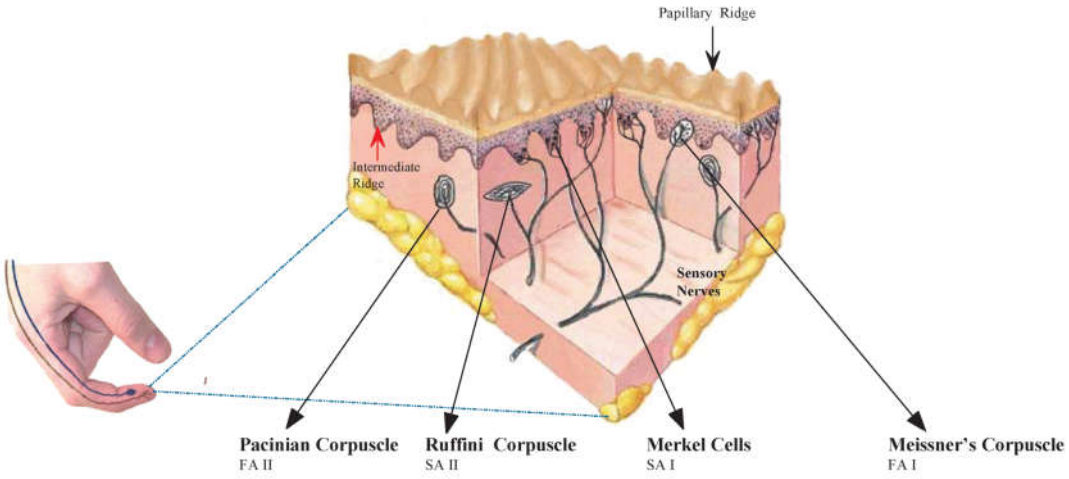

FIGURE 1.3: Four type of mechanoreceptors on the human skin [5].

rons are responsible for the sense of touch in human being and most of the mammals. The neuroscientists categorize these mechanoreceptors afferents into four categories; Slowly Adapting Type 1 (SA1), Slowly Adapting Type 2 (SA2), Rapidly Adapting (RA) and Pacinian (PC). Fig. 1.3 shows the four different mechanoreceptors and their location on the skin. Each of these neurons receptors respond differently to cutaneous deformation and motion [6].

1.2.1 Slowly Adapting Type 1 Afferents

The SA1 afferents end in Merkel cells. The Merkel cells have simple structure which is placed in the basal layer of the epidermic and surrounds ending of the SA1 afferent fiber, Fig. 1.4. Merkel Cells, also called Tactile Disc, respond to sustained indentation with slowly adapting discharge. They innervate the skin with 100 per cm^2 at the fingertip. Moreover, They have precise spatial resolution whereby each SA1 afferent can resolve spatial details of $0.5mm$. Due to their selective sensitivity and spatial resolution.

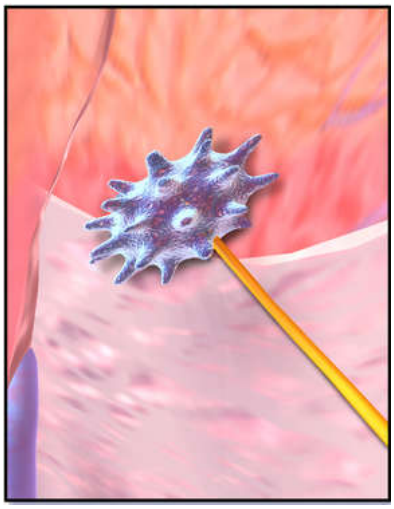

FIGURE 1.4: Slowly Adapting Type 1 Afferents (Merkel Cells) [7]

Briefly, SA1 afferent are responsible for form and texture perception [6]. Another feature of SA1 afferents is their linear behavior to skin deformation. Over a wide range of indentation with at least $1.5mm$ depth on the skin, they respond with a linear discharge rate. Because of their linear responsiveness to strain energy density, they detect the curvature of objects very accurately, and their response is independent with the applied force. SA1 receptive field grow minimally with indentation depth increment. They are ten times more sensitive to dynamic than to static stimuli and up to $80mm/s$ increase of scanning velocity, the spatial resolution of SA1 is affected minimally. This means that human haptic spatial pattern recognition is invariant up to at least $80mm/s$. Finally, SA1 are much more sensitive to texture when the finger is scanning the surface than when it is stationary. Finally the SA1 presents invariant responses to repeated skin indentation, which enables human to discriminate surface form [6].

1.2.2 Slowly Adapting Type 2 Afferents

The SA2 Afferent (Ruffini corpuscles) are the least innervated in the skin in comparison to other afferents, Fig. 1.5. They are six times less sensitive to skin indentation while they are $2-4$ times more sensitive to skin stretch. They detect skin stretch even better than SA1 afferents. The SA2 afferents exist in human hand while these receptors do not exist in the monkey hand [8]. This is probably the reason why the SA2 afferents have not been studied in deep.

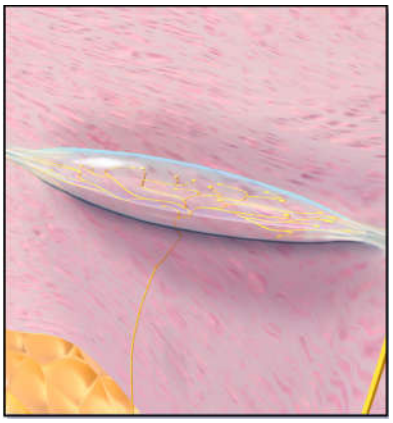

FIGURE 1.5: Ruffini Corpuscles [9]

1.2.3 Rapidly Adapting Afferents

Meissner afferents, so called Rapidly Adapting afferents (RA), innervate on the skin with density of 150 per cm^2, Fig. 1.6. They are very sensitive to dynamic skin deformation, four times more sensitive than SA1 afferents, while RA afferents are insensitive to static skin deformation. RA afferents respond uniformly to the stimuli over their entire receptive field $3-5$ mm in diameter, which cause them to resolve spatial information poorly. In spite of their poor spatial acuity, RAs present robust response to local events such as slip. Due to the wide and uniform sensitivity of RA afferents, they transmit a robust neural image to skin motion. Meissner afferents are more responsible to detecting slip between skin and touched objects, they are the most effective afferents in detecting sudden forces on the skin among all four mechanoreceptor afferents, hence they are the essential feedback sensors for grip control. RAs are insensitive to static force as well as low frequency vibration. As comparison, RA has greater sensitivity with poor spatial resolution while SA1 has less sensitivity with higher spatial resolutions.

1.2.4 Pacinian Corpuscles Afferents

PC afferents are large with 70 layers of onion-like structure, Fig. 1.7. They are sensitive to deformations in nanometer range. The layers play mechanical filter role to stop low frequency stresses and strains which provides protection to highly sensitive PC receptors. The PC afferents are distributed throughout the palm and fingers with density of $350-800$ per cm^2. Their extreme sensitivity can detect $10nm$ vibration on the skin, while they do not have precise spatial resolution.Another feature of PCs are their intensive filtering behavior in low frequency stimuli which is nearly $60dB$ per decade.

FIGURE 1.6: Meissner Corpuscle [10].

The PC population is responsible for the precision of high frequency stimuli. They have principal role in perception of distant event through an object held in the hand.

FIGURE 1.7: Pacinian Corpuscles [11].

When mechanoreceptors are activated, they transmit signals to the brain. By stimulating the human skin to induce tactile perception, haptic displays provides possibility of virtual sense of touch. Therefore, the next section of this chapter describes particular haptic displays.

1.3 State of Art of Haptic Displays

For creating haptic display, to date, variety of technologies has been developed which can convey tactile information to user [12, 13, 14, 15]. One can categorize these haptic

interfaces into two main categories; global stimulation and local stimulation regardless of their functionality.

1.3.1 Global Stimulation Haptic Displays

These types of haptic displays generally refer to haptic surfaces. In these interfaces, the haptic feedback is generated in whole display whereby all parts of display deliver almost the same sense of touch at the same time. These devices are designed to interact only with one finger at the same time, that is why there are called single touch haptic display as well. This section will review some of these haptic displays.

1.3.1.1 Lateral Force Modulation

This technology involves the lateral movement of the mechanical structure for the purpose of generating haptic sensation. The haptic display (the mechanical structure) is displaced using a piezoelectric disk bender actuator. The principal idea of lateral force haptic display comes from the fact that, in daily life, human obtain haptic perceptual information such as roughness, shape, text and etc. by sliding finger over the object. This fact was the inspiration of designing lateral force modulation.

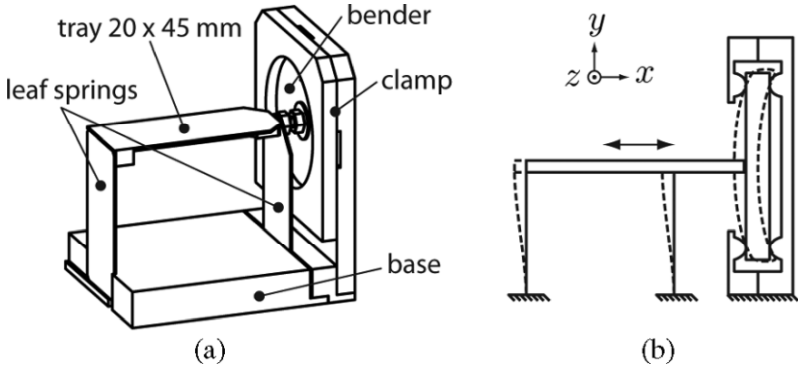

FIGURE 1.8: Schematic of lateral force modulation haptic display [16].

The initial prototype was manufactured using an aluminium beam [16]. It was operated in a causality inversion process of recording force and stimulating the displacement. In first phase, different type of texture has been attached to the tray (shown in Fig. 1.8.a) and a user is askedd to slide his finger on the tray with the attached texture.The signal of the lateral force between the finger and the textile was recorded by a disk bender which is located at the side of the tray (is seen in Fig. 1.8.b). In the second phase, the texture was unattached from the tray. The recorded force signal is applied to the

bender, which then works as an actuator and virtual stimulation of the haptic feeling is regenerated.

1.3.1.2 Friction Modulation Interface

Recently, ultrasonic haptic interfaces are considered as a potentially commercial candidate for future haptic market. In these type of haptic interfaces a set of transducers (typically piezoelectric transducers) are used to generate vibration on a solid surface (typically thin plates). The transducers are laminated to the haptic display (plate) and are controlled via electric signals.

The principle of friction reduction modulation interface is to excite the mechanical structure of a plate at one of its resonance vibration modes. Such vibration causes significant variation of friction between finger and plate. The friction variation of solid surface using this technique has been discovered and well explained by Watanabe et al [17] and friction modulation by ultrasonic wave has been well analyzed and prototyped by Biet et al [18] in L2EP laboratory. Fig. 1.9 represents the schematic of a solid surface with piezoelectric actuators. As it is seen in this figure, the piezoelectric actuators are small and they can be located in a pattern on the surface far from the touch area which facilitate the integration of haptic display and video display. Thus, this technology provides a good facility for designing low consumption embedded haptic displays. So far significant research has been done based on developing haptic display using ultrasonic vibration in L2EP[1] Laboratory. The surface friction is controlled by the finger position on the surface [19], therefore, the lateral forces can be modulated and different texture feeling are simulated [20]. Recently a multitouch approach has been investigated by Ghenna et. el [21] [22] using friction reduction modulation technique too.

The technologies to create global stimulation on tactile display is now very well developed. They can be used for texture simulation for example. However, by principle they cannot be used to render details without motion of the finger tip. This is why, we now present local stimulation haptic displays which can produce stimulation in a localized area.

[1] Laboratoire d'Electrotechnique et d'Electronique de Puissance (L2EP), Lille, France

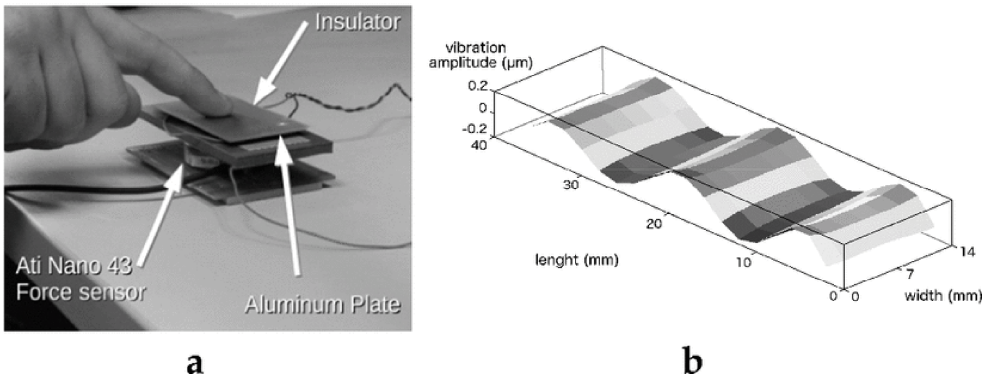

FIGURE 1.9: A. Piezoelectric based Ultrasonic haptic display B. Vibration waves on surface of ultrasonic haptic display [20]

1.3.2 Local Stimulation Haptic Displays

Local stimulation haptic displays are capable of generating haptic feeling in a small area on the finger pulpe. This section is dedicated to review some of these technologies.

1.3.2.1 Pins Array

Pins-Array is a local haptic display on which a matrix of pins have been manufactured side by side. The pins have the capacity to control the vertical position of pins. There are number of actuators and technics to create pins array haptic display, and below some of them are presented.

A pneumatic braille haptic pulse display has been fabricated and psychophysically evaluated [23]. In this haptic display, human finger is in contact with balloons which are inflated with pneumatic pressure. A key issue in designing pneumatic haptic display is the mass and size of pneumatic actuators and the challenge is to minimize them. Therefore, this type of braille haptic displays suffer from low density of the tactile feedback. The functionality of this pneumatic device is based on the pressure control of the balloons, independently of each other.

Another technology for realizing haptic display is Shape Memory Alloys (SMA) based actuators [24]. SMAs are smart materials, used to realize micro actuators in microelectromechanical system. They have quite high energy density compared with other smart material which cause them to achieve high force and displacement in low volume. The bistable SMA thin-film actuators are used to manufacture SMA haptic displays. Their function principle is like when a bucked metallic foil with two stable state (down and up) is switched to one of this position, it remains stable at that position till an external force

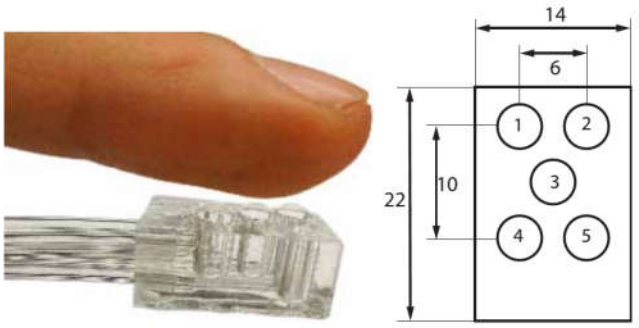

FIGURE 1.10: Tactile pulse display rendering a diagonal line. b) Balloon arrangement (distances in mm) [23]

changes its position to opposite state (as it is illustrated in Fig. 1.11). The design of the actuator consists of two main parts; a bucked thin film which is composed of active SMA layer, and a passive metal carrier layer providing the two-way actuation behavior. The actuator can be switched up or down by implementing heat pulses to the composite either by electric current or by heat flow from the environment. The actuation behavior of SMA can be detected by skin and finger's mechanoreceptors. They can operate in frequency range of up to 100 Hz in order to send haptic signals to receptors [25].

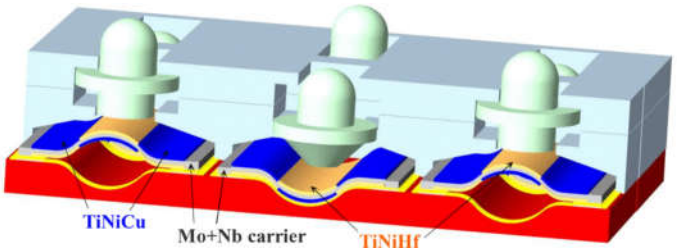

FIGURE 1.11: Example of an array of bistable thin-film actuators for haptic display applications. The actuator design for bistable SMA is based on a buckled thin-film composite. Thin-film actuators in the up/down switching positions are shown, as well as movable pins of the haptic display [24]

ElectroaActive Polymers (EAPs) also have been utilized for designing haptic displays. One of the most interesting EAP is Dielectric Elastomer Actuator (DEA) with lightweight and high energy efficiency. The functionality of DEA are similar to electromechanical transduction of two plate capacitors. When a voltage is applied to the electrodes, the elastomer is expanded in lateral direction and compressed in the thickness direction. Thus, due to stored electric charges in the surface, the actuation is generated. Schematic of DEA is presented in Fig. 1.12. As it is seen, the device is constructed by a frame with a rigid coupling and a DEA film. When the voltage on electrodes is off (left side Fig. 1.12) the actuator is under pretension. By applying voltage on electrodes, the actuator contacts toward the thickness direction. Consequently the pretension is reduced as a

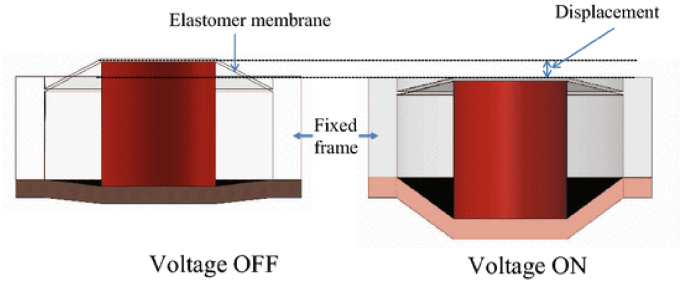

FIGURE 1.12: Operational principles of Dielectric Elastomer Actuator [26]

result of actuator expansion and the coupling moves down. This movement of DEA is transferred to the haptic display and touch spot. The high voltage input for driving DEA is a critical disadvantage of using these actuators in haptic displays [26]. While some researchers have embedded DEA in such a way that reduces the electrical damage concern to the user [27].

Streque et al [28] have presented a Micromagnetomechanical system for haptic actuation . This haptic actuator is an array of microactuators based on membrane deflection. The membrane is made of poly (Dimethyl-Siloxane), and a 4×4 prototype of the actuator has been tested [29]. The configuration is presented in Fig. 1.13. The design of this haptic microactuator is made of two major parts: a Poly Dimethyl-Siloxane Membrane (PDMS) which holds micromagnet in central location, and a support holding a miniature Copper coil which is fixed underneath the magnet. This haptic actuator is capable of actuation in the frequency range of $0 - 300$ Hz but it suffers from its low resolution of $2mm$.

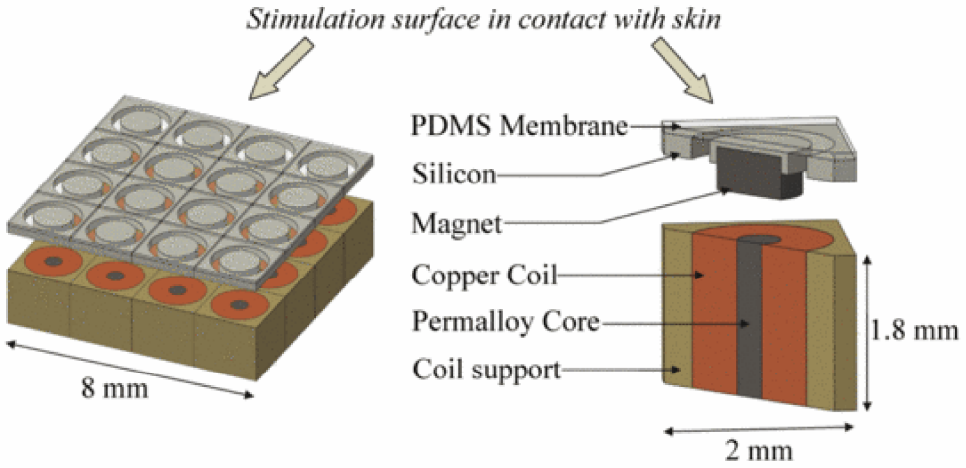

FIGURE 1.13: Global scheme of a MEMS microactuator array for haptic display [29]

1.3.2.2 Acoustic waves focusing

In acoustic wave focusing method, the mechanoreceptors are stimulated by focusing ultrasonic waves on the surface of the skin. We categorize these type of devices into two groups, those operating in air and the one operating on the solid medium.

Airborne ultrasound tactile displays: In this type of haptic display, the air is used as a medium and vibrotactile stimulation is produced on the skin utilizing air focused ultrasound [30, 31, 32]. This method profits the acoustic radiation force, and induces a shear wave in the skin tissue during focusing. The mechanoreceptors are excited and feel the haptic sensation as an influence of displacement of shear wave on the skin [33]. Airborne ultrasound transducers are used to excite the static pressure; the coordinate of the focal position is determined by the phase delay between each transducer proportional to its distance from focal point [30]. The application of this method in haptic has been inspired from sonography. An array of 18×18 airborne transducer is shown in Fig. 1.14 by which a phased array haptic display has been designed [30].

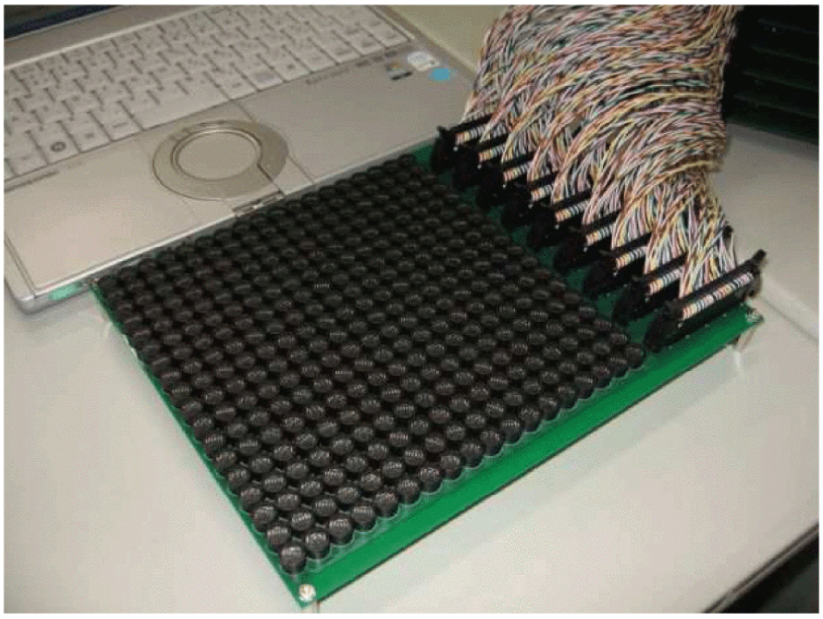

FIGURE 1.14: Phased array of 18 by 18 airborne ultrasound transducers [30]

If powerful acoustic field is excited, it can penetrated the skin. Then, the acoustic waves bypass the receptors and directly excite the nerve fibers and create the touch feelings [34]. Due to the powerful waves, this method is not suitable to design a haptic display.

Focused waves in solid medium: In this case, the solid medium is used as haptic display rather than air. In [35], piezoelectric actuators are placed around a glass panel.

The objective is to excite different hot zone on the plate. The modal parameters of the structure has been taken into account and using wave propagation equation, the actuators' contribution was calculated in order to excite local vibration in the desired zones. This research shows a good focus of vibration rendering in final study 1.15.

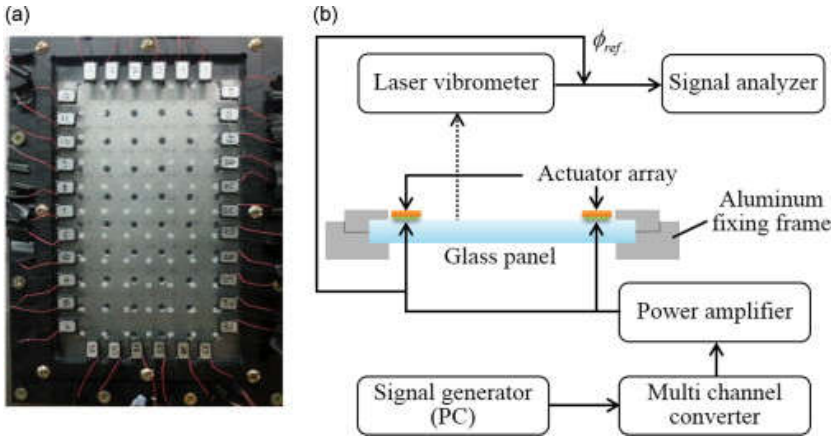

FIGURE 1.15: a. Schematic of phased array haptic display of solid medium [35] b. flow chart of function of the display

To improve the size of focusing spot, it is possible to use the time reversal technique to calculate the actuators supply signals, as shown in Fig. 1.16. Initially, a teaching process is performed on the device. During the teaching process, each location on the surface is excited externally and the surface deformation is recorded by set of transducers. The recorded signals are processed with time reversal later to regenerate the excitation in the same location.

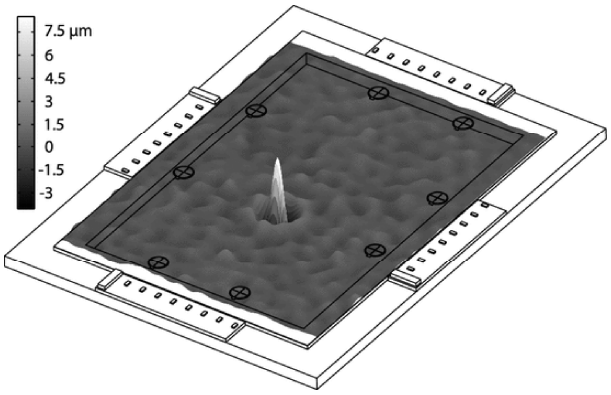

FIGURE 1.16: Ultrasonic time reversal haptic display [36].

In other implementation, the focusing spot is localized under the actuators in 1.17, a number of piezoelectric transducers are glued on a surface. Firstly, the transfer functions between one transducer and the others are identified by exciting one of the transducer in

actuator mode with sine sweep signal and recording the response from other transducers. The process is repeated for all the transducers and the transfer function matrix is obtained. Afterward, the inversion filter technique is applied to determine the required excitation signal to excite local vibration on the top of any transducers 1.17.

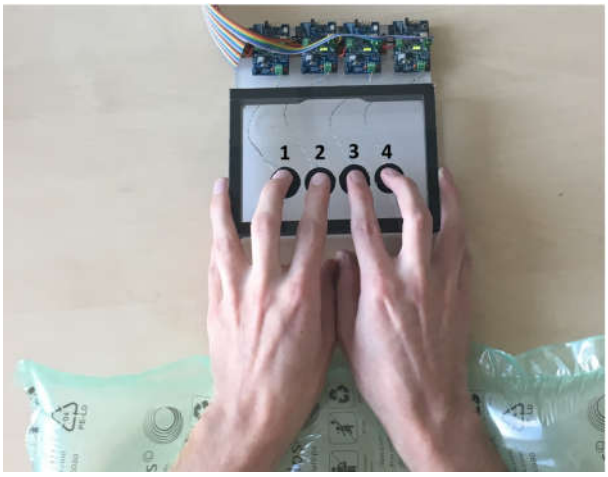

FIGURE 1.17: Photo of haptic display functioned by Spatio-Temporal Inverse Filtering [37].

1.4 Thesis objectives and methods

In this thesis, we want to propose a local stimulation tactile display and its objective is to study the feasibility of a device which is;

- **Robust:** The position of local stimulation area can be predefined with precision and does not suffer from environment changes.
- **Precise:** The local stimulation area is small
- **Applicable:** The set up is not complex and can be used in consumer products for instance.

In this section, we give pros and cons for each technologies of local haptic display. Then, we will explain our method to reach our goal.

1.4.1 Comparison of Local Haptic Displays

All the mentioned technologies are in development phase and few of them have been commercialized. Therefore, we discuss their characteristics below.

Technical principle	Robustness	Precision	Applicability
Time reversal	-	++	−
Phased array in solid medium	-	−	++
Pins array	++	++	−
Inverse Filtering	0	−	++

TABLE 1.1: Comparison of local stimulating haptic displays

Pins array: It is typical example of robust and precise device; indeed the location of stimulation is given by the location of the pins which can be made as small as necessary. However, it is not applicable in a consumer device, because it is complex and bulky.

Phased array in solid medium: Complexity is not so high because the signals to the phase delays are calculated with a simple model. However, it is not precise since the focusing spot is coarse.

Inverse Filtering: The applicability is very high and has been demonstrated practically. However, since the stimulation is located on the transducers it is not precise. Moreover, it is not robust enough, and an identification is necessary.

Time Reversal: It is very precise because a very fine spots of stimulation can be produced. However, It requires complex hardware to operate and since a learning phase is necessary prior to stimulation, in its current state, it is not applicable.

The table 1.1 gives the summery of the characteristics of the aforementioned devices.

It appears that none of the devices have the ideal characteristics. So we want to pick up the advantage of each method to reach our goal. Hence, in this thesis, since , as for the time reversal technique, precision is obtained if a large number of vibration modes are excited, we would like to excite a large number of the modes too. Moreover, since phase array is simply applicable thanks to its model based control, we will also rely on a modal to excite our modes. Finally, robustness cannot be achieved by corresponding the position of stimulation area and actuators as in pins array and inverse filtering, we make the assumption that the robustness can be achieved thanks to a closed loop control of the modes.

Hence the objective of this thesis is to create a focus vibration based on a model of vibrating structure which is also the haptic display. We want to define the requirements of the method for given performances and we want to define the required signals to the actuators used for that purpose. In the next section of this chapter, we detail our methodology.

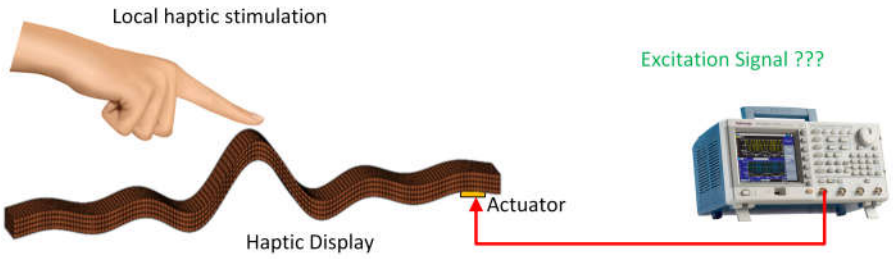

FIGURE 1.18: Local haptic stimulation and required electric signal

1.5 Method

Since we want to create local stimulation area on a solid medium, the question of the thesis is to find a model between electrical signals applied to the actuators and the local tactile stimulation detected by fingers (see Fig. 1.18). Our system, is then composed of piezoelectric actuators used to convert the energy from the electrical domain to the mechanical domain and solid medium made of different material to convert this mechanical energy to the location of stimulation.

One of our problem is that the solid medium does not convey the excitation energy directly to the location we want. We will see in chapter two that this problem can be carried out by taking into account the vibration modes of the structure, which have their distinguished resonance frequency. Hence, the problem is moved from the spatio-temporal domain to a domain based on the temporal evolution of vibration modes amplitude. This technique is called modal decomposition (in this thesis). This method is represented in Fig. 1.19.

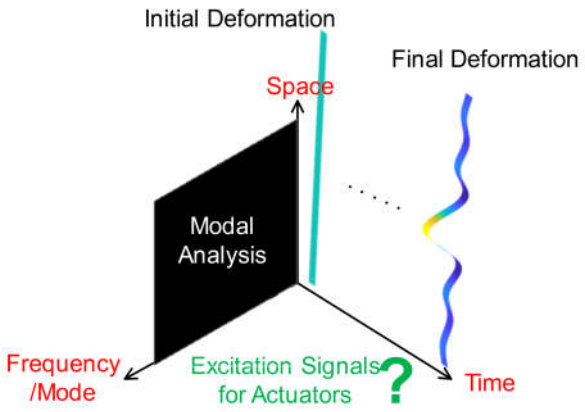

FIGURE 1.19: The schematic of multi-domain problem to study

To be more specific, the process of this thesis is summarized in Fig. 1.20.

It shows that we first calculate the modal decomposition of the desired vibration field and secondly its dynamic behavior from the temporal evolution of the vibration field. We then show how to deduce the excitation signals to the actuators in order to obtain the vibration field with the desired temporal behavior. This gives rise to the haptic stimulation which will be evaluated. It appears that this thesis contains multi disciplinary domain, mainly; vibration and modal analysis, signal processing and haptic science.

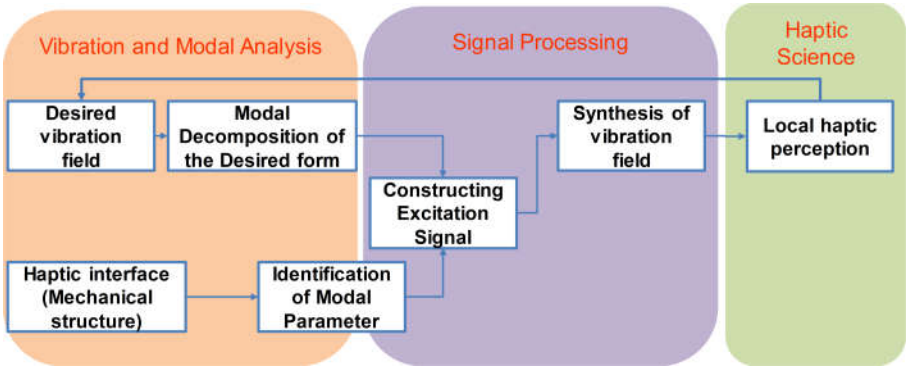

FIGURE 1.20: The global schematic of scientific fields of the thesis

Chapter 2

Flexural Waves and Modal Analysis of Haptic Display

Vibration occurs in many engineering systems. In most of mechanical systems, vibration is a limitation factor in performance and therefore, vibration suppression is necessary. Usually, passive damping is used to control high frequency vibration and low frequency vibration is suppressed with active control [38]. On the contrary, in certain haptic displays the vibration is a key element of functionality. The engineering objective is then to excite certain vibration modes of the structure. These interfaces consist in a mechanical structure (usually a simple surface touched by a user) and one or more transducers to excite and control the vibration. In another term, these haptic interfaces are smart structures on which vibration are excited using active vibration control. To date, several prototypes of these smart structures have been developed and some temporal control techniques have been applied on them. In most of these devices, only one mechanical mode of the structure is excited and this causes a general spatial vibration on the whole structure. Due to increasing interest to design locally vibrating haptic display, hence spatial control is an important topic to investigate, keeping in mind that the objective is to generate local vibration on the smart structure rather than usual vibration suppression.

In order to achieve spatial control of vibration on the haptic display, the model of the structure is required. The dynamic of vibrating structure is governed by Partially Differential Equation (PDE). This PDE does not give the insight of how to excite or control the structure, while modal analysis can be used to decouple the spatio-temporal problem into two sub-problems; the modal analysis and the modal projection. The

modal analysis of structures leads to decouple the vibration modes, the sum of which can explain the whole vibration on the structure. Thus, the system behavior is decoupled into several second order Ordinary Differential Equations (ODEs) where time dependent ODEs are the time function of the vibration modes amplitudes [39]. Achieving these ODEs, the spatial control of vibrating structures could be realized using commonplace control theories.

In this chapter, we give theoretical insights on how to produce local stimulation on a simple haptic device, based on the modal projection. In second section, the modal technique and its application is discussed. The analytical model of our haptic display is presented, and the parameters required to make the model are explained. The third section, presents how to generate an arbitrary spatial vibration form using the modal model of the structure. The modal decomposition of arbitrary spatial form, and how to obtain the required excitation signals of the piezoelectric transducers are discussed, and we apply this technique on an example in section four.

2.1 Basic theory of vibration propagation on a beam

2.1.1 Modelling of the problem

The scope of this thesis is to excite transverse wave on the structure in order to deliver a Haptic feeling for the user. The initial step to control the elastic waves on the surface is to model the problem. Consequently, in this section the problem of propagation of elastic waves on Haptic display will be translated to the mathematical equations. We assume the geometry of the Haptic display as a simple beam 2.1 with a constant cross-section area. A thin layer of piezoelectric material located at $x = x_p$ puts the beam in vibration.

The choice of this geometry is due to its simplicity in applying the theory meanwhile realizing the experiment and measuring vibration. It is supposed that Haptic feeling is linked with the vibration of beam. Accordingly, the model of transverse waves on the beam will explain the behavior of the structure.In this study the influence of the longitudinal waves are neglected in the Haptic interaction.

The transverse waves or shear waves are the waves which oscillate the matter in perpendicular direction(or right angle) to the wave propagation direction. For effective

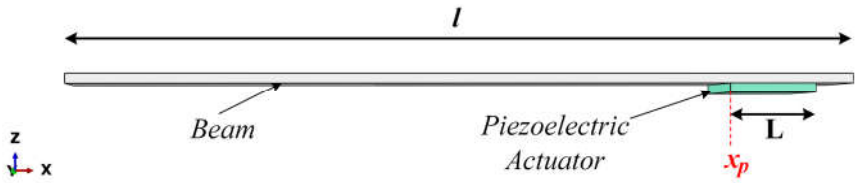

FIGURE 2.1: Schematic of beam with piezoelectric actuator

propagation of shear waves, an acoustically solid material is required, shear waves are not propagating properly in fluids. Transverse waves are relatively weak in comparison to longitudinal waves. Indeed, transverse waves are generated in materials using some of their energy from longitudinal waves [40].

A beam is an one dimensional elastic medium which transits bending and shear moments. There are three main linear hypothesis to model the dynamic of transverse elastic waves on the beam; The Euler-Bernoulli Hypothesis, Rayleigh hypothesis and Timoshenko hypothesis. The Euler-Bernoulli hypothesis considers only the bending moment of the beam and it neglects the shear and rotary deformation [41, 42, 43] . On the other hand, the Rayleigh hypothesis takes into account the effect of rotary inertia as well. The Timoshenko hypothesis takes into account all bending, shear and rotary momentum in modelling the transverse dynamic of the beam [44, 45]. In this study, the rotary and shear moments is considered to be negligible comparing to bending moment , consequently the Euler-Bernoulli hypothesis is considered for the problem.

The theory of propagation of flexural waves in solid media starts with definition of strains in the material. If we consider a beam, and inside this beam, a particle of matter located at the point M whose coordinates are $M(x, y, z)$; under external forces, the beam changes its shape and due to this deformation the particle displaces to the point $M'(x', y', z')$. We call $u = MM'$ the displacement vector. The coordinates of u are $u(u_x, u_y, u_z)$ with $u_x = x' - x$,$u_y = y' - y$ and $u_z = z' - z$. By definition, the strains $\boldsymbol{\epsilon}$ represent the relative displacement of the particles of the beam and we have:

$$\boldsymbol{\epsilon} = \begin{bmatrix} \epsilon_{xx} & \epsilon_{yy} & \epsilon_{zz} & \epsilon_{xz} & \epsilon_{yz} & \epsilon_{xy} & \epsilon_{zx} & \epsilon_{yx} & \epsilon_{zy} \end{bmatrix}^T \tag{2.1}$$

In above equation, ϵ_{xx}, ϵ_{yy}, and ϵ_{zz} are the axial deformations in three-orthogonal cartesian coordinate (x, y, z). While, ϵ_{xz}, ϵ_{yz}, ϵ_{xy}, ϵ_{zx}, ϵ_{yx}, and ϵ_{zy} are shear strains [46, 46] . The Shear strains are symmetric, which means;

$$\epsilon_{xz} = \epsilon_{zx} \qquad \epsilon_{yz} = \epsilon_{zy} \qquad \epsilon_{xy} = \epsilon_{yx} \tag{2.2}$$

Assuming small perturbations, the displacements are related to the strains according to the differential relations:

$$\epsilon_{xx} = \frac{\partial u_x}{\partial x} \tag{2.3a}$$

$$\epsilon_{yy} = \frac{\partial u_y}{\partial y} \tag{2.3b}$$

$$\epsilon_{zz} = \frac{\partial u_z}{\partial z} \tag{2.3c}$$

$$\epsilon_{xy} = \frac{\partial u_x}{\partial y} + \frac{\partial u_y}{\partial x} \tag{2.3d}$$

$$\epsilon_{zx} = \frac{\partial u_z}{\partial x} + \frac{\partial u_x}{\partial z} \tag{2.3e}$$

$$\epsilon_{zy} = \frac{\partial u_z}{\partial y} + \frac{\partial u_y}{\partial z} \tag{2.3f}$$

This thesis is focused on the study of a beam for which the in-plane displacements u_z and u_y depend upon the axial coordinate x only. Therefore, we write;

$$\epsilon_{yy} = \frac{\partial u_y}{\partial y} = 0 \tag{2.4a}$$

$$\epsilon_{zz} = \frac{\partial u_z}{\partial z} = 0 \tag{2.4b}$$

$$\epsilon_{zy} = \frac{\partial u_z}{\partial y} + \frac{\partial u_y}{\partial z} = 0 \tag{2.4c}$$

Applying the Euler-bernoulli kinematic hypothesis lead to write the deflection field $\boldsymbol{w}$ and displacement at the direction u_x as;

$$u_x = -z\frac{d\boldsymbol{w}}{dx} \tag{2.5}$$

$$\epsilon_{xx} = \frac{\partial u_x}{\partial x} = -z\frac{d^2\boldsymbol{w}}{dx^2} \tag{2.6}$$

Under all the aforementioned hypothesis, the transverse displacement of particles of the beam follows the dynamic equations given in Eq. 2.7, according to the Euler-Bernoulli beam model:

$$\rho A\frac{\partial^2 \boldsymbol{w}}{\partial t^2} + EI(\frac{\partial^4 \boldsymbol{w}}{\partial x^4}) = p(x,t) \tag{2.7}$$

in above equations ρ is the density of the beam's material, A is the cross section area of the beam, $p(x,t)$ is force linear density, E is Young's modulus and I is the second moment of area of beam about the *neutral plane*. The Eq. 2.7 explains the spatiotemporal behavior of the beam for the given excitation force $p(t)$. If we consider that the

piezoelectric actuator generates the force and the beam is the simple haptic display, determining the spatial form of vibration by the given partially differential equation (PDE) is not obvious. In other term, the relationship between input force and output vibration is coupled in space and time with partially differential equation and this equation is not in the straightforward classical control framework. In the next section, we show how to use modal modelling to decouple those temporal and spatial behavior.

2.2 Modal Modelling and Orthogonality principle

In recent decades, implementation of active vibration control has been increased as a result of progress in microprocessor technology and realization of digital signal processing for control system. Using active vibration control, different control algorithms have been developed in aerospace [47, 48], mechanical system [49] [50] and civil engineering [51] [52]. The typical challenge in active vibration control is dynamic model of vibration system which is usually not available. The finite element model of the vibration system is reachable while it is not possible to design controllers due to the high number of Degree Of Freedoms (DOFs) of the model. The solution is modal control method which is based on the coordinate transformation idea and decouples the system into a set of independent single-DOF systems of modal coordinates [53, 54, 39, 55, 56, 57, 58, 59, 60]. Thus, the design of control system can be carried out for each mode (single-DOF) no matter how large the model is. However according to the modal control theory, vibration of any structure can be explained by infinitive number of modes of vibration, the operation of modal modelling of vibration system is usually carried out on a reduced model of the system, using finite number of modes. The reduced model can be determined through finite element analysis or experimental modal identification techniques [61]. As a result, the modal control technique facilitates the understanding of mechanical system and its control by splitting the model to finite single-DOF systems. However, in this thesis, we do not study the closed loop control of the modes, we only present how to use the modal decomposition to obtain predefined vibration pattern in open loop.

In this subsection, the modal modelling theory is applied to the beam, where we neglect the effect of damping leading the equation:

$$\rho A \frac{\partial^2 \boldsymbol{w}}{\partial t^2} + EI\left(\frac{\partial^4 \boldsymbol{w}}{\partial x^4}\right) = \mathbf{p}(x,t) \tag{2.8}$$

The excitation force of the piezoelectric actuator can be defined by the applied voltage according to Mason piezoelectric equivalent circuit [62, 63, 64] as following:

$$\begin{aligned} \mathbf{p}(x,t) &= \gamma v_{p(t)} \; if x \in [x_p; x_p + l] \\ &= 0 \; if x \notin [x_p; x_p + l] \end{aligned} \tag{2.9}$$

In modal theory, the deflection of the beam $\boldsymbol{w}(x,t)$ in Eq. 2.8 can be described with spatial eigenvectors (called mode shapes of the beam, $\varphi_k(x)$) and temporal coefficients (called modal coefficients, $\eta_k(t)$) as shown Eq. 2.10

$$\boldsymbol{w}_{(x,t)} = \sum_{k=1}^{\infty} \varphi_k(x)\eta_k(t) \tag{2.10}$$

where $\varphi_{k(x)}$ is the k^{th} eigenfunction and the $\eta_{k(t)}$ modal coefficient of k^{th} eigenfunction. As a result of this modal presentation of the vibration, the spatiotemporal behavior of the deflection of the beam can be decoupled to a spatial part ($\varphi_k(x)$ mode shapes) and a temporal part ($\eta_k(t)$ modal coefficient).

There is a key feature of the mode shapes of the mechanical structure which guarantees the viability of superimposition in Eq. 2.10. In fact the orthogonality of the mode shapes create an orthogonal-subspace where the mechanical behavior of the structure can be described by its coordinate. The orthogonality of the mode shapes are defined as follows;

$$\int_{-l/2}^{l/2} \rho A \varphi_i(x)\varphi_j(x)\, dx \; = \delta_{i,j} \tag{2.11}$$

where

$$\delta_{i,j} = \begin{cases} 1 & \text{if } i = j; \\ 0 & \text{otherwise.} \end{cases} \tag{2.12}$$

This property allows us to project the equation 2.7 into the base of modal shapes. To simply explain the above equation, the orthogonality tells that each mode has not any linear correlation with other modes. Meanwhile, the linear self-correlation of each mode is unity values.

To explain the vibration behavior of a haptic display in modal space, ideally infinite number of the modes of structure is required. While, in practice finite number of modes

can be excited. Thus, number of modelled modes are limited in practice. In fact in practical application of these theories, one of the challenges is to define limited modal-subspace. The modes which are chosen to explain the behavior of structure in practice are called modelled modes. The other modes of structure which are not identified or excited during the modal test and modal synthesis of vibration are called non-modelled modes or neglected modes. This question of how to chose the modelled modes of a haptic display will be discussed in chapter 4.

$$\rho A \sum_{k=1}^{\infty} \varphi_k(x)\ddot{\eta}_k(t) + EI \sum_{k=1}^{\infty} \frac{\partial^4 \varphi_k(x)}{\partial x^4}\eta_k(t) = p(x,t) \tag{2.13}$$

Applying the projection on $\varphi_n(x)$ leads to:

$$\int_{-l/2}^{l/2} (\sum_{k=1}^{\infty} \rho A \varphi_k(x)\ddot{\eta}_k(t) + \sum_{k=1}^{\infty} EI \frac{\partial^4 \varphi_k(x)}{\partial x^4}\eta_k(t))dx - \int_{-l/2}^{l/2} p(x,t)\varphi_n(x)dx = 0 \tag{2.14}$$

inversing of $\sum$ and $\int$ gives;

$$\sum_{k=1}^{\infty} (\int_{-l/2}^{l/2} \rho A \varphi_k(x)\ddot{\eta}_k(t)\varphi_n(x)dx) + \sum_{k=1}^{\infty} (\int_{-l/2}^{l/2} EI \frac{\partial^4 \varphi_k(x)}{\partial x^4}\eta_k(t)\varphi_n(x)dx) = \int_{-l/2}^{l/2} p(x,t))\varphi_n(x)dx \tag{2.15}$$

due to the orthogonality property:

$$\sum_{k=1}^{\infty} (\int_{-l/2}^{l/2} \rho A \varphi_k(x)\ddot{\eta}_k(t)\varphi_n(x)dx) = \ddot{\eta}_n \tag{2.16}$$

Moreover, taking into account the boundary conditions we can show that;

$$\begin{aligned} \sum_{k=1}^{\infty} (\int_{-l/2}^{l/2} EI \frac{\partial^4 \varphi_k(x)}{\partial x^4}\varphi_n(x))dx &= [EI \frac{\partial^3 \varphi_k(x)}{\partial x^3}\varphi_n(x)]_{-l/2}^{l/2} - [EI \frac{\partial^2 \varphi_k(x)}{\partial x^2}\varphi_n(x)]_{-l/2}^{l/2} \\ &+ \int_{-l/2}^{l/2} EI \frac{\partial^2 \varphi_k(x)}{\partial x^2} \frac{\partial^2 \varphi_n(x)}{\partial x^2} dx = 0 + 0 + \omega_n^2 \delta_{k,n} \end{aligned} \tag{2.17}$$

so, by substituting Eq. 2.16 and Eq. 2.17 into Eq. 2.15, we will have;

$$\ddot{\eta_n}(t) + \omega_n^2 \eta_n(t) = P_n(t) \; where \; P_n(t) = \int_{-l/2}^{l/2} p(x,t)\varphi_n(x)dx \tag{2.18}$$

Here, ω_n represents the resonance angular frequency of the n^{th} mode and is given in Eq. 2.17. If we take into account the equation 2.9 P_n writes;

$$P_n(t) = \int_{-l/2}^{l/2} p(x,t)\varphi_n(x)dx = \int_{x_p}^{x_p+L} \gamma v_p \varphi_n(x)dx = \int_{x_p}^{x_p+L} \varphi_n(x)dx\gamma v_p(t) \tag{2.19}$$

In the equation 2.18, all spatial parts have been eliminated and the dynamic response of the beam is related to the modal coefficients of the modes. In other term, thanks to the application of the modal solution of vibration, the dynamic of the vibration of the beam can be explained with ideally infinitive number of modal coefficients whose behavior are described by second order linear ordinary differential equations. If we take into account the natural damping of the structure by a damping factor, the equation 2.18 becomes;

$$\ddot{\eta}_n(t) + 2\zeta_n\omega_n\dot{\eta}_{n)}(t) + \omega_n^2\eta_n(t) = \alpha_n v_p(t) \tag{2.20}$$

In this equations the ζ_n is the damping factor of n^{th} mode and α_n is the modal gain of mode n. These dynamic parameters as well as mode shapes of the modes should be accurately identified to built the modal model of the haptic display. Identification of these parameters will be discussed in the chapter 3. While, the next sections deals with synthesis of predefined vibration pattern on the beam.

2.3 Spatial Vibration Synthesis

As shown in Eq. 2.8 the vibration equation of the structure was coupled in time and space with the partially differential equation by which it was not evident how to excite the desired spatial form. Using the orthogonality property, the modal decomposition was applied to the dynamic behavior equation of structure and as a result , the coupled spatio-temporal equation (Eq. 2.8) was decoupled to a set of second order ordinary differential equations in time domain 2.20. The decoupling processes will result to study the spatial behavior of the structure independently of its temporal behavior and vice versa. The purpose of this section is to show how a spatial form vibration on a structure can be determined and excited theoretically. To this aim, firstly, the spatial specification of the desired vibration is presented and how to calculate the modal coefficients to render

the vibration form is shown. Afterward, the temporal behavior of the system is taken into account to explain how to excite modes to obtain desire spatial vibration form.

2.3.1 Spatial form specification

In this subsection, the temporal transient evaluation of the vibration on structure is neglected. Only the spatial behavior of the beam at a given time of $t = T_f$, is studied. A predetermined spatial form of vibration in a given time of $t = T_f$ $\ddot{\boldsymbol{w}}_R(x)$ is taken into account and the objective is to define the modal coefficients of each mode.

The spatial form of vibration can be related to the vibration acceleration $\ddot{\boldsymbol{w}}_R(x)$, vibration velocity $\dot{\boldsymbol{w}}_R(x)$ or vibration displacement $\boldsymbol{w}_R(x)$. In this study, the spatial vibration velocity has been considered and all the modal decomposition and the modal synthesis have been developed. Of course, the method can be extended to generate an acceleration or a displacement profile.

We determine necessary spatial factors by projecting the desired spatial form into the modes in order to be able to excite the desired spatial form. To determine the modal factor for each mode, the desired reference vibration velocity form $\dot{\boldsymbol{w}}_{R(x,T_F)}$ is firstly decomposed to its modal coefficients using below formula;

Starting from the modal representation equation for the desired vibration form;

$$\dot{\boldsymbol{w}}_R(x, T_f) = \sum_{k=1}^{\infty} \dot{\eta}^*_{kR}(T_f)\varphi_k(x) \tag{2.21}$$

by multiplying both side of the equation to ρA and projecting to the mode $\varphi_k(x)$ and taking into account the orthogonality property;

$$\begin{aligned}
\rho A \int_{-l/2}^{l/2} \dot{\boldsymbol{w}}_R(x, T_f)\varphi_n(x)dx &= \rho A \int_{-l/2}^{l/2} \sum_{k=1}^{\infty} \dot{\eta}^*_{kR}(T_f)\varphi_k(x)\varphi_n(x)dx \\
&= \sum_{k=1}^{\infty} \dot{\eta}^*_{kR}(T_f) \int_{-l/2}^{l/2} \rho A\varphi_k(x)\varphi_n(x)dx \\
&= \sum_{k=1}^{\infty} \dot{\eta}^*_{kR}(T_f)\delta_{(k,n)} \\
&= \dot{\eta}^*_{nR}(T_f)
\end{aligned} \tag{2.22}$$

The interpretation of Eq. 2.22 is that the desired vibration velocity form $\dot{\boldsymbol{w}}_R(x, t_F)$ can be generated by exciting infinite number of modes whose modal coefficient value are equal to $\dot{\eta}_{nR}$. Practically any spatial arbitrary vibration form can be generated by model decomposition as long as it is compatible with the kinematic constraints of the structure. However, in practice exciting infinite number of modes is not feasible, therefore, the spatial vibration form can only be approximated.

2.3.2 Example of Modal Decomposition of a Spatial Form

This subsection clarify the modal decomposition of spatial form with an example. Let's considered $\dot{\boldsymbol{w}}_R(x, T_F)$,which is shown in Fig. 2.2, as the vibration velocity field which we would like to generate on the beam. The spatial form is supposed to be a sinc function in this figure while any kind of spatial form can be considered and applied to the theory.

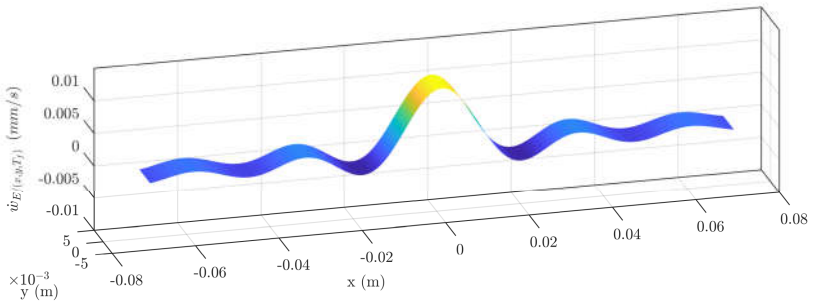

FIGURE 2.2: Example desired spatial vibration velocity form $\dot{\boldsymbol{w}}_{R(x,T_F)}$

Firstly, for the purpose of creating a virtual prototype, the mode shapes have been simulated by using a finite element modelling. The first five mode shapes are presented in Fig. 2.4. Then, the desired spatial form $\dot{\boldsymbol{w}}_R(x, T_F)$ is projected to the mode shapes of the structure using Eq. 2.22, an reported in Fig. 2.3 for the first twenty modes. For the purpose of illustration the figure 2.4 right shows the mode shapes multiplied by the modal coefficients.

Among the modal coefficients $\dot{\eta}_{1R}$, $\dot{\eta}_{3R}$, $\dot{\eta}_{5R}$,$\dot{\eta}_{7R}$,$\dot{\eta}_{9R}$ and $\dot{\eta}_{11R}$ have dominant participation to the desired spatial form.

By summation of these six modal components using Eq. 2.10, the desired spatial vibration velocity form can be excited on beam at $t = T_F$ as shown in Fig.2.5. Of course the excited spatial form will be an approximation of desired spatial form, since a finite number of modes are excited.

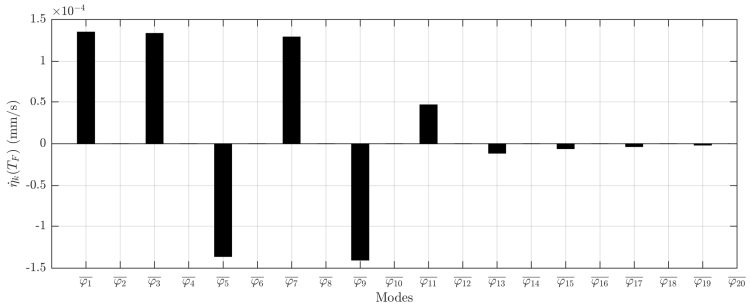

FIGURE 2.3: Modal coefficients of desired spatial form $\dot{\eta}^*_{nR}$

This section presented all the required theory, parameters and procedure to excite an arbitrary spatial form of vibration on a beam. All the theory presented in this section explains the spatial behavior of the structure at a specific time $t = T_F$. The definition of the temporal evolution of the modes is the topic of the next section.

2.4 Temporal Transient Control of Modes

As mentioned earlier, the behavior of the structure for any excitation responds to the elastic wave propagation which is happening in time and spatial domains. The spatial analysis of the vibration has been already discussed in previous subsection. Here, we concentrate on the temporal behavior. According to Eq. 2.20 it can be explained with the second order response of the modes. This section is divided into two subsections. First we present the general equation determining dynamic response of the modes and how to calculate the excitation signal to the piezoelectric actuator. Then we detail a specific case of modes' transient, namely exponential excitation, which is studied in this thesis to render haptic feeling.

2.4.1 How to determine transient of modes

Let's consider the dynamic equation of modes which are governing the dynamic of vibration on beam as in Eq. 2.20. We would like to carry the problem into Laplace domain to have a better insight to the input and output of the system and the dynamic of the system's modes. The dynamic equations of modes in Laplace domain are obtained as follows;

$$s^2\boldsymbol{\eta}_{n(s)} - s\eta_{n(0)} - \eta'_{n(0)} + 2\zeta_n\omega_n(s\boldsymbol{\eta}_{n(s)} - \eta_{n(0)}) + \omega_n^2\boldsymbol{\eta}_{n(s)} = \alpha_n\mathbf{v}_{p(s)} \tag{2.23}$$

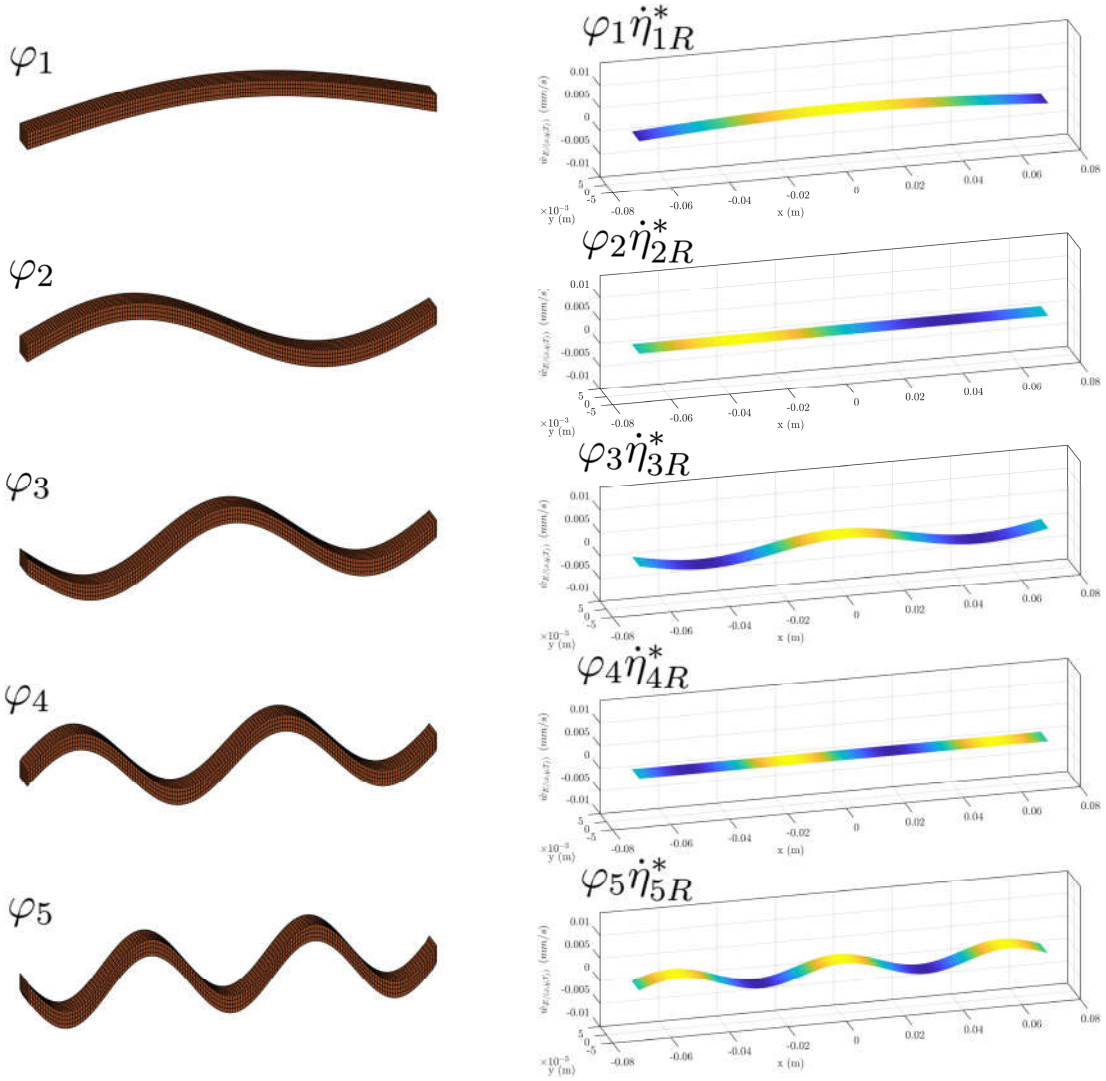

FIGURE 2.4: **Left.** First five mode shapes of beam (structure) **Right.** Modal participation of each mode for reconstructing the desired spatial form (only for five first mode and modal coefficients).

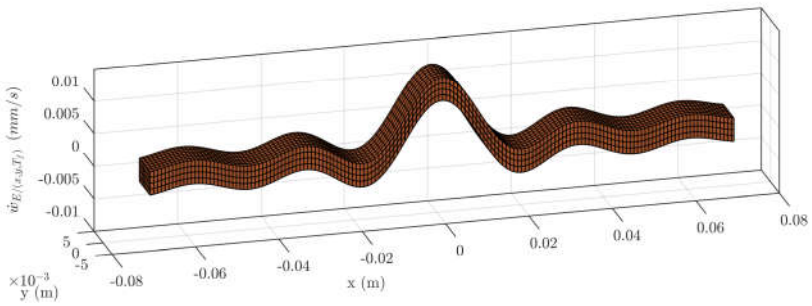

FIGURE 2.5: Synthesis of the spatial form using infinite number of the modes on the beam

In this equation, the $\boldsymbol{\eta}_{n(s)}$ and $\mathbf{v}_{p(s)}$ are the Laplace transform of the n^{th} modal coefficient and excitation voltage respectively. $\eta_{n(0)}$ is the initial condition of the n^{th} modal coefficient. Assuming that the beam initially is in the equilibrium situation will cause all the initial condition become zero. Applying this assumption to above equations, leads to;

$$s^2\boldsymbol{\eta}_{n(s)} + 2s\zeta_n\omega_n\boldsymbol{\eta}_{n(s)} + \omega_n^2\boldsymbol{\eta}_{n(s)} = \alpha_n\mathbf{v}_{p(s)} \tag{2.24}$$

between the voltage applied to the actuator and the modal coefficient $\boldsymbol{\eta}_{n(s)}$. Eq. 2.24 is reorganized to obtain the transfer function for the n^{th} mode named $\mathbf{H}_n$ as follow;

$$\mathbf{H}_{n(s)} = \frac{\boldsymbol{\eta}_{n(s)}}{\mathbf{v}_{p(s)}} = \frac{\alpha_n}{s^2 + 2s\zeta_n\omega_n + \omega_k^2} \tag{2.25}$$

We would like that each mode is excited equal to their reference modal coefficient value at the time T_f denoted by $\dot{\eta}^*{}_{nR}$. But we need to construct the transient between $t = 0$ and $t = T_f$, because it is not specified by the modal shape definition. But this transition cannot be specified haphazardly. Indeed, if we calculate $V_p(s)$ by definition 2.25 we have;

$$\begin{aligned} \mathbf{v}_{p(s)} &= \mathbf{H}_1^{-1}(s)\dot{\eta}^*{}_{1R} \\ &= \mathbf{H}_2^{-1}(s)\dot{\eta}^*{}_{2R} \\ &= ... \end{aligned} \tag{2.26}$$

obviously, $\mathbf{v}_{p(s)}$ cannot fulfill the equation 2.26 for all the modes. The method chosen in this thesis is to use the frequency decoupling of the structure. The idea is to build intermediate voltages $\mathbf{v}_{np}(s)$ such that;

$$\mathbf{v}_{np}(s) = \mathbf{H}_n^{-1}(s)\eta_{nR}(s) \tag{2.27}$$

Then we build;

$$\mathbf{v}_{p(s)} = \sum_{k=1}^{N_{mm}} \mathbf{v}_{kp}(s) \qquad N_{mm} = number\ of\ modelled\ modes \tag{2.28}$$

Indeed,

$$\begin{aligned}\boldsymbol{\eta}_{n(s)} &= \mathbf{H}_{n(s)}\mathbf{v}_{p(s)} \\ &= \mathbf{H}_{n(s)} \sum_{k=1}^{N_{mm}} \mathbf{v}_{kp(s)} \\ &= \sum_{k=1}^{N_{mm}} \mathbf{H}_{n(s)}\mathbf{v}_{kp(s)}\end{aligned} \tag{2.29}$$

then, if η_{kR} is chosen in such a way that;

$$|\mathbf{H}_n(s)\mathbf{v}_{kp}(s)| \simeq 0 \qquad if k \neq n \tag{2.30}$$

then

$$\boldsymbol{\eta}_n(s) = \mathbf{H}_n(s)\mathbf{v}_{np}(s) = \mathbf{H}_n(s)\mathbf{H}_n^{-1}(s)\eta_{kR} = \eta_{kR} \tag{2.31}$$

in practice, the condition Eq. 2.30 is fulfill if the frequency contents of $\boldsymbol{\eta}_{nR(s)}$ is inside the bandwidth of the mode n, and outside the bandwidth of all other modes, as depicted in Fig. 2.6. In the next subsection we present an example of reference form $\boldsymbol{\eta}_{nR(s)}$ which is convenient and has been utilized in this thesis.

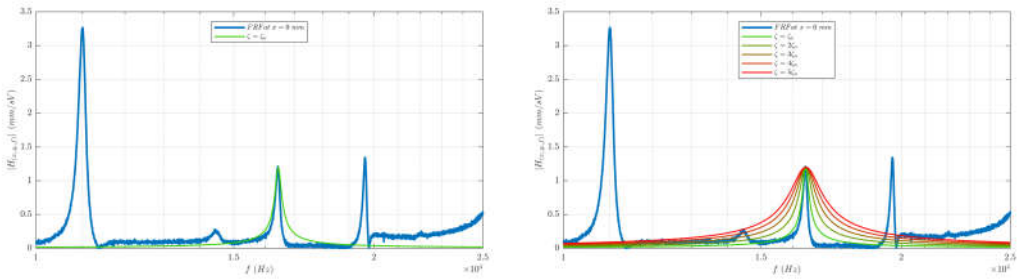

FIGURE 2.6: **Left.** The transfer function of an example structure (blue line) and a well defined excitation signal whose frequency of excitation falls inside the bandwidth of a single mode at 17 kHz (green color) **Right.** Red color curve shows frequency band of an uncorrect excitation voltage signal whose frequency band falls in bandwidth of multiple of modes

2.4.2 Case study of exponential excitation

This subsection discusses how to excite the N_{mm} modes from their initial state of equilibrium to their target value of η_{nR}^*. Considering the comments in previous section, a

cosinusoidal term $cos(\omega_n t)$ is defined to excite the n^{th} mode in its resonance frequency of f_n ($\omega_n = 2\pi f_n$).

Second factor in determining the temporal behavior of the modes are their temporal evolution. From haptic point of view, the ideal case is when the modes make immediate passage from equilibrium to the final value η^*_{nR} when it is not viable from structure dynamic point of view. Inspired by natural response of the system, we consider an exponential push function to make an amplitude modulation of cosinusoidal function and guide the transient from initial zero state of mode to its target state η^*_{nR}. The exponent coefficient is considered to be $\zeta_n\omega_n$ and the time span is limited to $t = [0 - T_f]$. In the moment T_f it is supposed that the transient of the mode dynamic has been terminated and the mode has arrived to its focusing amplitude η^*_{nR}. After the focusing moment T_f, which is post transient, the structure is left non excited to arrive to equilibrium with free vibration. Accordingly, Eq. 2.32 shows the analytical expression of determined dynamic for the n^{th} mode that we proposed.

$$\dot{\eta_n}(t) = \dot{\eta}^*_{nR} cos(\omega_n(t - T_F)) e^{\zeta_n\omega_n(t-T_F)}(u_{(T_F+\frac{\pi}{2\omega_n}-t)} - u_{(t)}) \tag{2.32}$$

in above equation, $u(t)$ is for heaviside step function, the cosinusoidal term is for exiting n^{th} mode in its resonance angular frequency ω_n. ζ_n is proportional damping of the mode n, the exponential function is the amplitude modulation for resonance excitation which terminate in final value of $\dot{\eta}^*_{nR}$ and $u_{(t)}$ is the step function for determining the time span for dynamic of mode. It should be highlighted that after the end transient T_f that the modes will experience a post transient with free vibration decaying to equilibrium.

Practically each mode has distinguished value of resonance angular frequency and damping factor. As a result the rise time value of each mode is different from other. Since in spatial form rendering N_{mm} number of modes are required in temporal excitation of modes there are some modes having longer rise time than others. Such case can be problematic by generating significant vibration amplitude during the transient or the past transient and it can be solved by exciting sharper exponential function. Therefore, in special cases the dynamic of modes can be modulated with an exponential function which is far faster than the natural response as in the following equation:

$$\dot{\eta_k}(t) = \dot{\eta}^*_{kR} cos(\omega_k(t - T_F)) e^{\kappa\zeta_k\omega_k(t-T_F)}(u_{(T_F+\frac{\pi}{2\omega_k}-t)} - u_{(t)}) \tag{2.33}$$

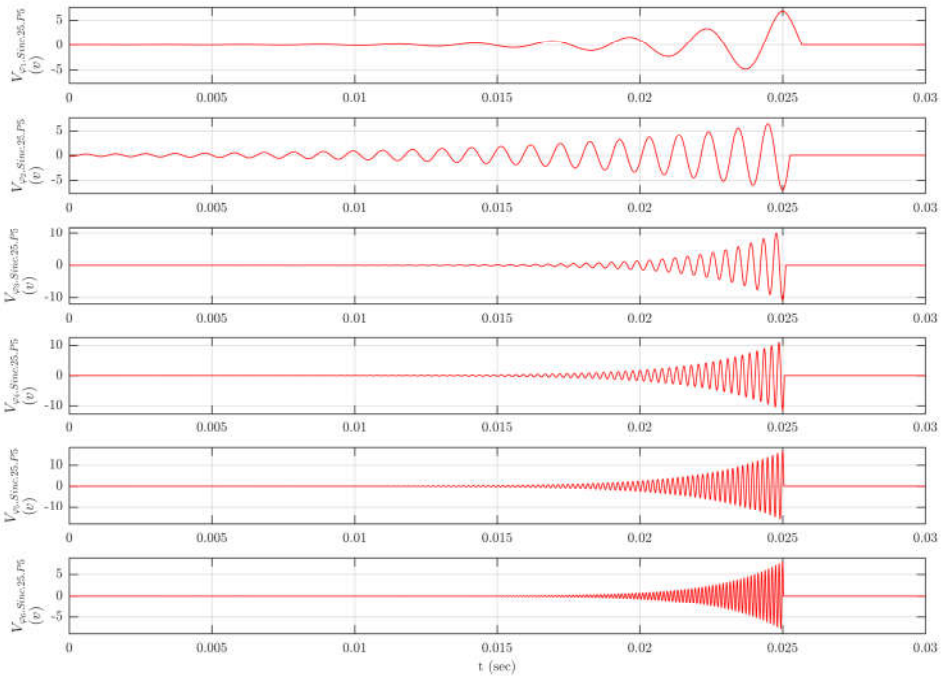

FIGURE 2.7: Excitation voltage for each mode $V_{\varphi_k.E.25.Squa.P5(t)}$ to excite $\dot{\boldsymbol{w}}_{E.25.Squa.P5\,(x,t)}$

where, κ is constant coefficient which can take values larger than zero and is defined to accelerate or decelerated the transient of mode from initial to final state. As the dynamic behavior of the mode is determined in temporal domain, by substituting Eq. 2.32 to Eq. 2.20 the voltage signal of each actuator can be determined as follow;

$$v(t) = \sum_{k=1}^{N_{mm}} \frac{\dot{\eta}^*_{kR}}{\alpha_k} cos(\omega_k(t - T_F))e^{\zeta_k\omega_k(t-T_F)})u(T_F + \frac{\pi/2}{\omega_k} - t) \tag{2.34}$$

Since the voltage signal of the actuators $v_i(t)$ are achieved thus the desired spatial deformation velocity can be rendered $\dot{\boldsymbol{w}}_{R(x,T_F)}$ now.

2.4.3 Example

For the purpose of illustration, we present Fig. 2.7 the intermediate voltages for six first modes of a beam ($105mm \times 7mm \times 1mm$ Aluminium). This example is extensively treated in chapter 4. Here, we only present the result of the voltage calculation. This

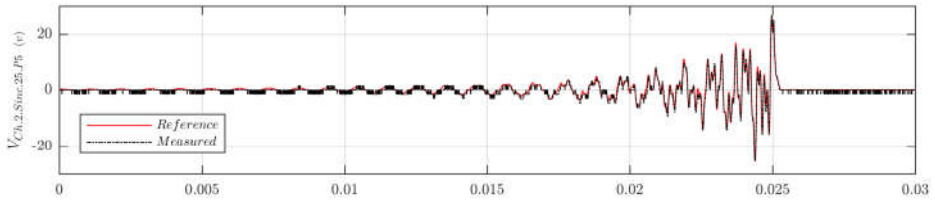

FIGURE 2.8: The reference (red) and experimentally applied (dot-dashed black) voltage signals to actuator set 2.

six voltages are then summed up to produce the voltage $v_p(t)$ depicted in Fig. 2.8.

2.4.4 Conclusion

This chapter presents the theoretical background of the modal decomposition. Starting from the equation governing the vibration propagation on the beam. We use the concept of modal shapes to decouple the space and the temporal domains. Then, the orthogonality property of the mode shapes is used in order to calculate the modal coefficients of each mode, by projection of the desired vibration form onto each modal shape. A study with an example emphasized the fact that in practice, only a limited number of modes, namely the modal model,are required to achieve a good approximation of the desired vibration field. Then we discuss on the voltage necessary to actuate the modes. Here, we use the frequency decoupling. Conditions to use this method is required, leading to a condition on the frequency content of the modal coefficients. Thanks to these theoretical tool, this method is applied on an experimental test bench in the next chapters.

Chapter 3

Modal Parameter Identification of Haptic Displays

In the previous chapter, a methodology to synthesize a given spatial shape at given instant in time has been presented. It requires the knowledge of;

- the mode shapes, which constitute the basis to specify the desired focusing shape
- the dynamic parameters (resonance frequencies and damping factors of modes), to determine the excitation voltage signals

Therefore, the objective of this chapter is to identify the model parameters. That is a method to determine the values of the parameters of the modal model such that a good correlation between the prediction of the modal and physical measurement is achieved. It will then be possible to predetermine the behavior of vibrotactile haptic display.

There are two main categories of structural identification technics; Experimental Modal Analysis and Operational Modal Analysis.

- In experimental modal analysis (EMA), measured data from the experimental response of the structure to a specific excitation are used to identify the parameter of the models, which explains the structure behavior. An accurate identification with EMA requires a precise definition of excitation signal, application-specific simplification, accurate vibration measurement, data acquisition, data resolution and signal processing. Therefore, it requires specific set-up which are difficult to deploy.

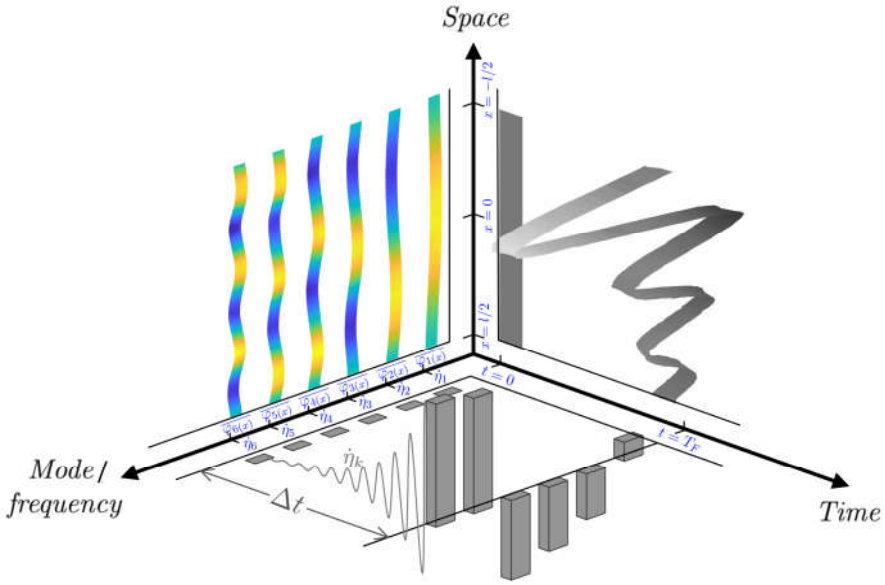

FIGURE 3.1: Spatio-Tempro-Modal schematic; mode shapes which couples the system spatial behavior to mode frequencies

- Operational Modal Analysis (OMA) on the contrary are a family of the methods that allow to identify the dynamic of an existing mechanical structure, where the excitation is not controlled. It is based on vibration measurements where the actual input is unknown. Usually, it is used on large structure where excitation is difficult to realize.

EMA is the process of characterizing the dynamic property of elastic structure by identifying the natural modes of vibration from the experimental excitation. In modal analysis and EMA, damping factors and natural frequencies are the parameters associated with each mode, for the time response. Meanwhile, each mode has its spatial characteristic that is defined as mode shape. The mode shape defines the special distribution of movement over entire structure. By obtaining this model parameter, one can explain the spatial behavior of structure with frequency of mods or vice versa. Therefore, the modal model couples spatial behavior structure to frequency domain behavior as it is shown in fig. **??**.

The common EMA method for identifying dynamic characteristics of small and medium size structure is forced vibration tests. In this method, the structure is excited using a controlled force and by measuring the structure response to this force. There exists many techniques to induce controlled force vibration on structure for the purpose of identification. Two most important controlled excitations are Mechanical shaker and Transient loads.

- The mechanical shaker can be realized with electro-magnetic actuator, piezoelectric actuator, rotating eccentric mass or hydraulic actuator. Mechanical shakers, are used to apply forces in sufficiently large amplitude and within frequency range of interest.
- The transient load force excitation can be realized with pull-back and release or with impact hammer. i

in this study, the mechanical shaker method, more specifically piezoelectric actuator is used to apply identification test. The main reason is that vibrotactile haptic display is already integrated with one or more patches of piezoelectric actuators, consequently the same actuator are used to make the identification of modal parameters.

There are two main approach to identify modal parameters, Time Domain Identification and Frequency Domain Identification. The time domain identification of modal parameter is based on directly processing the time measurement of the structure (either force or deformation). There are various time domain modal identification methods. The Ibrahim Time Domain is probably the first technique which was presented in 1970s [65]. However it is based on the assumption that the system resonance are well decoupled [66]. Other methods, using less restrictive hypothesis have since been proposed: Stochastic subspace Identification [67], Least-squares time domain method [68], The Eigensystem Realization Algorithm [69, 70], ARMA time series method [71, 72, 73] and AR Models and Poly Reference [74, 75].

In frequency domain identification the forced response structure measurement data are transformed using FFT algorithm and Frequency Response Functions (FRF) are obtained for each deflection point. The advantage of frequency domain identification is the simplicity of identifying multiple of the modes in the frequency band of excitation signal. This is due to the fact that, around resonance frequency of the mode the FRF gain are local maximal.There are different technique to realize frequency domain identification of modal parameters, such as Frequency Domain Decomposition [76], Peak-Picking Method [77, 78], Circle Fit Method [79], Inverse FRF Method [80], Lease-Squares Frequency Domain Method [81], Dobsons Method [82]. In this study, the Peak-Picking Frequency Domain Identification method has been chosen for modal parameter extraction. The structures used in this study are resonant and have linear behavior, thus the peak-picking method is used since it is simple to apply and the identified parameter are sufficiently precise with regard to the study case.

3.1 Frequency domain identification of structure

As mentioned above, the frequency domain identification method is used in this work. This section is dedicated to the theoretical basis to identify spatial and dynamic model. The frequency domain identification has been chosen because it can identify in a given frequency range. Indeed, the damping, the resonance frequencies and the modal shapes can be identified by tracking the mobility FRF of various point of the structure. Moreover, it is relatively faster and easy to implement using standard algorithm in Matlab. To this purpose, in this section firstly the modal model of structure is defined in frequency domain and modal parameters to be identified are highlighted. Afterward, the Peak-Picking method is introduced and its application to identify dynamic parameters is discussed. At end of the section, the identification of the mode shapes is presented using the Peak-Picking method. Special topics in spatial model identification, such as spatial resolution (sampling) criteria of identification and re-orthogonalization of the identified non-orthogonal modes are discussed. Finally the identification result of an example is presented.

3.1.1 Modal model of haptic display in frequency domain

Previous chapter showed that the elastic equation of vibration of a medium can be decoupled to infinite number of second order ordinary differential equations (ODEs). The frequency response of mode k is obtained by taking $s = j\omega$) in Eq. 2.24 which yields:

$$-\omega^2\ddot{\eta}_k(j\omega) + j2\zeta_k\omega\omega_k\eta_k(j\omega) + \omega_k^2\eta_k(j\omega) = \alpha_k v_p(j\omega),\ k \in \mathbb{N} \mid 1 \leq k < \infty \tag{3.1}$$

where ζ_k and ω_k are respectively the damping factor and natural resonance frequency of mode k, two dynamic parameter which will be identified with Peak-Picking method, α_k is the modal gain. We assume that in frequency band of excitation signal N_{mm} can be excited. Hence, we recall the modal representation of structure vibration in frequency domain as follow:

$$\boldsymbol{w}(x, j\omega) = \sum_{k=1}^{N_{mm}} \varphi_k(x)\eta_k(j\omega) \tag{3.2}$$

$\varphi_k(x)$ is the mode shape of k^{th} mode, the spatial parameter which will be discussed in identification of spatial properties section.

It is obvious that the spatial part of the modal representation, namely mode shapes $\varphi_k(x)$, is not affected by the time-frequency transformation. Only the temporal function $\eta_k(t)$ is transformed to $\eta_k(j\omega)$. The measurement of the vibration is supposed to be done with single spot doppler laser as a result the spatial model will be discrete. Hence the spatially discrete modal representation of vibration on structure for $x = x_n$ is as follow;

$$\boldsymbol{w}(x_n, j\omega) = \sum_{k=1}^{N_{mm}} \varphi_k[x_n]\eta_k(j\omega) \tag{3.3}$$

Where the brackets are used to stress that the mode shapes are sampled. Then substituting Eq. 3.1 into 3.3 yields;

$$\boldsymbol{w}(x_n, j\omega) = \sum_{k=1}^{N_{mm}} \varphi_k[x_n]\frac{\alpha_k v_p(j\omega)}{\omega_k^2 - \omega^2 + j2\zeta_k\omega_k\omega} \tag{3.4}$$

In this equation, $v_p(jw)$ is the excitation input voltage signal which should be properly defined to identify the dynamic parameters ζ_k and ω_k as well as spatial parameters of α_k and $\varphi_k[x_n]$.

3.1.2 Peak-Picking identification of dynamic parameters

One of the simplest structure identification method is Peak-Picking method. It is based on the fact that in n-degree of freedom system the frequency response function of the system experiences peak values of the FRF gain near to the mode frequencies of the system. By exciting the structure with a wide spectrum signal like as white-noise, impulse, sine sweep and etc, the modal parameter can be identified within frequency range of excitation signal. The peak-picking method is two steps procedure method, firstly the natural frequency of the modes are estimated, afterward the damping of the modes are identified.

- Resonance frequency of mode: The natural frequency of a mode is considered to be the peak value of gain FRF ;

$$\omega_k = \omega_{peak} \tag{3.5}$$

- Damping of the mode: The damping of the mode can be calculated from half power method. Meaning that the half power frequency of the mode are defined as

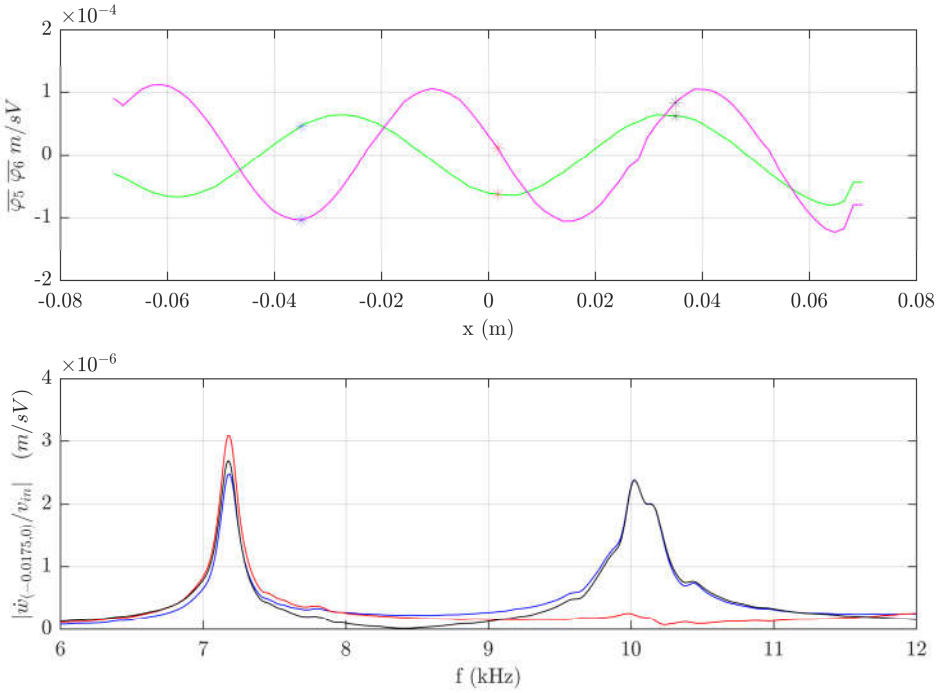

FIGURE 3.2: Comparing the FRF result of two measurement point of $x = 70\ cm$ in red and $x = 97\ cm$ in black

$\omega_{1,k}$ as lower frequency and $\omega_{2,k}$ as higher frequency of bandwidth of the mode. The damping of corresponding mode are estimated using resonance frequency and bandwidth of the mode as following equation;

$$\zeta_k = \frac{\omega_{2,k} - \omega_{1,k}}{2\omega_k} \tag{3.6}$$

As it is written in Eq. 3.4 the FRF depends on the position of measurement. As a consequence, some of the peak are not visible when measurement are taken on a node. To mitigate this problem, the FRF are taken at multiple location and a mean FRF is considered to estimate the resonance frequency and the damping factor.

3.1.3 Identification of spatial properties

The identification of spatial parameters of the structure are discussed in this subsection. It is assumed that the identification of spatial model is done by single point measurement as a result the mode shapes are discrete in space. First we present the criteria to avoid lost of information due the sampling. The second problem is that even if the

previous condition is respected, orthogonality of the modes can be lost and therefore post-treatment is required to restore this property.

3.1.3.1 Mode shape identification

According to the equation 3.4, and assuming that the modes are well decoupled in the frequency domain, it is possible to isolate one mode by exciting it at its resonance frequency. For instance, suppose the k^{th} mode is excited at the frequency $\omega = \omega_k$ the equation can be simplified by neglecting the other modes, and the real coefficients of denominator vanish. Thus, the vibration is approximated by:

$$\boldsymbol{w}(x_n, j\omega_k) \approx \varphi_k[x_n] \frac{\alpha_k v_p(j\omega_k)}{j2\zeta_k\omega_k^2} \tag{3.7}$$

by reorganizing Eq. 3.7, and since the excitation voltage $v_p(j\omega_k)$ is known, we can identify the mode shape $\varphi_k[x_n]$ up to a factor α_k :

$$\alpha_k \varphi_{k[x_n]} = \frac{j2\zeta_k\omega_k^2 \boldsymbol{w}(x_n, j\omega_k)}{v_p(j\omega_k)} \tag{3.8}$$

in order to apply this formula, it is assumed that ω_k and ζ_k are known. However, as the modes will be normalized afterwards this point is not so critical. Actually, in this work the laser vibrometer can only measure vibration velocity, therefore we used the following equation, which can be easily derived from Eq. 3.8:

$$\alpha_k \varphi_k[x_n] = \frac{2\zeta_k\omega_k \dot{\boldsymbol{w}}(x_n, j\omega_k)}{v_p(j\omega_k)} \tag{3.9}$$

As it is seen in Eq. 3.9, there is an indetermination, namely the amplitude of the mode shape can be determined only if the modal gain is known and vice versa. Therefore, one of them has to been chosen arbitrarily. If we wish to keep the orthonormality of the modes as exposed in previous theory, one has to impose the property $< \overline{\varphi}_k(x_n), \overline{\varphi}_k(x_n) >= 1$, and then it follows that $< \alpha_k\overline{\varphi}_k[x_n], \alpha_k\overline{\varphi}_k[x_n] >= \alpha_k^2$. In this case, we can calculate α_k by:

$$\alpha_k = \sqrt{\rho A \int_{-\frac{l_x}{2}}^{\frac{l_x}{2}} \left(\frac{2\zeta_k\omega_k \dot{\boldsymbol{w}}(x_n, j\omega_k)}{v_p(j\omega_k)} \right)^2 dx} \tag{3.10}$$

where A is cross section of beam. In practice, this expression must be implemented using trapezoidal approximation of the integral. Supposing that the surface of the structure (haptic display) has been discredited into $N+1$ regularly spaced measurement points in the x direction,one can write;

$$x_n = X_{min} + (n-1)\Delta X, \qquad \Delta X = \frac{l_x}{N}, \qquad 1 \leq n \leq N+1 \tag{3.11}$$

where, l_x is the length of structure in X direction. Eq. 3.10 thus is approximated as;

$$\alpha_k = \frac{2\zeta_k\omega_k}{v_p(j\omega_k)}\sqrt{\rho A\frac{l_x}{2N}\sum_{x=1}^{N}(\dot{\boldsymbol{w}}^2[x_n, j\omega_k] + \dot{\boldsymbol{w}}^2[x_{n+1}, j\omega_k])} \tag{3.12}$$

Using Eq. 3.13, the modal gain α_k can be extracted from measured vibration velocity field. In practice, this estimation of the modal gain may be cumbersome and biased by noise. So that, in this work the normalization was defined by:

$$\frac{\dot{\boldsymbol{w}}[x_k, j\omega_n]}{max(|\dot{\boldsymbol{w}}[x_k, j\omega_n]|)} = \frac{\frac{\alpha_n v_p(\omega_n)}{2\zeta_n\omega_n}\dot{\boldsymbol{w}}[x_k, j\omega_n]}{|\frac{\alpha_n v_p(\omega_n)}{2\zeta_n\omega_n}|max(|\dot{\boldsymbol{w}}[x_k, j\omega_n]|)} = sign(\alpha_n)\frac{\varphi_n[x_k]}{max(|\varphi_k[x_k]|)} \tag{3.13}$$

We arbitrarily assume that the modes maximum amplitude is always positive. So that, the maximum amplitude of the normalized mode is always one, therefore the sign of the gain can be positive or negative accordingly. In practice the gain is then evaluated by selecting the highest velocity of the mode and applying:

$$\alpha_n = \frac{2\zeta_n\omega_n}{|v_p|}max(|\dot{\boldsymbol{w}}[x_k, j\omega_n]|) \tag{3.14}$$

3.1.3.2 Spatial resolution of mode shape identification

As mentioned in the previous subsection, due to measurement constraints, the spatial identification of the structure is sampled. As a consequence, the mode shapes are discretized, and some accuracy will be lost which can deteriorate the precision of the model.

As it was discussed in the previous chapter, the objective of this thesis is to use limited number of modes to excite a desired spatial form of vibration. Moreover, we have restrained the study to the cases of the beam and the plates. For such geometries,

the mode shapes are roughly combination of sinusoidal functions. So we can consider a spatial wavelength for mode shapes at the highest frequencies of identification. With this approximation, we can refer to the Nyquist sampling criterion. let ΔX be the spatial sampling period, and λ is the shortest spatial wavelength of the highest frequency mode, then we can write:

$$\Delta X < \frac{\lambda}{2} \tag{3.15}$$

In fact, this is the necessary condition (minimum spatial sampling condition) and not the sufficient criteria of spatial sampling. In order to obtain a precise spatial model, the spatial sampling should be even smaller than this criteria.

3.1.3.3 Post-Processing of mode shapes; Orthogonalization of Non-Orthogonal Modes

In practice, the orthogonality of the identified mode shapes is not exactly verified. This can be induced by sampling itself. The sampling distance can be reduced, while it would be time and resource consuming. Measurement errors can also induce such problems. In such cases, the modes shapes are not independent and the linear summation of the modes in Eq. 2.21 to generate desired form is not valid anymore. In fact, the resulted modal coefficient for a given vibration form using modal decomposition of non-orthogonal modes include an error which is due to the cross talk of the modes. In order to overcome this problem, a set of orthogonal modes should be generated using the identified modes and applying a orthogonalizing technique such as Gram-Schmidt algorithm.
The Gram-Schmidt process is a method for orthonormalising a set of vectors (mode shapes) equipped with an inner product finite space. The Gram-Schmidt takes a finite set of linearly independent mode shapes $(\varphi_1, \varphi_2, ..., \varphi_k)$ and generates an orthogonal set of modes shapes $(\varphi_1^\dagger, \varphi_2^\dagger, ..., \varphi_k^\dagger)$.

The projection operator is defined as follows:

$$proj_{\varphi_i}(\varphi_j) = \frac{< \varphi_i, \varphi_j >}{< \varphi_i, \varphi_i >} \varphi_i \tag{3.16}$$

The Gram-Schmidt is an iterative procedure, where the first orthogonal mode $\varphi_1^\dagger$ is equal to the mode φ_1, The rest of the orthogonal modes being generated as below:

$$\varphi_1^\dagger = \varphi_1 \tag{3.17a}$$

$$\varphi_2^\dagger = \varphi_2 - proj_{\varphi_1^\dagger}(\varphi_2) \tag{3.17b}$$

$$\varphi_3^\dagger = \varphi_3 - proj_{\varphi_1^\dagger}(\varphi_3) - proj_{\varphi_2^\dagger}(\varphi_3) \tag{3.17c}$$

$$\varphi_k^\dagger = \varphi_k - \sum_{j=1}^{k-1} proj_{\varphi_j^\dagger}(\varphi_k) \tag{3.17d}$$

The orthogonalized modes can then be normalized in order to apply in the modal projection as in Eq. 3.18.

$$\overline{\varphi_k^\dagger} = \frac{\varphi_k^\dagger}{||\varphi_k^\dagger||} \tag{3.18}$$

3.2 Experimental study case of frequency domain identification of modal parameters

The presented frequency domain identification methods in previous subsection has been utilized to identify a simple structure. A beam has been used for this purpose, the reason of choosing beam is its limited survey area which reduces the number of measurement point of vibration and in return reduce the identification measurement process time. In this section, the excitation signal for identification and obtained measurement result and modal parameter are presented. As it was mentioned earlier, the identified mode shapes are normally affected with noise and cross-talk of other modes. This is the case for this study, thus Gram-Schmidt orthogonalization is applied to identified modes and orthogonal sub-space is achieved at the end of this section.

3.2.1 Experiment setup and study case of identification

In this experiment the setup is an aluminum structure with dimension of $l_x = 105\ mm$ of length, $l_y = 7\ mm$ of width and $h = 1\ mm$ of thickness has been considered as shown in Fig. 3.3. Clamped-Clamped boundary conditions are imposed by bolting the

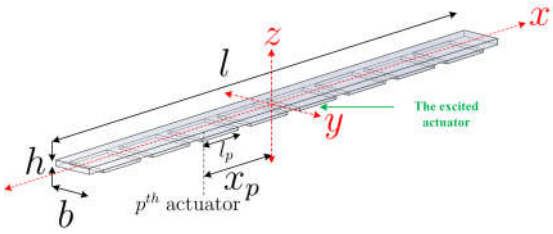

FIGURE 3.3: Schematic of beam used in identification

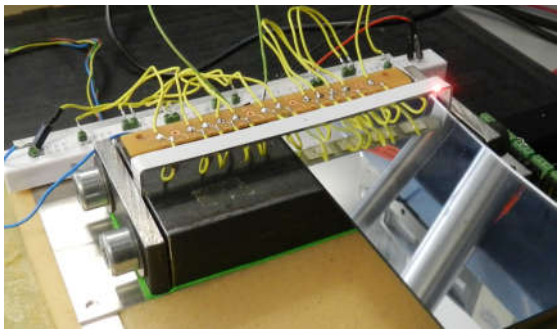

FIGURE 3.4: Photo of realized beam

structure to a heavy and rigid chassis of steel. The setup is depicted in Fig. 3.4. eight piezoelectric transducer have been laminated to the beam as shown in the same figure. Only one of actuator has been excited during identification experiment, the actuators were used to increase modal gain during the focusing experiment. This actuator was selected on the basis of finite element simulation which showed that it was coupled to the modes of interest. A single spot doppler laser vibrometer is used to measure vibration of at the sampled points on the beam.To do so the setup is mounted on a XY table.

3.2.2 Excitation signal

In this identification test the excitation force is produced by, the piezoelectric actuator for the identification procedure. There are two reasons for that; firstly the piezoelectric actuator has a large bandwidth and therefore it is enough to identify the modes of interest. Secondly, it asses the ability of actuator to excite the required mode. Many excitation force can be generated with piezoelectric to run identification tests such as: sinusoidal excitation, Chirp, white noise excitation and so on. Even if, theoretically the FRF does not depend on the excitation force, in practice the precision and quality of FRF does depend on the signal to noise ratio. With random excitation this condition requires long measurements. On the other hand, with deterministic method, a chirp signal provides enough power to compensate the measurement noise. So in this case, since FRF at each sampling points must be acquired. Thus, a linear sine sweep voltage signal is define to be applied to the actuators as below;

$$v_{in}(t) = \begin{cases} V_{in} sin(2\pi f_{v_{in}}(t)t), & 0 \leq t \leq T_{sweep} \\ 0, & t \geq T_{sweep} \end{cases} \tag{3.19}$$

$$f_{v_{in}(t)} = (\frac{f_H - f_L}{T_{sweep}} t + f_L) \tag{3.20}$$

where, V_{in} is the amplitude of excitation signal in $Volt$, f_L and f_H are the lowest and highest frequency range of identification band and T_{sweep} is the time duration to pass from lowest frequency f_L to highest frequency of excitation f_H. T_{sweep} should be defined large enough whereby the modes with high damping factor be well excited. The blue curve in fig. 3.6 shows the excitation voltage applied to the actuator with 30 V $pk-pk$ amplitude, time duration of $T_{sweep} = 250$ $msec$ and $f_L = 100$ Hz and $f_H = 100$ kHz. There are two important criteria in determine excitation signal as well as measurement which are explained in the next two subsection.

One important point is the bandwidth $\times$ time product. For given values, the excitation spectrum tend to a rectangular spectrum which guarantees that all modes on the bandwidth are correctly excited. As illustrated in Fig. 3.5, four chirp signals spanning the same frequency band of 100 kHz with different sweep time have different Fourier transform. By increasing the sweep time, the FFT of the chirp become shaper and the ripples are more prominent near the end frequencies. The Fourier transform of excitation signal of test corresponds to the blue curve in the same figure. This choice was made not only to obtain an homogenous excitation for all the excitation frequency band, but also to guarantee the frequency resolution which will be discussed later.

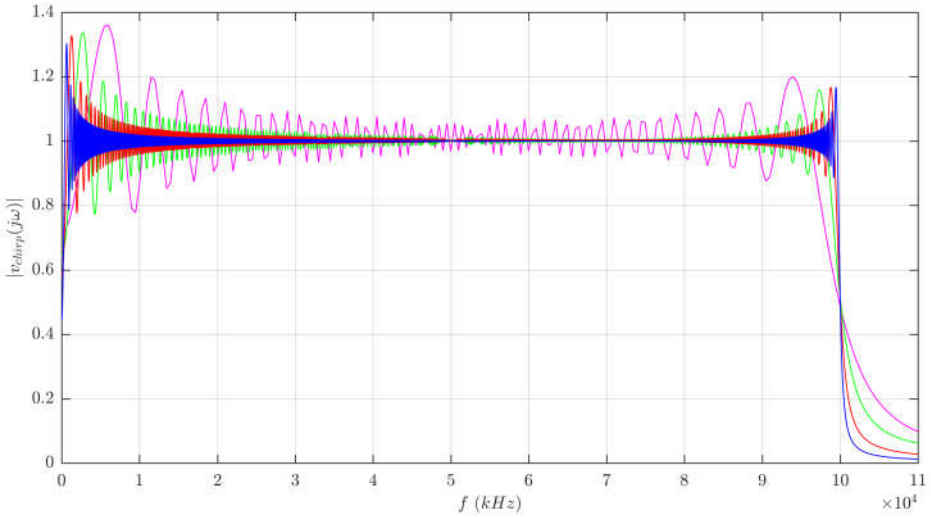

FIGURE 3.5: Comparison of Chirps signal excited in frequency domain for the same amplitude and same frequency range but different time periods; $T_{sweep} = 2$ ms purple color,$T_{sweep} = 10$ ms green color, $T_{sweep} = 50$ ms red color and $T_{sweep} = 250$ ms blue color plot

3.2.3 Frequency domain resolution of FRF

The peak-picking method is applied in the frequency domain. Therefore, some constraints on the sampling frequency and the duration and the length of the acquisition have to be verified.

According to the Shanon's sampling criterion, the sampling frequency must at least be twice the highest frequency of the acquired signal. In the case at hand, since this chirp signal's highest frequency is known, we chose experimental sampling frequency of excitation signal ten time higher than f_H to ensure an accurate dynamic response measurement of the structure.

The measured temporal data are transformed to frequency domain using Fourier transformation. Then the identification method is applied and parameters are extracted. As all the measured data are discrete in time, inevitably the FRFs are discrete as well. The resolution of FRFs in frequency domain is crucial to accurately identify the resonance frequencies and the damping factor. Hence, the FRFs should have enough resolution to identify correctly parameters. It can be proven that the frequency resolution of FRF δf is inversely proportional to duration of the sampled signal. Here again it coincides with parameter of the chirp signal, namely T_{sweep}. That is in our test with as sweep time of 250 msec (in the test, the excitation and measured signals have the same time length) T_{sweep} where by the FRFs resolution is 4 Hz.This latest choice, is made with some prior knowledge from the FEM simulations which indicated that the first resonance will be around 400 Hz, thus a quality factor Q of 100 can be detected.

3.2.4 Obtained results

The experiment was run with the defined sine sweep signals. The surface of the beam were scanned with single spot laser vibrometer and measured temporal vibration velocity was measured and recorded using Picoscope oscilloscope and Matlab software. Measured vibration velocity for one of the point on the beam is shown in red color in Fig. 3.6. The peaks in this curve, shows the times that excitation signal is in the resonance frequency of mode.

All excitation and measured vibration velocity signals have been converted to the frequency domain applying Fourier transformation. The chirps excitation signal is shown in blue curve in Fig. 3.7 in frequency domain. As it is observable the excitation covers the frequency range from 100 Hz to 100 kHz with peak-peak amplitude of 30 Volts.

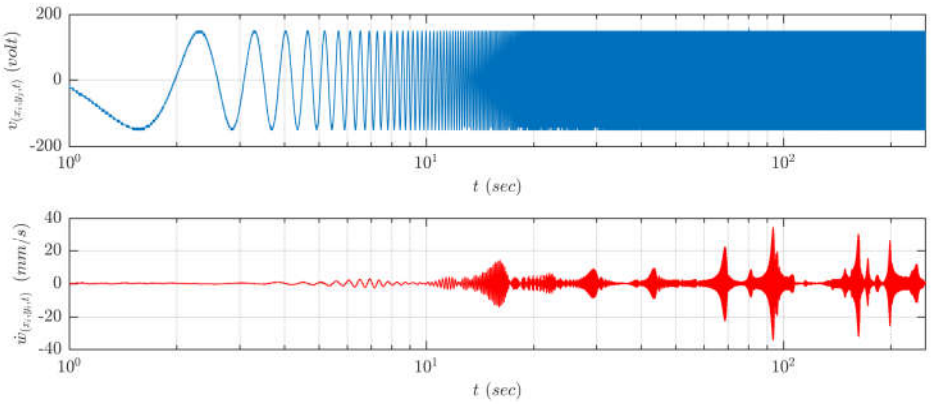

FIGURE 3.6: **Top.** Excitation sine sweep signal applied to the actuator **Bottom.** Measured signal of vibration velocity for a given point on the beam

This ensures that the actual displacements are small in order to avoid nonlinearities of the modes of the beam at the resonance. The measured vibration velocity field of a single point on the beam is shown in red curve in the same figure. Each peak on this curve corresponds to one mode of the structure and the frequency of corresponding peak is a resonance frequency of the beam (Unless the measurement points are on the node of particular mode). The mobility FRF, that is the force to vibration velocity transfer function, is calculated by dividing the velocity FFT by the excitation chirp FFT.

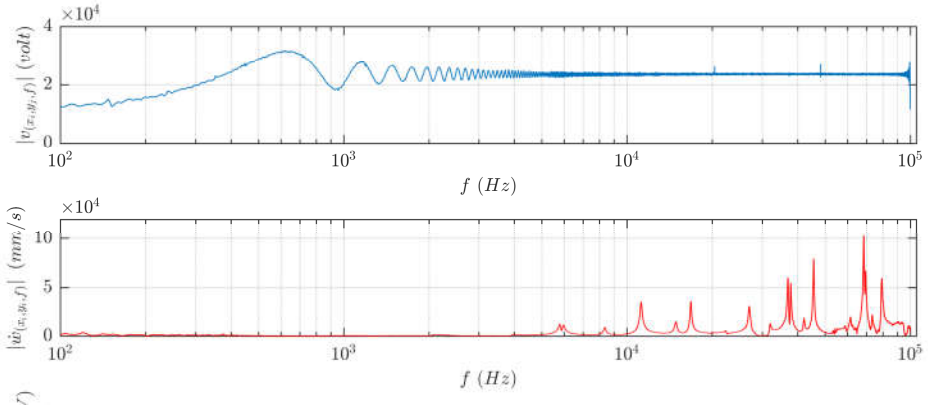

FIGURE 3.7: **Top.** Fourier transform of excitation Chirp signal. **Below.** Frequency domain response of structure to the Chirp excitation.

The curves in Fig. 3.8, depict the FRF at three different locations on the beam. One can notice immediately, that the peak have different heights according to their location of measure. This is due to the mode shapes as can be justified according to Eq. 3.7. An algorithm has been developed which search local maximums of FRF by a given threshold. It automatically identifies the resonance frequencies as depicted in Fig. 3.8 by red stars. Afterward, using each resonance frequency a neighbour band of frequency

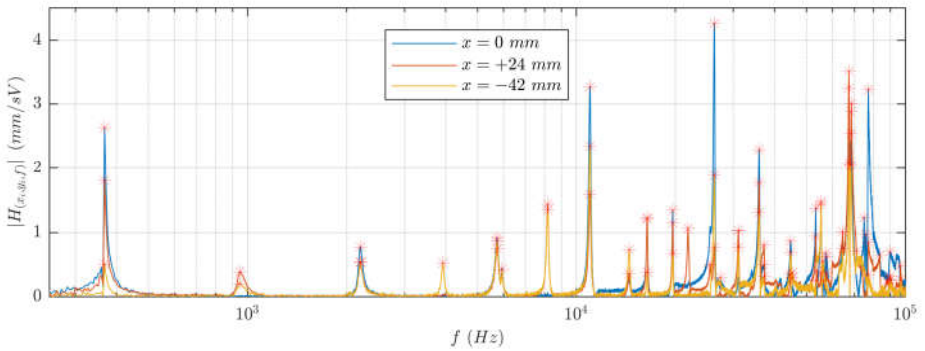

FIGURE 3.8: The mobility FRF of the

is chosen and isolated from the rest of FRF function. Then, the half power bandwidth is interpolated nearby the identified resonance frequency which yield to damping estimation. The damping factor is identified using half power method in Eq. 3.6, where the half power points $(Q/\sqrt{2})$ on the FRF are detected and corresponding frequency are noted as $f_{(1,k)}$ and $f_{(2,k)}$ (low bandwidth and high bandwidth frequencies). By applying Eq. 3.6 the damping factor is identified for k^{th} mode. Fig. 3.9 illustrated one example of identifying resonance frequency and half power band. In this figure, the red vertical line shows the peak of the FRF and corresponding resonance frequency. The green and blue lines are the points on the FRF where the amplitude arrives to half power. The frequency values on horizontal axis for green and blue lines show $f_{(1,k)}$ low bandwidth frequency and $f_{(2,k)}$ high bandwidth frequencies, respectively.

The result of the identification process for the studied experimental structure is given in 3.1. It should be noticed that the method is limited to the ability of actuator to excite the modes. Here for instance, mode 18 cannot be identified due to the fact that it is not controllable with the actuator that the structure was excited during identification test.

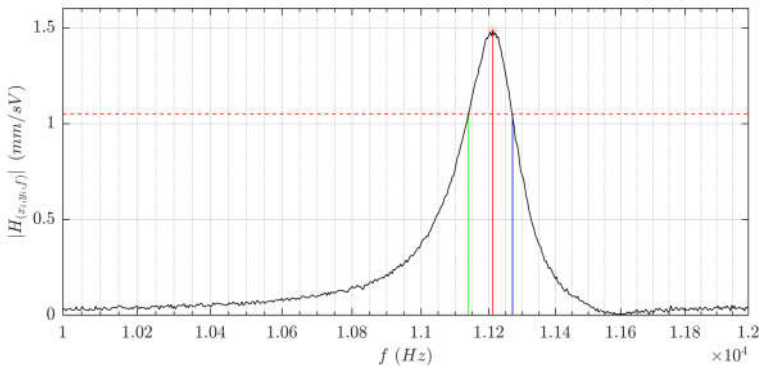

FIGURE 3.9: FRF around one resonance frequency and identifying half power band

Mode N.	f_E kHz	Damping	Gain (mm/(sV))
1	0.368	11.77 $\times 10^{-3}$	15.84 $\times 10^{+3}$
2	0.963	22.84 $\times 10^{-3}$	31.59 $\times 10^{+3}$
3	2.253	28.62 $\times 10^{-3}$	81.05 $\times 10^{+3}$
4	3.907	15.10 $\times 10^{-3}$	92.67 $\times 10^{+3}$
5	5.719	10.40 $\times 10^{-3}$	88.62 $\times 10^{+3}$
6	8.166	9.18 $\times 10^{-3}$	259.99 $\times 10^{+3}$
7	10.942	9.64 $\times 10^{-3}$	726.43 $\times 10^{+3}$
8	14.355	11.55 $\times 10^{-3}$	596.08 $\times 10^{+3}$
9	16.327	7.16 $\times 10^{-3}$	490.08 $\times 10^{+3}$
10	21.801	8.94 $\times 10^{-3}$	612.61 $\times 10^{+3}$
11	26.121	8.80 $\times 10^{-3}$	1101.05 $\times 10^{+3}$
12	30.888	5.82 $\times 10^{-3}$	723.82 $\times 10^{+3}$
13	37.100	16.91 $\times 10^{-3}$	985.67 $\times 10^{+3}$
14	41.449	11.21 $\times 10^{-3}$	730.42 $\times 10^{+3}$
15	44.551	10.88 $\times 10^{-3}$	1015.78 $\times 10^{+3}$
16	54.605	16.39 $\times 10^{-3}$	1666.20 $\times 10^{+3}$
17	67.351	7.27 $\times 10^{-3}$	1496.10 $\times 10^{+3}$
18	Not controlable	—	—
19	74.863	7.21 $\times 10^{-3}$	1072.37 $\times 10^{+3}$
20	89.927	15.12 $\times 10^{-3}$	1396 $\times 10^{+3}$
21	96.587	6.66 $\times 10^{-3}$	545.63 $\times 10^{+3}$

TABLE 3.1: Table of Dynamic Parameter of Modes

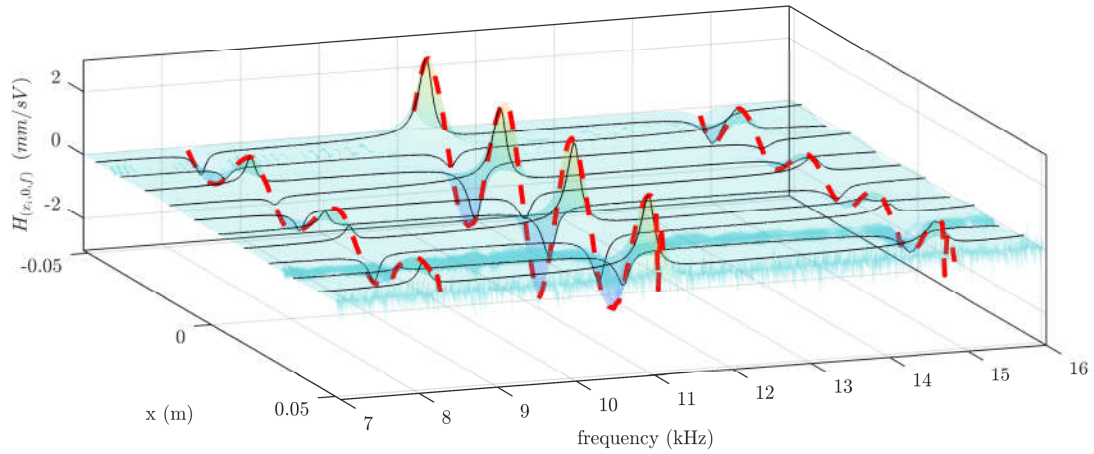

FIGURE 3.10: Illustration of transfer function of beam on its central line in spatio-Frequency domain

3.2.4.1 Mode shape identification

Refering to the beam schematic presented in Fig. 3.3, we consider the mid line passing from center of beam in x direction (red dashed line in x direction). The transfer function of each measured point is plotted next to each other to build. The obtained identification data is depicted in space-frequency figure as it is shown in Fig. 3.10. In this figure, the

axis labeled with x is the position in the length of beam as shown in Fig. 3.3 red line and the axis labeled with frequency is the response of the structure in space for the excitation in corresponding resonance frequency. The black lines are the transfer function of some of the points on the beam and the transparent colored surface is the interpolated transfer function between all the measured point. By linking the frequency peaks in direction of the x we will obtain the dashed red lines which are the mode shapes coupled with modal gain $\alpha_k \varphi_{k[x_n]}$. Referring to the red dashed lines in Fig. 3.10, the form of 6^{th}, 7^{th} and 8^{th} modes are observable. To sum up, the mode shapes and modal gain parameters can be extracted from the transfer functions measured at specific location on a grid points and peak-picking method when vibration field is plotted in a space frequency figure. The procedure can be used for plate, by using a similar graph for the remaining dimension.

Using Eq. 3.13, the modal gain value can be extracted, the obtained modal gain values are presented in Table 3.1. For the measurement of the these mode shapes, spatial sampling was of 1 mm in both x and y directions. This choice has been made to obtain minimum five measurement point for highest resonance mode (Mode 21) on the given structure.

3.2.4.2 Orthogonalization of Mode shapes

Regarding to the identified mode shapes, unusual deformation are detected after mode 12^{th}. This can be verified by orthogonality check of the modes using following formula:

$$< \varphi_k \varphi_n >= \frac{l_x l_y}{(4NM)} \sum_{x_i=1}^{N} \sum_{y_j=1}^{M} \varphi_k[x_i, y_j] \varphi_n[x_i, y_j] m[x_i, y_j] \tag{3.21}$$

The self-correlation factor of the real modes of structure are shown in Fig. 3.11. left. Here in this figure, the yellow color shows the complete correlation and dark blue color shows complete orthogonality. There are modes that have cross-talk between each other, an example is mode 13 and mode 14. Thus, the Gram-Schmidt orthogonalization technic in Eq. 3.17a has been applied to the first sixteen identified modes in Fig. 3.13.

The obtained orthogonalized mode shapes are depicted in color in Fig. 3.12 and their identified values are depicted in gray color in the same figure. The orthogonalized mode, have been self-projected as described in Eq. 3.21 and their self-correlation factor is presented in Fig. 3.11. It is noticeable in this figure that the modes are completely

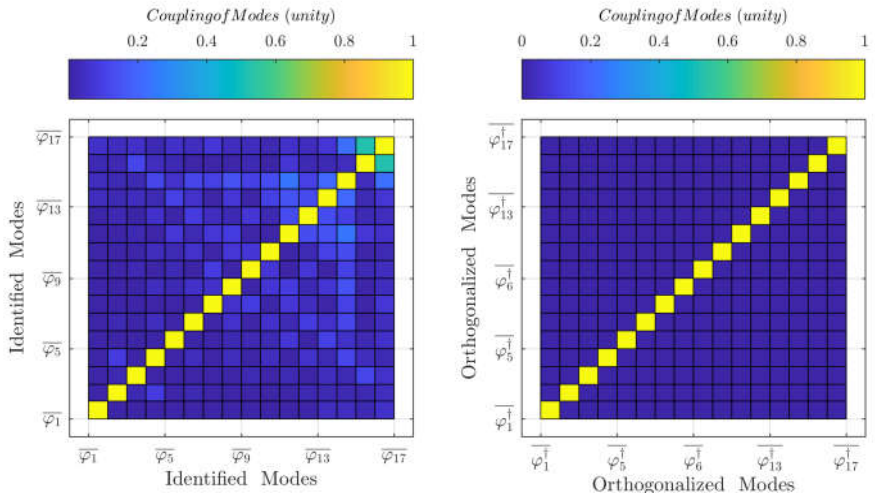

FIGURE 3.11: **Left:** The cross talk factor between identified modes of beam. **Right:** The cross talk between orthogonalized mode shapes using Gram-Schmidt method.

orthogonal. It can be observed that orthogonalization has modified the mode shapes, particularly for the higher order modes. This modification reject the noise error and more specially cross talk error in mode shape identification and yields an orthogonal basis.

3.2.4.3 Conclusion

This chapter was dedicated to introduce an identification procedure to determine the dynamic model of a vibrating structure. Due to the fact that the model of the structure is required for a given bandwidth, a frequency domain identification method namely peak-picking method has been selected due to its simplicity and sufficient accuracy in our case (which is lightly damped structure). The corresponding mathematical theory, has been developed to identify resonance frequency, damping factor and modes shape of the structures.

The necessary criterion for spatial discretization, sampling of temporal excitation signal, and frequency resolution of FRFs have been discussed in order to obtain an accurate identification. The problem of losing orthogonality of modes due to the discretization has been explained and an orthogonalization method has been proposed to address problem. Finally, the identification methodology has been validated with an experimental identification study.

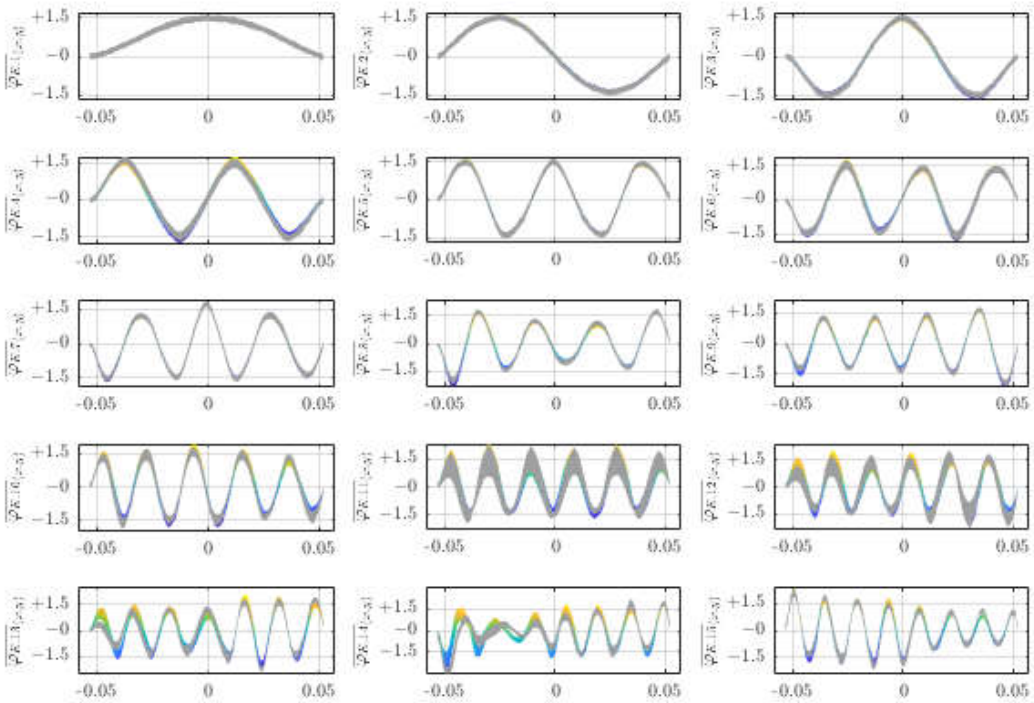

FIGURE 3.12: Orthogonalized mode shapes of beam using Gram-Shmidt method depicted in color and identified mode shapes depicted in gray

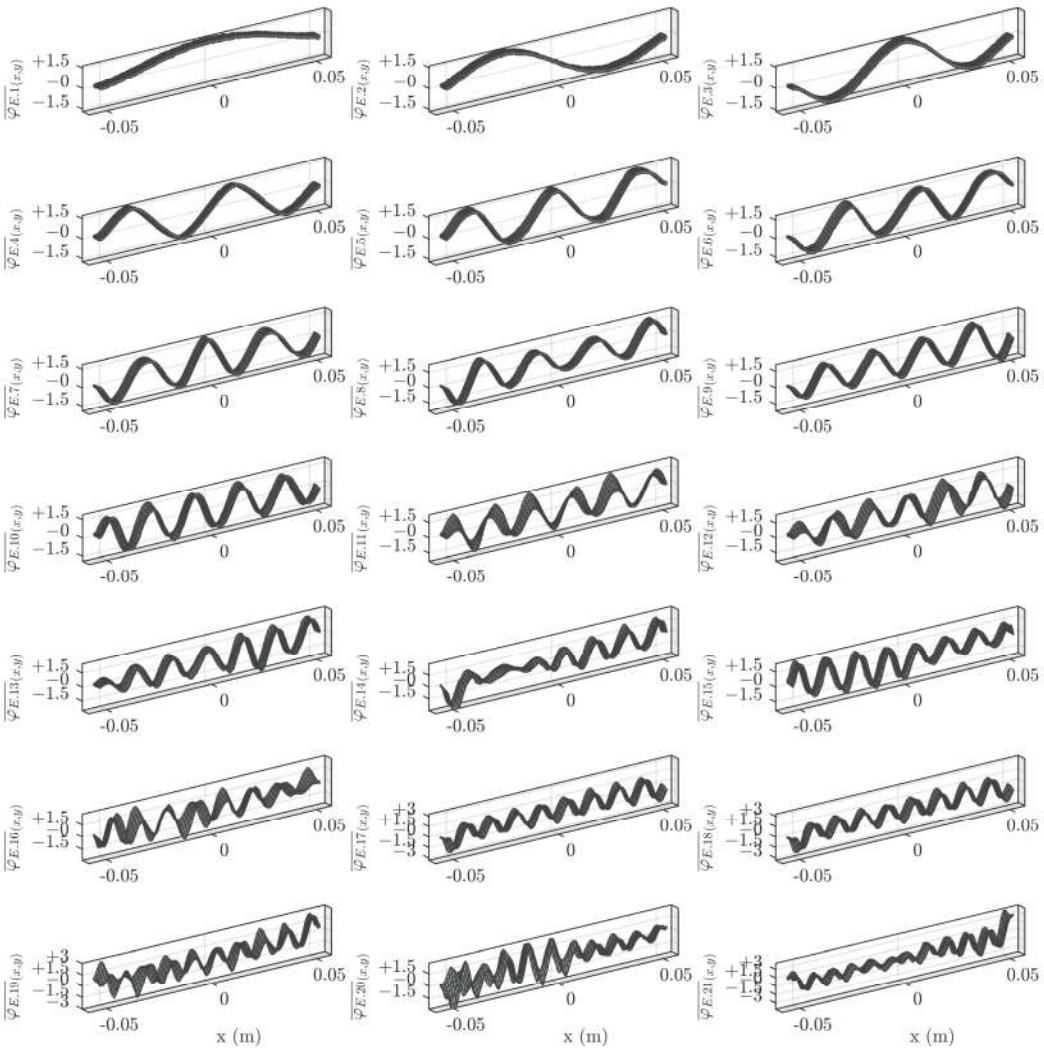

FIGURE 3.13: The identified mode shapes of beam for frequency range of 100 Hz − 100 kHz

Chapter 4

Experimental Validation of Local Deformation Stimulation On Haptic Display

In this chapter a set of experiments have been developed to verify the feasibility of spatial control of vibration on the simple haptic display. In fact, the presented modal model in chapter 2 and the identification technique in chapter 3 have been used to model the spatial behavior of the experimental cases. Utilizing the model, the feasibility of exciting predefined spatial form of vibration is investigated experimentally. For this experiment study, the spatial form is considered to be pulses and it is due to the application of haptic display which is considered to excite local vibration (local haptic feeling). To this end, several prototype have been developed whose experiment objective as well as mechanical properties differ from each other.

- The objective of first experiment case is to verify possibility of focusing vibration in different location on the beam. This has been realized with exciting sinc pulses whose pulse center are in different location on the beam.
- The second prototype is dedicated to analyze possibility of exciting different spatial form using modal decomposition method. So that, a mechanical design has been realized whereby multiple number of the modes can be excited. Thanks to its capability of exciting several modes, the possibility of exciting different spatial form has been investigated using modal method.

- A third prototype has been developed to study haptic feedback of the excited spatial form. To this end, a smart structure has been designed in a way that the vibration amplitude can achieve the level of human tactile perception.

This chapter puts in evidence how to start with a smart structure with its modal model and apply the modal decomposition to render desired vibration field. The topics like as how to determine reduced modal model and required criteria is studied. As well as, how to determine the excitation voltage signals of actuator to excite a given spatial form is studied experimentally in this chapter.

The main objective of this chapter is to arrive from equilibrium point to desired spatial form of vibration by properly exciting the required vibration modes of the smart structure. Thus, the experimental measurement results are organized in a way to illustrate the final spatial form (in Time-space domain) obtained by experiment and modal coefficient values of each mode at final moment (in Time-Mode domain).

As it is depicted in Fig. 4.1, the problem of this thesis is explained in space, time and frequency (domain). The objective of this chapter, is represented by the colored surface in space-time plane of this figure. This is obtained by properly exciting the modes to achieve the spectrum as shown with green bars in time-frequency plane in Fig. 4.1. Hence these two representation in the physical and modal spaces will be recalled during result validation in this chapter.

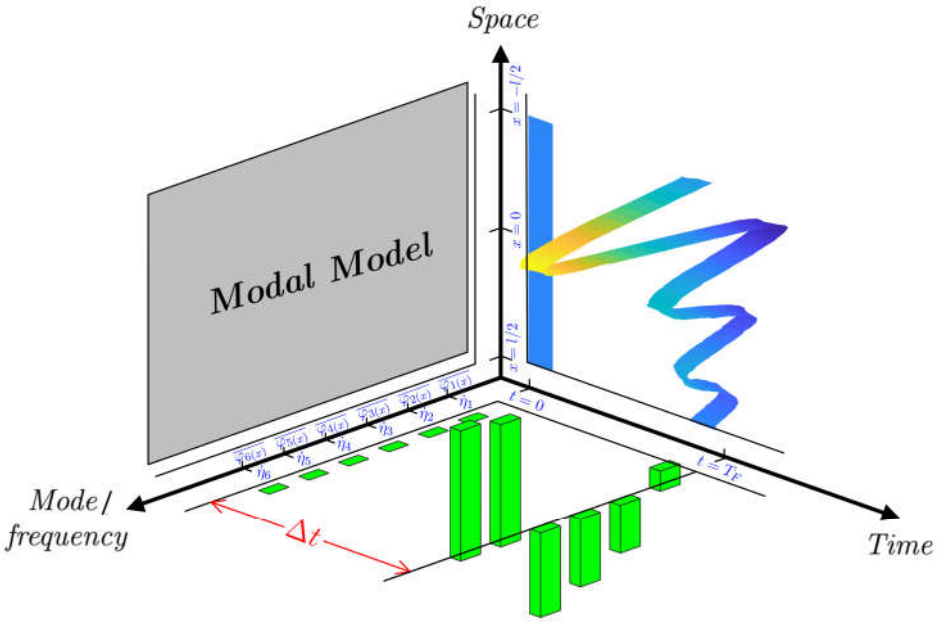

FIGURE 4.1: Space-Time-Modal schematic of problem; objective of this chapter is to obtain desired spatial form by a proper excitation of modes

This chapter is organized in six sections. The experiment test bench and test protocols are defined in first section. The experimental setup and feasibility of exciting desired spatial form with different pulse center (focusing vibration in different location on the beam) is presented in second section. The possibility of exciting different spatial form, namely exciting pulses with different form and pulses with different pulse width, is studied in third section. The temporal issues of how to excite a mode, dynamic of mode and transient of vibration is discussed in section three. The obtained results are discussed in section five, consequently some improvement is proposed and validated in section six.

4.1 Test bench and experiment protocols

In order to realize the experiments, a test bench have been developed as shown in Fig. 4.2. This test bench includes simulation and experimental setups whose results are fully processed in the Matlab software. The software setup includes FEM simulation of structure for determining mode shapes and dynamic behavior. The FEM software result is exported to Matlab via Python interpretation as shown in Fig. 4.2.

The experimental setup includes excitation and measurement loops. The excitation part includes a signal generator which is responsible of generating the reference voltage signal. The generated signals are amplified utilizing power amplifiers to reach adequate level to excite the smart structure. The measurement loop includes a single spot leaser whose measured data are transferred to matlab via an oscilloscope. In the experimental setup Matlab software is used as central organizer infrastructure to run automatically

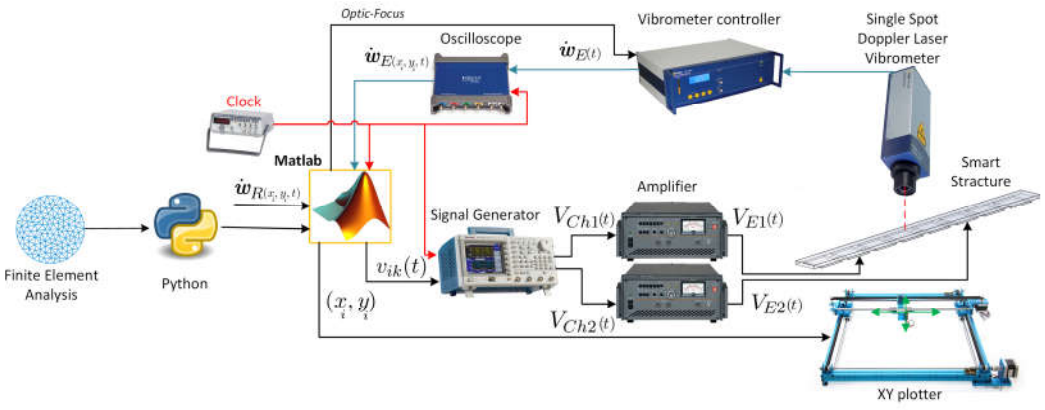

FIGURE 4.2: Schematic of test bench

all experiment including exciting the haptic display and measuring the vibration field. For exciting each spatial velocity field $\dot{\boldsymbol{w}}_{R(x_i,y_j,T_F)}$, the voltage signal of each actuator $v_{kR(t)}$ is calculated by Matlab using presented theory in section 2.34 for all experiment. The reference voltage of the actuators are delivered to the signal generator (Tektronix AFG 3202) and after amplification of signal in electric power amplifier (NF HSA 4051) the excitation voltage $v_{kE(t)}$ signals are applied to each actuator of haptic display. Matlab supervise the measurement process of experiment. The single spot Doppler laser vibrometer (Polytec OFV 5000) measures the vibration velocity $\dot{\boldsymbol{w}}_{R(x_i,y_j,T_F)}$ for each point of structure (x_i, y_j). The measured signal is deliver to Matlab via Picoscope 3403 oscilloscope. This measurement is repeated by Matlab in order to survey all the surface of the haptic display and determine the spatial vibration field of structure whereby a xy-plotter moves the structure under the fixed laser to collect the vibration information of predefined points (x_i, y_i). The command signal of (x_i, y_i) to move xy-ploter is determined by Matlab as well. The excitation, measurement and Matlab software are synchronized using an external clock, as shown with red line in the figure. Meanwhile, Matlab has communication with controller of laser vibrometer to improve signal to noise ratio during the measurements (by two ways; firstly repeating measurement of vibration at each point and calculating the means value, secondly; Re-focusing of the laser). After measurement of vibration of some points on the structure, the temporal vibration field of structure $\dot{\boldsymbol{w}}_{E(x,y,T_F)}$ is determined by Matlab.

Briefly, during the experiment following milestones has been considered as experiment protocols;

- The reference spatial forms have been defined for the structure.
- The FEM model of the structure is developed and it ability to excite spatial form is investigated in simulation case.
- The prototype of the structure is realized and its modal parameter are identified.
- The desired spatial form is projected into identified mode shapes to obtain the modal coefficient of each spatial form
- The modal model corresponding desired spatial form is reduced to excite limited number of modes.
- Using the reduced model, the modal approximation of spatial form is obtained $\dot{\boldsymbol{w}}_{M\,(x,T_F)}$

- The voltage excitation signals of the actuators are defined V_{iR} and are applied to actuator via signal generator and amplifier.
- The measurement setup measures the temporal evaluation of vibration field on the structure, as it was explained at the first of this subsection, and measured spatial form at end transient $\dot{\boldsymbol{w}}_{E\,(x,T_F)}$ is obtained.
- The defined reference spatial form, modal spatial form and experimental spatial form of all experiment are compared in spatial and modal domains.

4.2 Local Deformation Excitation on Beam

This section is to study possibility of focusing vibration on different location on the beam. The aim is to use a single actuator which is responsible of exciting multiples of modes to generate local vibration. To this end, a beam with the length of 140 mm and the width and thickness of 6 mm and 5 mm has been considered. The boundary condition of the beam supposed to be pinned-pinned. Fig. 4.3 shows the schematic of this beam. An experiment has been prepared whose objective is to excite pulses in different location on the beam, these spatial specification is presented in below subsection (4). The prototype and obtained simulation and experimental result are discussed in subsection 4.

4.2.1 Objective (Spatial specification of local vibration)

In order to investigate the feasibility of exciting local vibration (focusing) with modal synthesis of vibration, sinc (cardinal sine) function has is chosen as desired spatial form.

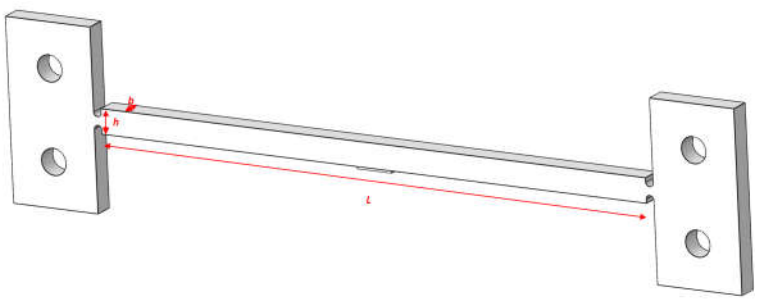

FIGURE 4.3: Schematic of Rython Beam

The sinc function is well known to have band limit spectrum which is constructible with limited number of sinusoidal harmonic. An example is the sinc electrical signal (which is a sinc function of time domain), the Fourier series of temporal sinc function is a square window in frequency domain (spectrum is band limited) which permits to construct as sinc function with limited number of eigenfunction and high precision of signal. The fact of exciting spatial sinc in space is analog to Fourier series and sinc function in time, if and only if the structure have sinusoidal mode shapes as eigenfunctions of Fourier series. Then, spatial sinc function can be reconstructed using limited number of the mode shapes (eigenfunctions of structure) which causes to model reduction of haptic display and utilize limited number of modes to excite experimentally. The desired vibration field, spatial sinc, is defined using Eq. 4.1a.

$$\dot{\boldsymbol{w}}_{R.PW.Sinc\,(x,T_F)} = A_{sp} Sinc\left(\frac{3}{2PW_{sp}}(x - x_{Csp})\right) \quad where \tag{4.1a}$$

$$Sinc(x) = \frac{sin(\pi x)}{\pi x} \tag{4.1b}$$

where, A_{sp} is the amplitude of Sinc in its maximal point on space, PW_{sp} is the spatial

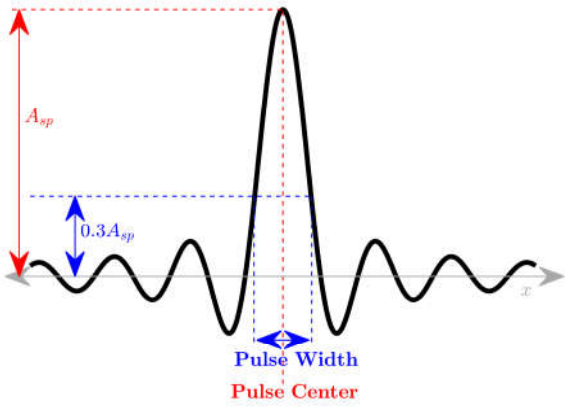

FIGURE 4.4: Spatial Sinc pulse and definition of *Spatial Pulse Width*, *Spatial Pulse Amplitude* and *Spatial Pulse Amplitude*

sinc pulse width, x_{Csp} is the spatial location of sinc pulse center and $\dot{\boldsymbol{w}}_{R.PW.Sinc\,(x,t_F)}$ is reference spatial sinc deformation at the end transient (focusing moment T_f) with pulse width of PW. The spatial sinc function and its parameter are illustrated in Fig. 4.4. According to this figure, the pulse width is defined from 30% of the pulse amplitude of A_{sp}.

Number of experiments have been prepared to investigate the feasibility of objectives; firstly addressing sinc pulse center x_{Csp} using modal vibration rendering. The detail of these experiments is discussed in future subsections.

4.2.2 Design of prototype

To perform experiment for the above mentioned beam has been considered with the Rython material properties. The reason to do so, is the similarity of the mechanical parameter of the Rython composite to Aluminium with 9 GPa of Young's modulus and 1656 kg/m^3 of density. The important merits of using Rython composite in this experiment compared to aluminium are the simplicity of imposing pinned-pinned boundary condition, less damping of the material and its resonance frequency of the modes which are in appropriate range of the haptic application. Here the pinned-pinned boundary condition is directly realized thanks to elastic hinges as depicted on Fig. 4.3

The FEM model of the beam has been developed and a frequency analysis has been performed. The mode shapes of the structure have been obtained as depicted for some of them in Fig. 4.5. The frequency domain simulation (mode shape analysis) of the beam is limited only the first thirty one modes. This is due to the fact that, after thirty one modes the wavelength tend to the dimension of the hinges, thus the propagation is not concealed. In other word the boundary are not imposed.

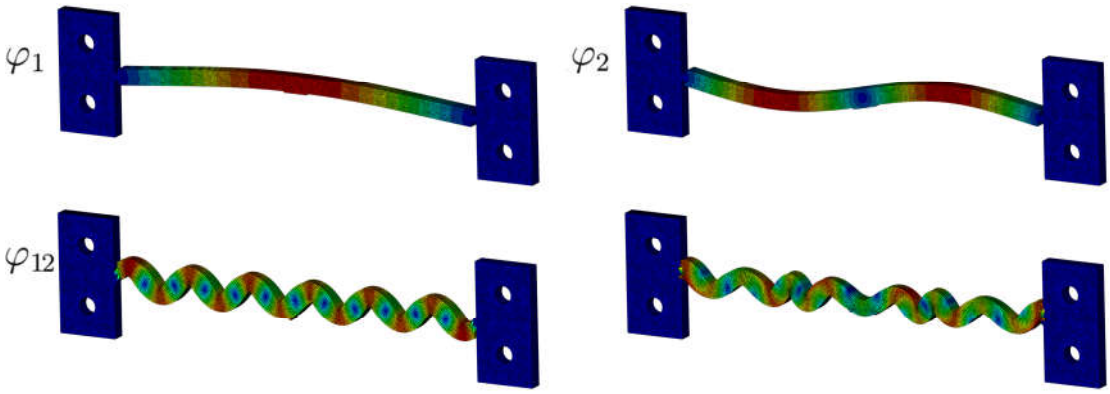

FIGURE 4.5: Mode shapes of Rython Beam obtained by FEM

The feasibility of exciting local deformation on the beam has been studied with FEM simulation as well, as presented in second chapter 2.1.1.

Once the feasibility of exciting sinc forms validated thanks to numerical simulations, the beam was manufactured with Rython composite material and pinned-pinned boundary condition with the dimension of 140 mm of length and 6 mm and 5 mm of width and thickness respectively. Only one actuator has been glued on the beam on one side of beam near one hinge(see Fig. 4.6). This location was chosen because it has almost no influence on the mode shapes, and it is able to excite all the flexure modes.

The identification test has been performed on the prototype and the modal parameters have been obtained as it is presented in Appendix A.

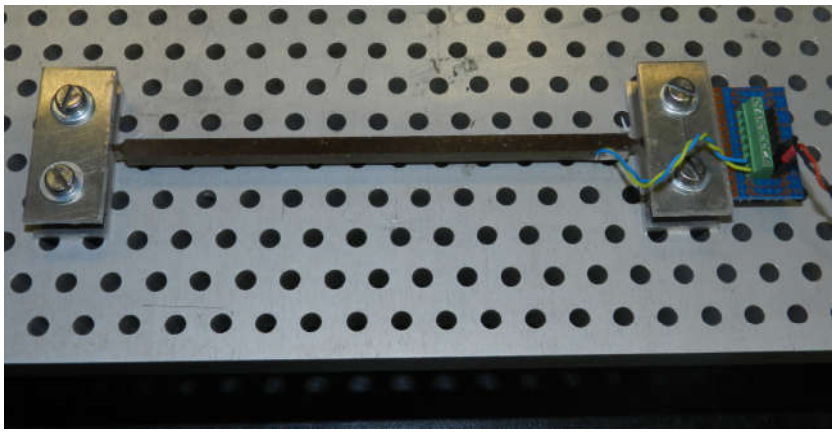

FIGURE 4.6: Prototype of beam manufactured by Rython composite with pinned-pinned bounary condition and a single actuator at a side (where the connections are visible)

4.2.3 Experimental results of local vibration excitation

A set of seven spatial sinc pulses have been defined as reference spatial form with pulse width of $PW = 20\ mm$ and various pulse center as presented in Table . 4.1:

Pulse n	P_1	P_2	P_3	P_4	P_5	P_6	P_7
Pulse center x_{Cspn}	$-58mm$	$-38mm$	$-19mm$	$0mm$	$+19mm$	$+38mm$	$+58mm$

TABLE 4.1: Pulse centers of defined spatial sinc for Rython beam experiment

The reference shapes are depicted in dark blue on Fig. 4.7. On the same figure, in light blue are the approximated shapes using 13 experimental modes, are represented. These shapes are actually obtained by superimposing the experimental modes of annex A. Using the modal coordinate resulting from the projection of the shape on the simulated modes. This confirms that the expected shape is feasible. The modal approximation

of these seven spatial pulse have been obtained using thirteen number of the modes of beam.

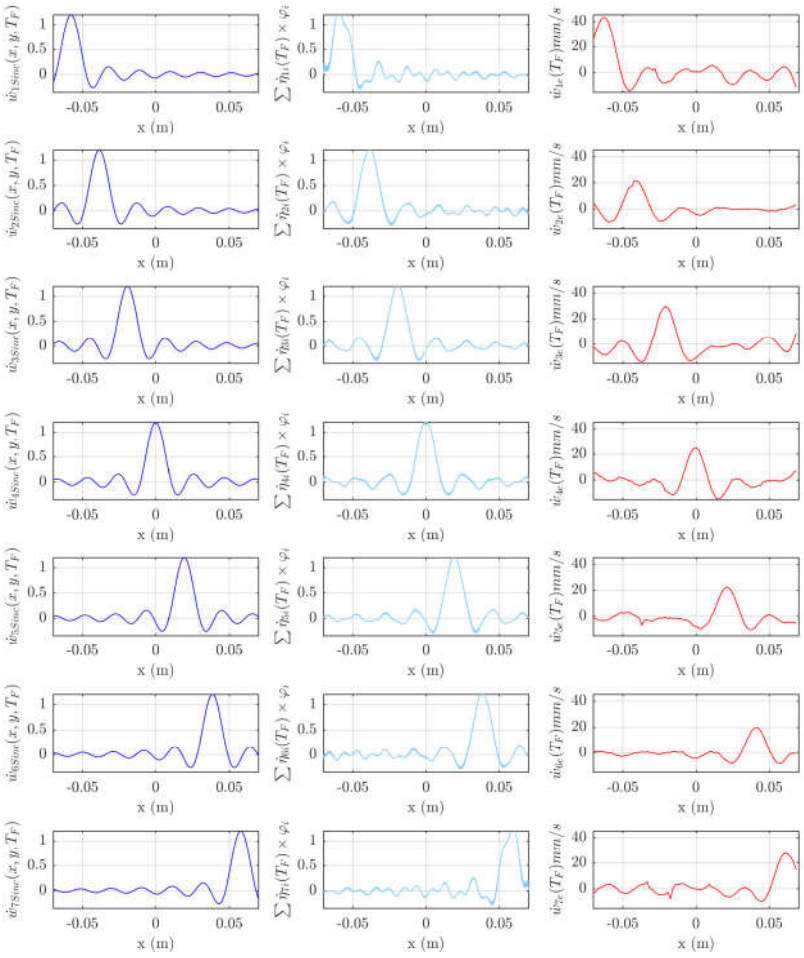

FIGURE 4.7: The reference spatial sinc pulses on Rython beam (dark blue), their modal modelled form using (light blue) number of the modes, experimentally measured vibration field of beam at $t = T_F$ (red)

The experimental measurement are obtained by recording the transient at regularly spaced location. A mean transient is then reconstituted, the synchronization signal is used here to garantee the correct superposition of the different runs. This procedure mitigates the measurement noise yieldding the curves in red in Fig. 4.7. The difficulty here is to compare spatial shapes that are potentially very different. In order to do so , we propose to use the following criterion:

$$\tau = \frac{cov(\dot{\boldsymbol{w}}_R, \dot{\boldsymbol{w}}_E(x, T_F))}{var(\dot{\boldsymbol{w}}_R)} \tag{4.2}$$

Where, cov is the covariance operator between $\dot{\boldsymbol{w}}_R$ and $\dot{\boldsymbol{w}}_E$ and var is the variance operator. This criterion can be easily implemented in the used for the case of sampled measurement. It also has a practical interpretation. Indeed, the covariance of two vectors is proportional to their scalar product. Hence, the more similarity exists between $\dot{\boldsymbol{w}}_R$ and $\dot{\boldsymbol{w}}_E$, the larger their covariance. To rescale the result, the covariance is divided by the variance of the reference form $\dot{\boldsymbol{w}}_R$. Therefore, ideally if $\dot{\boldsymbol{w}}_E = \dot{\boldsymbol{w}}_R$, since $cov(\dot{\boldsymbol{w}}_R, \dot{\boldsymbol{w}}_E) = var(\dot{\boldsymbol{w}}_R)$, τ will be equal to 1.

On Table. 4.2, the criterion is applied between reference (set to 40 mm/s) and measured velocity fields. On the first line of the table, the rough result are used while on the second, the measured vibration velocity fields are scaled to a unit maximum values. In the first case, the results are seemingly poor. This is due to the discrepancy of the actual amplitude, and the reference maximum amplitude of 40 mm/s. It appears once this factor eliminated by normalizing the maximum that the experimental shapes are close to what is expected.

Pulse center	P_1	P_2	P_3	P_4	P_5	P_6	P_7
τ	0.9268	0.5448	0.7963	0.6960	0.5962	0.4981	0.6444
τ_{Norm}	0.8625	1.0164	1.0791	1.1137	1.0629	0.9990	0.9398

TABLE 4.2: Covariance comparing factor of experimental and reference Sinc pulse of 20 mm on Rython beam

To conclude on this experiment, we can sum up the following results:

- The velocity fields can be realized using the proposed methodology
- A single actuator is capable to combine a large number of modes if it is correctly located with regard to the mode shapes.
- However, due to the technological limitation, in this case the limit voltage of the amplifier, the amplitude of experimental vibration velocity field cannot always be achieved.

Therefore, in the following further investigation are described based on a new set-up which involve several actuators.

4.3 Exciting various vibration field

This section is studying the possibility of not only focusing vibration but also exciting various spatial forms with more complicated spatial characteristics. These experiment objectives are defined in following subsection. The detail study of prototype and obtained experimental result will be studied afterward.

4.3.1 Design of the prototype

The previous prototype and its experimental results showed the possibility of exciting local vibration using modal synthesis.The aim of this section is to propose another beam whose boundary condition are easier to realize with a more realistic design for haptic display. To this aim, a clamped staple shape aluminium beam is proposed as depicted in Fig. 4.8. This new geometry is more appropriate for a haptic display, on the other hand, it does not completely fall into the frame of the beam theory. Hence, the application of the modal synthesising of vibration might be challenging for such structure.

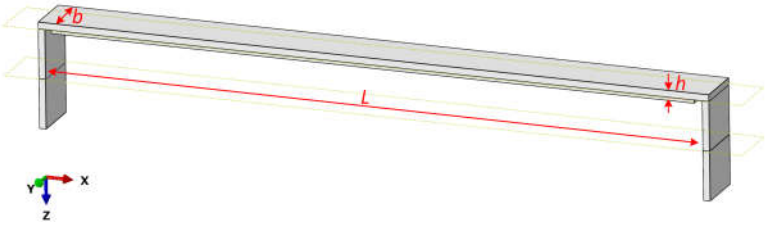

FIGURE 4.8: Schematic of clamped staple shape aluminium beam

The proposed schematic of staple shape beam in Fig. 4.8 is taken into account as the study case. The beam is considered to be made of aluminium and the bended edges of the beam are supposed to be clamped to a chassis. The FEM model of the beam has been developed and frequency domain simulation has been realize.d The obtained mode shape from FEM simulation is depicted in Fig. 4.9.

According to the result of FEM, the realized boundary condition concentrates the deformation roughly between the "legs" of the staple. While at high frequency, the boundary of the beam shows deflection of the modes in the sides which complicates the utilization of the theoretic beam model, see modes $\varphi_{12(x)}$-$\varphi_{14(x)}$. The problematic becomes more difficult knowing that the measurement of vibration field of staple beam is feasible on it upper face due to the technical limitation. As a result the identification of side deformation of mode shape is not possible and the spatial modelling of the structure does not include all the behavior of the structure.

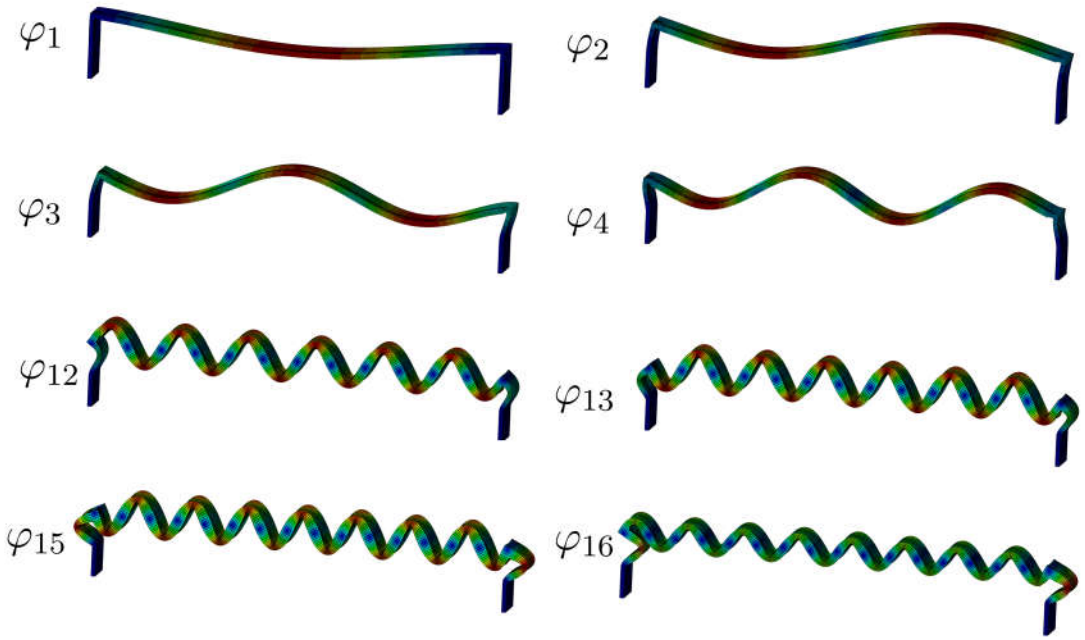

FIGURE 4.9: Number of mode shapes of prototype obtained by FEM simulation

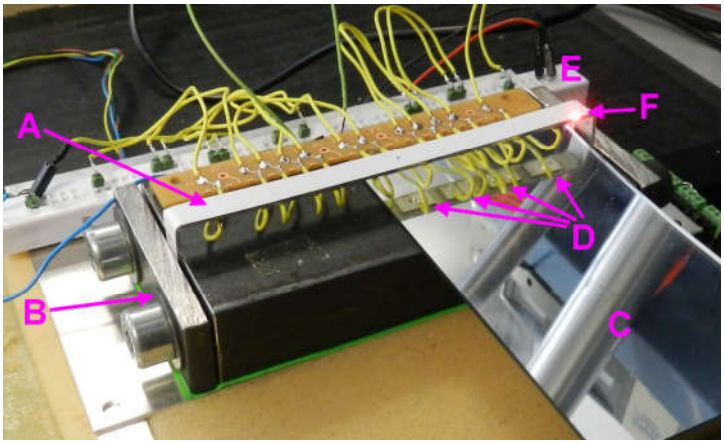

FIGURE 4.10: Prototype of beam manufactured by aluminium with clamped-clamped boundary condition

The beam is realized as shown in Fig. 4.10. In this figure, (A) is the beam, (B) is the chassis on which the beam is clamped, (D) are the actuators and (C) is a mirror by which we can observe the actuators, (E) is the electrical connections of actuator signals and (F) is the spot of laser. Eight piezoelectric actuators were glued under the beam. Each actuator has a different contribution in exciting the modes used in this experiment. An identification test has been realized on this beam for the frequency range of 100 Hz to 100 kHz(as mentioned in previous chapter). The result of identification is presented in Fig. 3.13 and Table 3.1.

4.3.2 Generalization to different velocity field

The objective of this section is to validate the possibility of exciting different spatial form. First a sinc pulse with different pulse width at different location of the beam. Secondly, the feasibility of exciting bump pulse is investigated. This shape has nice mathematical properties and zero velocity outside the given range. The square pulse is the ideal velocity field in the sense that velocity is constant within a range and zero outside. However it is difficult to excite since it requires an infinite number of the modes. The final part of this section discusses the possibility of exciting an approximation of square pulse.

4.3.2.1 Exciting Sinc pulses with different pulse width

The feasibility of the exciting spatial sinc pulse with pulse centre in arbitrary location have been proven in previous section. This section investigates the validity of modal projection and proposed model reduction in exciting spatial sinc pulses with different pulse width. To this end, three sets of experiments have been developed to excite firstly spatial pulse with pulse width of 25 mm and secondly to excite spatial pulses with even narrower pulse width of 18 mm and finally pulses with pulse width of 10 mm.

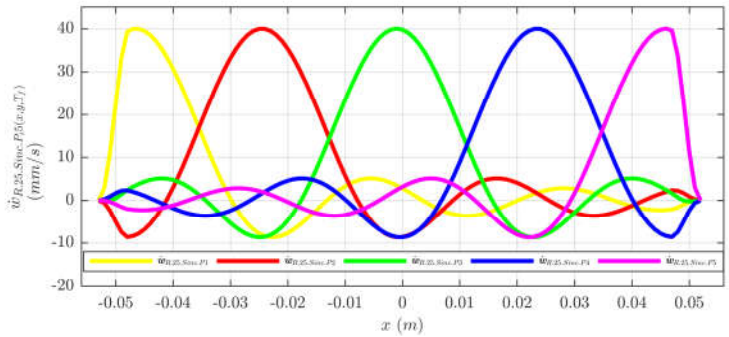

FIGURE 4.11: Reference spatial sinc pulse form with 25 mm of pulse width and amplitude of the 40 mm/s; Yellow line is $\dot{\boldsymbol{w}}_{R.25.Sinc.P1\,(x,T_F)}$, Red line is $\dot{\boldsymbol{w}}_{R.25.Sinc.P2\,(x,T_F)}$, Green line is $\dot{\boldsymbol{w}}_{R.25.Sinc.P3\,(x,T_F)}$, Blue line is $\dot{\boldsymbol{w}}_{R.25.Sinc.P4\,(x,T_F)}$ and Purple line is $\dot{\boldsymbol{w}}_{R.25.Sinc.P5\,(x,T_F)}$.

Five reference sinc pulse $\dot{\boldsymbol{w}}_{R.PW.Sinc.Pi\,(x,T_F)}$ with the same amplitude $A_{sp} = 40\ mm/s$ and same pulse width of $PW_{sp} = 25\ mm$ are defined with different pulse center x_{Csp}. The reference spatial pulses $\dot{\boldsymbol{w}}_{R.25.Sinc.P1\,(x,T_F)}$, $\dot{\boldsymbol{w}}_{R.25.Sinc.P2\,(x,T_F)}$, $\dot{\boldsymbol{w}}_{R.25.Sinc.P3\,(x,T_F)}$,

$\dot{\boldsymbol{w}}_{R.25.Sinc.P4\,(x,T_F)}$ and $\dot{\boldsymbol{w}}_{.}R.25.Sinc.P5\,(x,T_F)$ have their sinc pulse center at $x_{Csp.1} = -46\ mm$, $x_{Csp.2} = -24\ mm$, $x_{Csp.3} = 0\ mm$, $x_{Csp.4} = +24\ mm$ and $x_{Csp.5} = +46\ mm$ respectively as depicted in Fig. 4.11. As shown in this figure, the reference sinc pulses have been multiplied to a Tukey window whereby the window have the value of zero near boundary of the beam and unity value for the rest part of the beam. This is to respect kinematic compatible of vibration form with kinematic of geometry (Beam). As it is seen in Fig.4.11, the spatial shape of reference sinc function of sides $\dot{\boldsymbol{w}}_{R.25.Sinc.P1\,(x,T_F)}$ (yellow plot) and $\dot{\boldsymbol{w}}_{R.25.Sinc.P1\,(x,T_F)}$ (purple plot) have been influenced by Tukey window near the boundary of beam.

We keep the same sinc pulse parameter as previous case and we just change the pulse width to $PW_{sp} = 18\ mm$. Using this new value of pulse width five new reference spatial form are defined as ($\dot{\boldsymbol{w}}_{R.18.Sinc.P1\,(x,T_F)}$, $\dot{\boldsymbol{w}}_{R.18.Sinc.P2\,(x,T_F)}$, $\dot{\boldsymbol{w}}_{R.18.Sinc.P3\,(x,T_F)}$, $\dot{\boldsymbol{w}}_{R.18.Sinc.P4\,(x,T_F)}$ and $\dot{\boldsymbol{w}}_{R.18.Sinc.P5\,(x,T_F)}$ that have distinguish pulse center at $x_{Csp.1} = -46\ mm$, $x_{Csp.2} = -24\ mm$, $x_{Csp.3} = 0\ mm$, $x_{Csp.4} = +24\ mm$ respectively and are shown in Fig. 4.12.

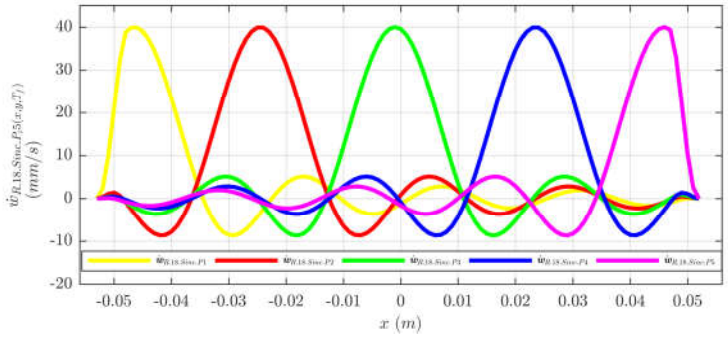

FIGURE 4.12: Reference spatial sinc pulse form with 18 mm of pulse width and amplitude of the 40 mm/s; Yellow line is $\dot{\boldsymbol{w}}_{R.18.Sinc.P1\,(x,T_F)}$, Red line is $\dot{\boldsymbol{w}}_{R.18.Sinc.P2\,(x,T_F)}$, Green line is $\dot{\boldsymbol{w}}_{R.18.Sinc.P3\,(x,T_F)}$, Blue line is $\dot{\boldsymbol{w}}_{R.18.Sinc.P4\,(x,T_F)}$ and Purple line is $\dot{\boldsymbol{w}}_{R.18.Sinc.P5\,(x,T_F)}$.

We define a set of even narrower pulses which have pulse width of $PW_{sp} = 10\ mm$ while their other pulse parameter are identic as previous sinc pulse. These new reference spatial forms are named $\dot{\boldsymbol{w}}_{R.10.Sinc.P1\,(x,T_F)}$, $\dot{\boldsymbol{w}}_{R.10.Sinc.P2\,(x,T_F)}$, $\dot{\boldsymbol{w}}_{R.10.Sinc.P3\,(x,T_F)}$, $\dot{\boldsymbol{w}}_{R.10.Sinc.P4\,(x,T_F)}$ and $\dot{\boldsymbol{w}}_{R.10.Sinc.P5\,(x,T_F)}$ and are depicted in Fig. 4.13.

4.3.2.2 Bump spatial pulse

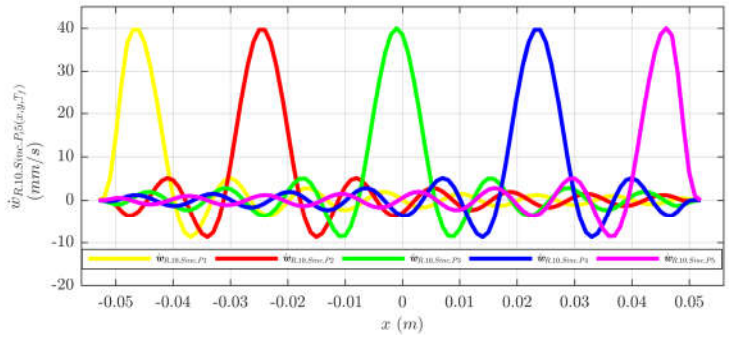

FIGURE 4.13: Reference spatial sinc deformation with 10 mm of pulse width and 40 mm/s amplitude; Yellow line is $\dot{\boldsymbol{w}}_{R.10.Sinc.P1\,(x,T_F)}$, Red is $\dot{\boldsymbol{w}}_{R.10.Sinc.P2\,(x,T_F)}$, Green is $\dot{\boldsymbol{w}}_{R.10.Sinc.P3\,(x,T_F)}$, Blue is $\dot{\boldsymbol{w}}_{R.10.Sinc.P4\,(x,T_F)}$ and Purple is $\dot{\boldsymbol{w}}_{R.10.Sinc.P5\,(x,T_F)}$.

For the purpose of exciting different spatial form, the Bump function has been chosen and defined as Eq. 4.3. The bump function is mathematically smooth function, which has derivatives of all order everywhere, and is a bounded function, whose amplitude value is inside bounded values. Hence it is a good candidate to reproduce it with vibration modes.

$$\dot{\boldsymbol{w}}_{R.PW.Bump\,(x,T_F)} = \begin{cases} \frac{A_{sp}}{e} e^{-\frac{1}{1-a(x-x_{Csp})^2}} & \text{if } |(x-x_{Csp}| < 1/a; \\ 0 & \text{otherwise.} \end{cases} \tag{4.3}$$

In this equation, A_{sp} and x_{Csp} are the bump pulse amplitude and bump pulse center, e is Euler's number and a is positive constant to determine bump pulse width.

Five desired spatial deformation of bump function have been defined in with five distinguish bump pulse center. Namely, $\dot{\boldsymbol{w}}_{R.25.Bump.P1\,(x,T_F)}$, $\dot{\boldsymbol{w}}_{R.25.Bump.P2\,(x,T_F)}$, $\dot{\boldsymbol{w}}_{R.25.Bump.P3\,(x,T_F)}$, $\dot{\boldsymbol{w}}_{R.25.Bump.P4\,(x,T_F)}$ and $\dot{\boldsymbol{w}}_{R.25.Bump.P5\,(x,T_F)}$ are defined with the same pulse amplitude of $A_{sp} = 40\ mm/s$ and same pulse width of $PW_{sp} = 25\ mm$ ($a = 53$) while with different pulse centers of respectively $x_{Csp.1} = -46\ mm$, $x_{Csp.2} = -24\ mm$, $x_{Csp.3} = 0\ mm$, $x_{Csp.4} = +24\ mm$ and $x_{Csp.5} = +46\ mm$. Morover, in order to respect kinetic compatibility of desired vibration form with boundary condition of beam, the same Tukey window as in previous case is multiplied to the defined reference bump pulse. Fig. 4.14 shows the reference spatial bump pulses in different colors, as mentioned earlier the tukey window has influenced bump pulses in boundary, $\dot{\boldsymbol{w}}_{R.25.Bump.P1\,(x,T_F)}$ and $\dot{\boldsymbol{w}}_{R.25.Bump.P5\,(x,T_F)}$, which are in yellow and purple colors.

4.3.2.3 Square spatial pulse

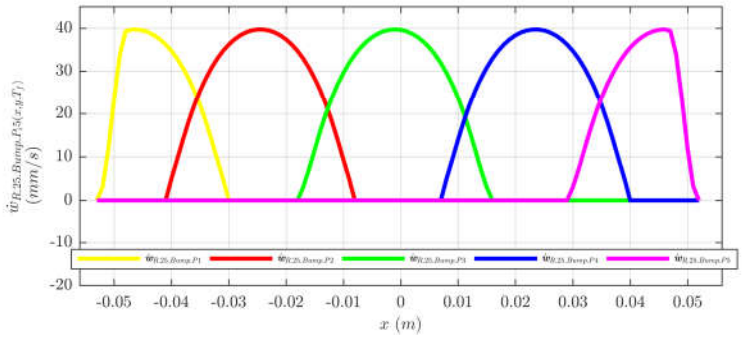

FIGURE 4.14: Reference spatial bump pulses with 25 mm of pulse width and 40 mm/s amplitude; Yellow line is $\dot{\boldsymbol{w}}_{R.25.Bump.P1\,(x,T_F)}$, Red is $\dot{\boldsymbol{w}}_{R.25.Bump.P2\,(x,T_F)}$, Green is $\dot{\boldsymbol{w}}_{R.25.Bump.P3\,(x,T_F)}$, Blue is $\dot{\boldsymbol{w}}_{R.25.Bump.P4\,(x,T_F)}$ and Purple is $\dot{\boldsymbol{w}}_{R.25.Bump.P5\,(x,T_F)}$.

A real challenge in exciting spatial form is exciting square pulse form on the beam. The difficulty is due to exciting sharp edges of the square form which theoretically requires excitation of all the modes of the beam. Thus, the Square spatial pulses were considered as new spatial form to be excited on the beam. The Square spatial pulse on the beam with pulse center of x_{Csp}, pulse width of PW_{sp} and pulse amplitude of A_{sp} are defined as following equation;

$$\dot{\boldsymbol{w}}_{R.PW.Squa\,(x,T_F)} = \begin{cases} A_{sp} & \text{if } |(x - x_{Csp}| < \frac{PW_{sp}}{2}; \\ 0 & \text{otherwise.} \end{cases} \tag{4.4}$$

As previous cases, five spatial square pulse are defined with the same amplitude of $A_{sp} = 40\ mm/s$, pulse width of $PW_{sp} = 25\ mm$ with five distinct pulse center at $x_{Csp.1} = -46\ mm$, $x_{Csp.2} = -24\ mm$, $x_{Csp.3} = 0\ mm$, $x_{Csp.4} = +24\ mm$ and $x_{Csp.5} = +46\ mm$. These defined spatial pulses $\dot{\boldsymbol{w}}_{R.25.Squa.P1\,(x,T_F)}$, $\dot{\boldsymbol{w}}_{R.25.Squa.P2\,(x,T_F)}$, $\dot{\boldsymbol{w}}_{R.25.Squa.P3\,(x,T_F)}$, $\dot{\boldsymbol{w}}_{R.25.Squa.P4\,(x,T_F)}$ and $\dot{\boldsymbol{w}}_{R.25.Squa.P5\,(x,T_F)}$ are multiplied to a tukey window to respect the kinetic of the boundary and they are depicted in Fig. 4.15. The tukey window has affected the pulse width of square pulse $\dot{\boldsymbol{w}}_{R.25.Squa.P1\,(x,T_F)}$ and $\dot{\boldsymbol{w}}_{R.25.Squa.P5\,(x,T_F)}$ which are located at the boundary of beam (see Fig. 4.15 Red and Purple lines).

4.3.3 Experimental results of control of Spatial Pulse Width

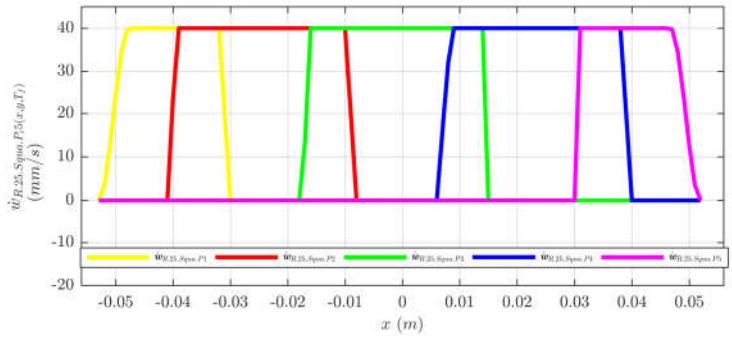

FIGURE 4.15: Reference spatial square pulses with 25 mm of pulse width and 40 mm/s amplitude; Yellow line is $\dot{\boldsymbol{w}}_{R.25.Squa.P1\,(x,T_F)}$, Red is $\dot{\boldsymbol{w}}_{R.25.Squa.P2\,(x,T_F)}$, Green is $\dot{\boldsymbol{w}}_{R.25.Squa.P3\,(x,T_F)}$, Blue is $\dot{\boldsymbol{w}}_{R.25.Squa.P4\,(x,T_F)}$ and Purple is $\dot{\boldsymbol{w}}_{R.25.Squa.P5\,(x,T_F)}$.

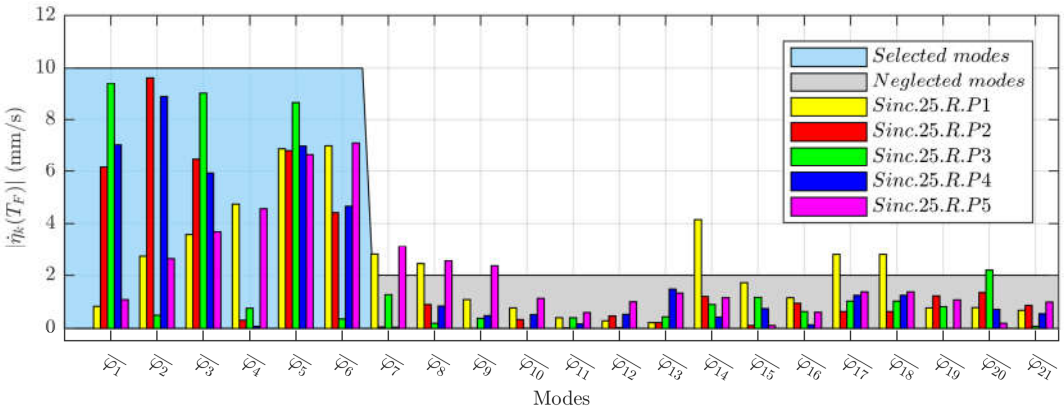

FIGURE 4.16: Absolute value of Modal Coefficients of Sinc spatial pulse with 25 mm pulse width; Yellow, Red, Green, Blue and purple respectively represents the modal coefficients for pulses with pulse center in P1, P2, P3, P4 and P5, The light blue region shows the modelled modes for experimental excitation and the gray region shows the neglected modes in the experiment.

4.3.3.1 Sinc Pulse with 25 mm Pulse Width

All five reference spatial form, shown in Fig. 4.11 were decomposed to their modal coefficient using twenty one identified modes and Eq. 2.22 and their modal value have been achieved as $\dot{\eta}^*_{k.R.25.Sinc.P1}$, $\dot{\eta}^*_{k.R.25.Sinc.P2}$, $\dot{\eta}^*_{k.R.25.Sinc.P3}$, $\dot{\eta}^*_{k.R.25.Sinc.P4}$ and $\dot{\eta}^*_{k.R.25.Sinc.P5}$, whose absolute value is depicted respectively with yellow, red, green, dark blue and purple bars for twenty-first modes of beam in Fig. 4.16. In these notation $\dot{\eta}^*_{k.R.25.Sinc.P_i}$ shows k^{th} modal coefficient of Sinc spatial form with pulse width of 25 mm and pulse center of P_i. Theoretically, for obtaining desired reference all modes should be excited to their modal coefficient values, while practically it is not feasible, hence a mode selection and model reduction method should be taken into account. During all experiment, we

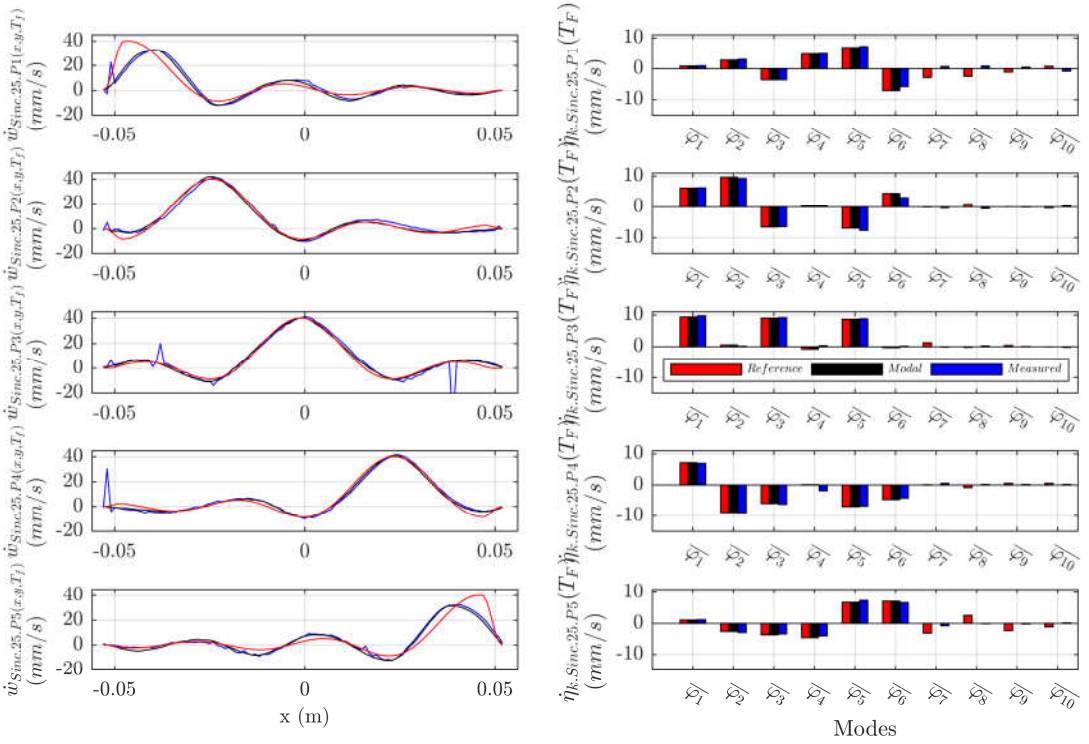

FIGURE 4.17: **Left:** The Reference (red color) $\dot{\boldsymbol{w}}_{R.25.Sinc.P_i\,(x,T_F)}$, Modal modelled (black color) $\dot{\boldsymbol{w}}_{M.25.Sinc.P_i\,(x,T_F)}$ and experimentally measured (blue color) $\dot{\boldsymbol{w}}_{E.25.Sinc.P_i\,(x,T_F)}$ spatial sinc in different location on the beam (from top to below: $P1$, $P2$, ... and $P5$). **Right:** The modal coefficient of Reference spatial form $\dot{\eta}^*_{k.R.25.Sinc.P1}$ (red bars), modal coefficient of modal modelled spatial sinc $\dot{\eta}^*_{k.M.25.Sinc.P1}$ (black bars) and modal coefficient of experimentally excited spatial form $\dot{\eta}^*_{k.E.25.Sinc.P1}$ (blue bars).

proposed to select the modes whose modal coefficient value for most of five pulse has more that 20% of maximal mode coefficients.

For this case, the maximum modal value is for $\dot{\eta}^*_{2.R.25.Sinc.P2} \simeq 10\ mm/s$ (Red bar on mode $\overline{\varphi}_{k(x)}$ in Fig. 4.16), hence we consider 2 mm/s line as minimum line. The modes that has more than 2 mm/s for majority of five modal coefficients are selected and the rest of modes are neglected. As it is seen in Fig. 4.16 the modes $\overline{\varphi}_{1(x)}$), $\overline{\varphi}_{2(x)}$), $\overline{\varphi}_{3(x)}$), $\overline{\varphi}_{4(x)}$), $\overline{\varphi}_{5(x)}$), and $\overline{\varphi}_{6(x)}$) are selected modes for this experiment (light blue region) the rest of modes are neglected (light gray region). As a consequence, only modes $\overline{\varphi}_{1(x)}$- $\overline{\varphi}_{6(x)}$ will be excited to generate spatial sinc defined in this subsection. The reference spatial sinc are shown in red color in Fig. 4.17 and modal approximating of each spatial sinc has been achieved using the six modelled modes in the same figure in black color. According to the figure (left side), The modal modelled spatial sinc are an approximation for $\dot{\boldsymbol{w}}_{M.25.Sinc.P2\,(x,T_F)}$, $\dot{\boldsymbol{w}}_{M.25.Sinc.P3\,(x,T_F)}$ and $\dot{\boldsymbol{w}}_{M.25.Sinc.P4\,(x,T_F)}$. While for the modal modelled sinc for two side of beam, namely $\dot{\boldsymbol{w}}_{M.25.Sinc.P1\,(x,T_F)}$ and $\dot{\boldsymbol{w}}_{M.25.Sinc.P5\,(x,T_F)}$ have noticible difference from their reference values $\dot{\boldsymbol{w}}_{R.25.Sinc.P1\,(x,T_F)}$

and $\dot{\boldsymbol{w}}_{R.25.Sinc.P5\,(x,T_F)}$. This is due to the fact that for exciting spatial sinc near boundary of the beam more than six modes are required (see $\dot{\eta}^*_{k.R.25.Sinc.P1}$ and $\dot{\eta}^*_{k.R.25.Sinc.P5}$ red bars for modes $\overline{\varphi}_{7(x)}$), $\overline{\varphi}_{8(x)}$ and $\overline{\varphi}_{14(x)}$ in Fig.4.16.

By substituting the determined modal coefficient $\dot{\eta}^*_{k.R.25.Sinc.Pi}$ and identified dynamic parameter (f_k and ζ_k) into Eq. 2.34 for six premier modes($\overline{\varphi}_{1(x)}$- $\overline{\varphi}_{6(x)}$) the excitation voltage for actuators $v_{R.1(t)}$ and $v_{R.2(t)}$ have been defined and applied to the actuator as explained before. The experimentally measured vibration velocity field at $t = T_f$ for each pulse center case are shown in blue color in Fig. 4.17 left. In this figure the experimentally achieved result for spatial sinc $\dot{\boldsymbol{w}}_{E.25.Sinc.Pi\,(x,T_F)}$ is almost the same as expected modal modelled spatial values of $\dot{\boldsymbol{w}}_{M.25.Sinc.P2\,(x,T_F)}$. Looking at modal coefficients of experimentally excited spatial sinc $\dot{\eta}^*_{k.E.25.Sinc.Pi}$, it is obvious that the experimental achieved result have almost the same of the references with slight error for some modes. For the side focuses, $\dot{\boldsymbol{w}}_{E.25.Sinc.P1\,(x,T_F)}$ and $\dot{\boldsymbol{w}}_{M.25.Sinc.P5\,(x,T_F)}$ are well following modelled values of $\dot{\boldsymbol{w}}_{M.25.Sinc.P2\,(x,T_F)}$ and $\dot{\boldsymbol{w}}_{M.25.Sinc.P5\,(x,T_F)}$ and their slight spatial error from $\dot{\boldsymbol{w}}_{R.25.Sinc.P1\,(x,T_F)}$ and $\dot{\boldsymbol{w}}_{R.25.Sinc.P5\,(x,T_F)}$ is due to model reduction as mentioned earlier. Briefly, by using modal model of beam and it is possible to excite sinc deformation with pulse center x_{Csp} in different location on beam at pulse width of $PW_{Csp} = 25\ mm$. Additionally, not all the modes of the structure are necessary to excite desired spatial form, by applying modal reduction method it is possible to excited limited number of modes and generated an acceptable approximation of the spatial form. As in this experiment by exciting only six modes, the sinc spatial form with 25 mm of pulse width are excitable.

Pulse center	P_1	P_2	P_3	P_4	P_5
Covariance factor	0.8323	0.9881	1.0085	0.9933	0.8545

TABLE 4.3: Covariance comparing factor of experimental and reference Sinc pulse of 25 mm

4.3.3.2 Sinc Pulse with 18 *mm* Pulse Width

The reference spatial form of sinc pulses with 18 mm of pulse widths as illustrated in Fig. 4.12. For the purpose of defining reduced modal model of these new spatial pulses, the $\dot{\boldsymbol{w}}_{R.18.Sinc.P1\,(x,T_F)}$, $\dot{\boldsymbol{w}}_{R.18.Sinc.P2\,(x,T_F)}$, $\dot{\boldsymbol{w}}_{R.18.Sinc.P3\,(x,T_F)}$, $\dot{\boldsymbol{w}}_{R.18.Sinc.P4\,(x,T_F)}$ and $\dot{\boldsymbol{w}}_{.}R.18.Sinc.P5\,(x,T_F)$ (whose absolute values are depicted in Fig. 4.18 respectively in Yellow, Red, Green, Blue and Purple color) are decomposed to the experimentally

identified and normalized modes of beam ($\overline{\varphi}_{k(x)}$) using Eq. 2.22 and modal coefficient of each spatial form have been obtained.

The same model reduction criteria as in the previous case has been applied. Meaning that, the maximum absolute value of modal coefficient among all modal coefficients $Max(|\dot{\eta}_{k.R.18.Sinc.P_i\,(T_F)}|)$ is chosen as the maximal value. For this case, $|\dot{\eta}_{7.R.18.Sinc.P3\,(T_F)}|$ the 7^{th} mode coefficient of the center pulse is found to have maximal value of almost 7 mms/s. The twenty percent of this maximal value is defined as 1.4 mm/s, the modes $\overline{\varphi}_{k(x)}$ whose contribution for five define spatial pulse is less than the limit value are neglected from modes (the modes highlighted with gray region in Fig. 4.18) the rest of the modes are kept in model to experimentally excite the 18 mm width sinc pulses (the modes appearing in the light green region in Fig. 4.18). As in this Figure the nine modes of $\overline{\varphi}_{1(x)}$ to $\overline{\varphi}_{9(x)}$ are required to excite these new spatial references.

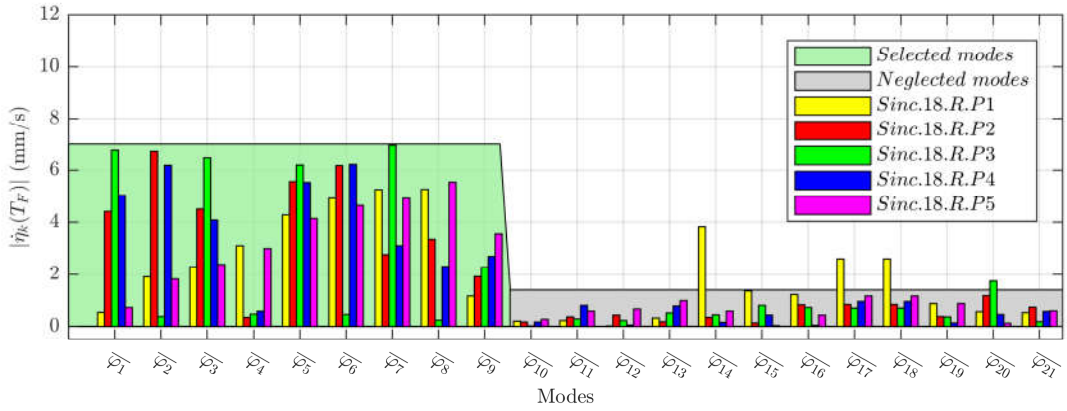

FIGURE 4.18: Absolute value of Modal Coefficients of Sinc spatial pulse with 18 mm pulse width; Yellow, Red, Green, Blue and purple respectively represents the modal coefficients for pulses with pulse center in P1, P2, P3, P4 and P5, The light green region shows the modelled modes for experimental excitation and the gray region shows the neglected modes in the experiment.

In order to confirm the spatial precision of modelled spatial sinc pulses with determined modal band ($\overline{\varphi}_{1(x)}$ to $\overline{\varphi}_{9(x)}$), five spatial pulse have been reproduced using nine mode and nine modal coefficient as $\dot{\boldsymbol{w}}_{M.18.Sinc.P_i\,(x,T_F)} = \sum_{k=1}^{9} \dot{\eta}_{k.R.18.Sinc.P_i\,(T_F)} \overline{\varphi}_{k(x)}$. These reproduced modal modelled spatial sinc pulses $\dot{\boldsymbol{w}}_{M.18.Sinc.P_i\,(x,T_F)}$ is illustrated in Fig.4.19.left with black color. The defined reference spatial forms are shown in the same figures with red color for five distinct pulse center. Regarding to these figures, the model reduction is capable to reproduce a good approximation of the reference sinc forms, except for sinc near the boundary of the beam ($\dot{\boldsymbol{w}}_{R.18.Sinc.P1\,(x,T_F)}$ and $\dot{\boldsymbol{w}}_{R.18.Sinc.P5\,(x,T_F)}$). More than nine modes are required to excite these two spatial form. This can be seen in Fig. 4.18

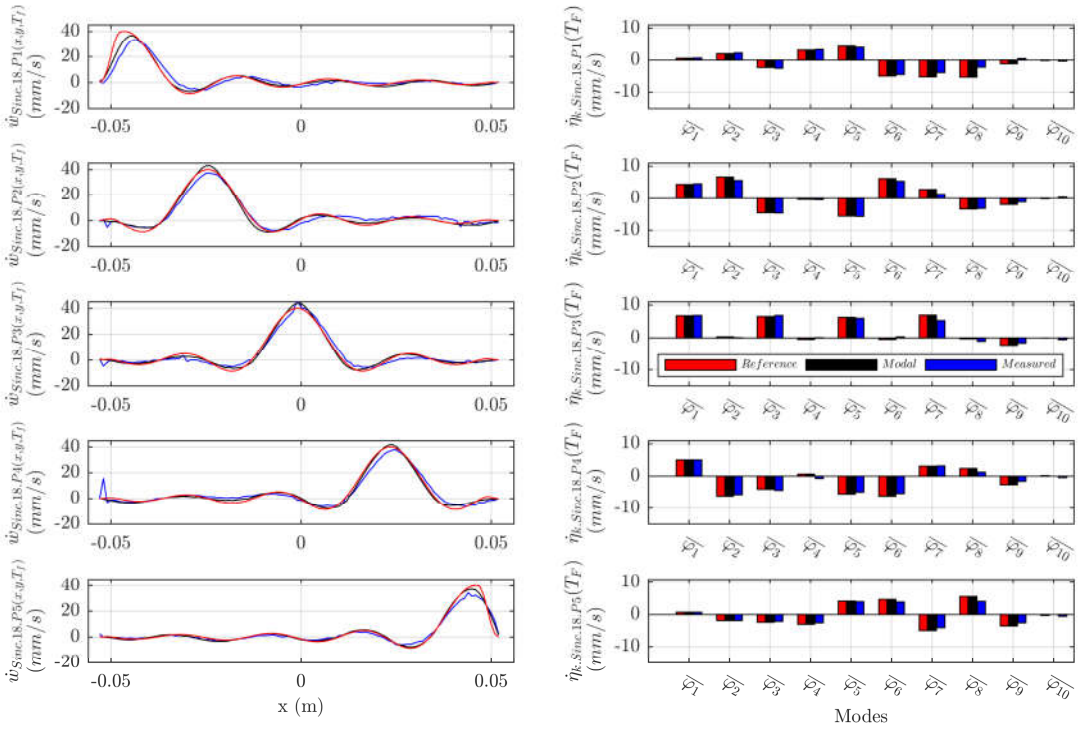

FIGURE 4.19: **Left:** The Reference (red color) $\dot{\boldsymbol{w}}_{R.18.Sinc.P_i\,(x,T_F)}$, Modal modelled (black color) $\dot{\boldsymbol{w}}_{M.18.Sinc.P_i\,(x,T_F)}$ and experimentally measured (blue color) $\dot{\boldsymbol{w}}_{E.18.Sinc.P_i\,(x,T_F)}$ spatial sinc in different location on the beam (from top to below: $P1$, $P2$, ... and $P5$). **Right:** The modal coefficient of Reference spatial form $\dot{\eta}^*_{k.R.18.Sinc.P1}$ (red bars), modal coefficient of modal modelled spatial sinc $\dot{\eta}^*_{k.M.18.Sinc.P1}$ (black bars) and modal coefficient of experimentally excited spatial form $\dot{\eta}^*_{k.E.18.Sinc.P1}$ (blue bars).

with yellow bars and their corresponding modes $\overline{\varphi}_{17(x)}$, $\overline{\varphi}_{1(x)}$ and $\overline{\varphi}_{18(x)}$ which are inside neglected modes.

The excitation voltages of the actuator have been created utilizing the aforementioned Eq. 2.34, the created signals are applied to the actuators and the vibration field of the beam have been measured as the processes explained at the beginning of this section. The experimentally measured spatial vibration form at the end transient moment $T_F = 25\ ms$ for five different measurement ($\dot{\boldsymbol{w}}_{M.18.Sinc.P_1\,(x,T_F)}$, $\dot{\boldsymbol{w}}_{M.18.Sinc.P_2\,(x,T_F)}$, $\dot{\boldsymbol{w}}_{M.18.Sinc.P_3\,(x,T_F)}$, $\dot{\boldsymbol{w}}_{M.18.Sinc.P_4\,(x,T_F)}$, and $\dot{\boldsymbol{w}}_{M.18.Sinc.P_5\,(x,T_F)}$) are depicted in blue color in Fig. 4.19. left. Looking at the spatial form of measured spatial form (blue lines in Fig.4.19.left) and comparing to its expected modal form (black lines in Fig.4.19.left), the feasibility of addressing sinc pulse with pulse width of 18 mm in five different pulse center are validated. Meanwhile, Fig.4.19.right shows the modal coefficients of experimentally excited spatial form $\dot{\eta}^*_{k.E.18.Sinc.P_i}$ with blue bars and expected modal coefficient $\dot{\eta}^*_{k.M.18.Sinc.P_i}$ in black color. Comparing these two values of modal coefficients shows

that at focusing moment T_F, the modes of beam are well excited to reach their reference value (black bars). This confirms when using the criteria 4.2, as shown in Table. 4.4

Pulse center	P_1	P_2	P_3	P_4	P_5
Covariance factor	0.8228	0.9531	1.0068	0.9535	0.9165

TABLE 4.4: Covariance comparing factor of experimental and reference Sinc pulse of 18 mm

4.3.3.3 Sinc Pulse with 10 *mm* Pulse Width

These reference spatial deformation, shown in Fig. 4.21, are decomposed to their modal values as explained in previous subsubsection 4 and the absolute value of modal coefficients for all five reference form ($\dot{\eta}^*_{k.R.10.Sinc.P1}$, $\dot{\eta}^*_{k.R.10.Sinc.P2}$, $\dot{\eta}^*_{k.R.10.Sinc.P3}$, $\dot{\eta}^*_{k.R.10.Sinc.P4}$ and $\dot{\eta}^*_{k.R.10.Sinc.P5}$) have been achieved and illustrated in Fig. 4.20. The same model reduction approach has been applied to this case whereby first sixteen modes of the beam have been selected to excite Sinc pulse with 10 *mm* of pulse width.

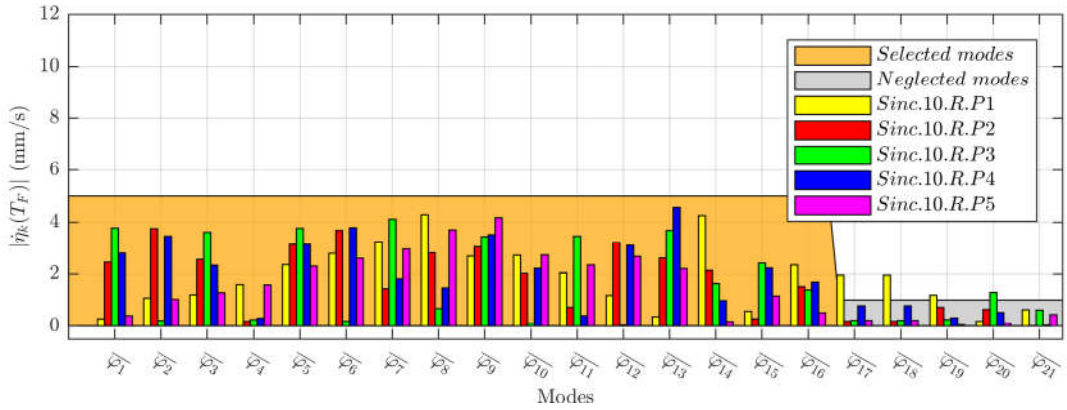

FIGURE 4.20: Absolute value of Modal Coefficients of Sinc spatial pulse with 10 *mm* pulse width; Yellow, Red, Green, Blue and purple respectively represents the modal coefficients for pulses with pulse center in P1, P2, P3, P4 and P5, The light orange region shows the modelled modes for experimental excitation and the gray region shows the neglected modes in the experiment.

The five reference deformation are reconstructed with modelled modes and the modal modelled spatial deformation of 10 *mm* pulse width sinc function $\dot{\boldsymbol{w}}_{M.10.Sinc.P1\,(x,T_F)}$, $\dot{\boldsymbol{w}}_{M.10.Sinc.P2\,(x,T_F)}$, $\dot{\boldsymbol{w}}_{M.10.Sinc.P3\,(x,T_F)}$, $\dot{\boldsymbol{w}}_{M.10.Sinc.P4\,(x,T_F)}$ and $\dot{\boldsymbol{w}}_{M.10.Sinc.P5\,(x,T_F)}$ are plotted in black color in Fig. 4.21.left a side their analytically defined reference value (red color Fig.4.21. left). According to this figure, It is clear that the modal modeled spatial $\dot{\boldsymbol{w}}_{M.10.Sinc.P_i\,(x,T_F)}$ have almost the same form as reference spatial sinc $\dot{\boldsymbol{w}}_{R.10.Sinc.P_i\,(x,T_F)}$. This is the case even for sinc whose pulse center is in boundary. Hence, the validity of the

model reduction is confirmed. The experimentally measured values of spatial deformation at the end of the transient moment of $t = T_F$ ($\dot{\boldsymbol{w}}_{E.10.Sinc.P1\,(x,T_F)}$, $\dot{\boldsymbol{w}}_{E.10.Sinc.P2\,(x,T_F)}$, $\dot{\boldsymbol{w}}_{E.10.Sinc.P3\,(x,T_F)}$, $\dot{\boldsymbol{w}}_{E.10.Sinc.P4\,(x,T_F)}$ and $\dot{\boldsymbol{w}}_{E.10.Sinc.P5\,(x,T_F)}$) are depicted in blue lines in Fig. 4.21.left. The achieved experiment spatial form are in good agreement in term of pulse width, pulse center and pulse amplitude to their expected modal modelled values. As a conclusion, the method of modal projection and modal reduction is valid to excite sinc deformation with 10 mm pulse width as well.

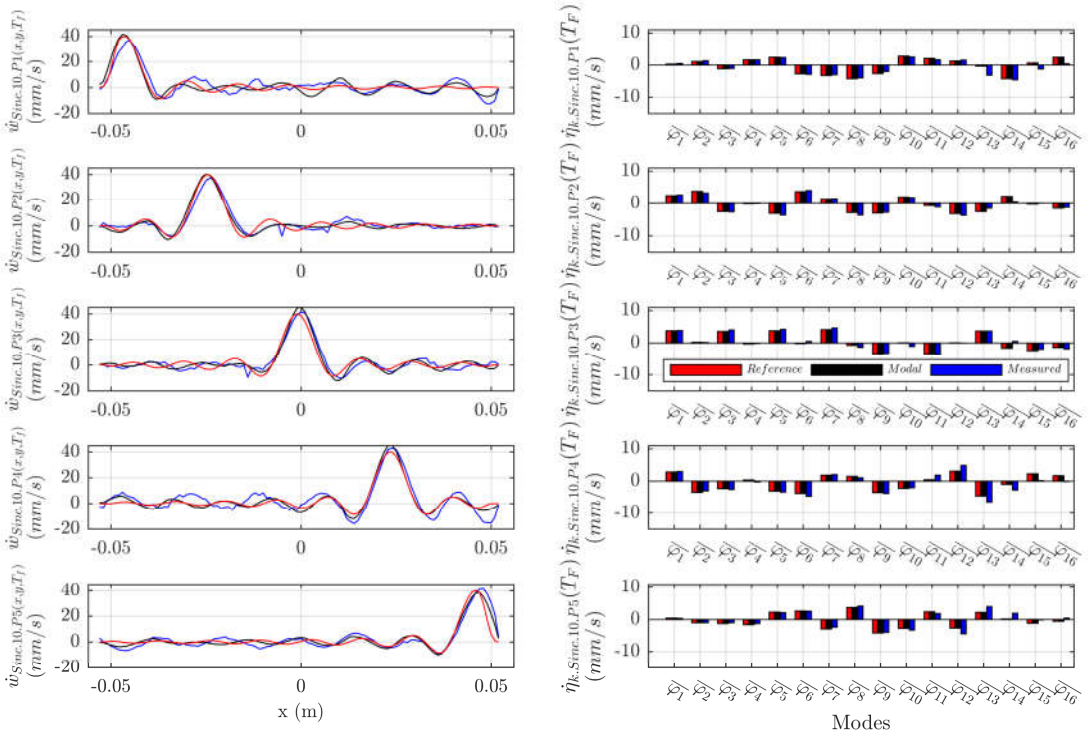

FIGURE 4.21: **Left:** The Reference (red color) $\dot{\boldsymbol{w}}_{R.10.Sinc.P_i\,(x,T_F)}$, Modal modelled (black color) $\dot{\boldsymbol{w}}_{M.10.Sinc.P_i\,(x,T_F)}$ and experimentally measured (blue color) $\dot{\boldsymbol{w}}_{E.10.Sinc.P_i\,(x,T_F)}$ spatial sinc in different location on the beam (from top to below: $P1$, $P2$, ... and $P5$). **Right:** The modal coefficient of Reference spatial form $\dot{\eta}^*_{k.R.10.Sinc.P1}$ (red bars), modal coefficient of modal modelled spatial sinc $\dot{\eta}^*_{k.M.10.Sinc.P1}$ (black bars) and modal coefficient of experimentally excited spatial form $\dot{\eta}^*_{k.E.10.Sinc.P1}$ (blue bars).

Fig. 4.21.right shows the modal coefficient of desired spatial form $\dot{\eta}^*_{k.R.10.Sinc.P_i}$ with red bars, model modelled coefficients $\dot{\eta}_{k.M.10.Sinc.P_i}$ with black bars and experimentally obtained modal coefficients $\dot{\eta}_{k.R.10.Sinc.P_i\,(T_F)}$ at $t = T_F$ for each deformation. The experimentally obtained modal values (blue bars) are in agreement with the expected values (black bars). Except for the points P_4 and P_5 which have errors of amplitude in comparison with their reference values. The application of the criterion reveals more clearly the discrepancies.

Pulse center	P_1	P_2	P_3	P_4	P_5
Covariance factor	0.8196	0.9091	0.9317	1.0770	0.8993

TABLE 4.5: Covariance comparing factor of experimental and reference Sinc pulse of 10 mm

4.3.4 Bump Spatial Pulse Shape

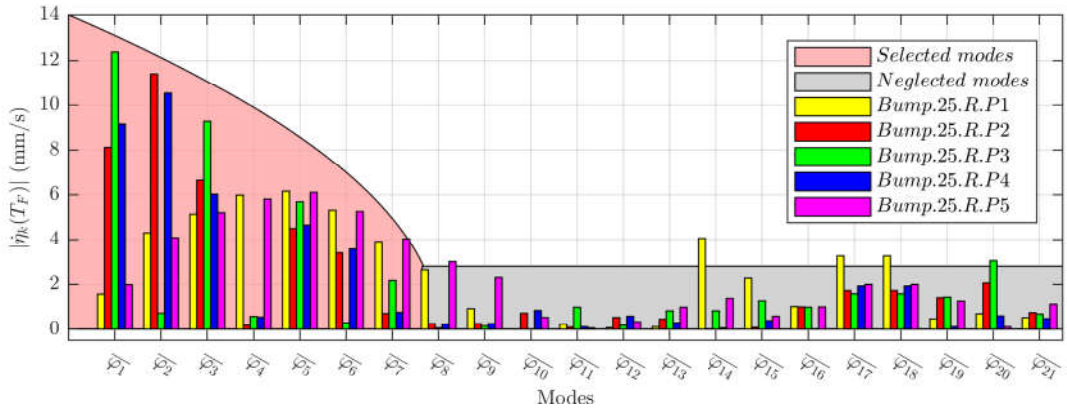

FIGURE 4.22: Absolute value of Modal Coefficients of Bump spatial pulse with 25 mm pulse width; Yellow, Red, Green, Blue and purple respectively represents the modal coefficients for pulses with pulse center in P1, P2, P3, P4 and P5, The light orange region shows the modelled modes for experimental excitation and the gray region shows the neglected modes in the experiment.

To build reduced modal model, all five bump pulses, depicted in Fig. 4.14, are decomposed on the modal bars illustrated in Fig. 4.22. The maximum modal coefficient of 12 mm/s (approximately) have been recognized to the $\dot{\eta}^*_{1.E.25.Bump.P3}$ and the 20% margin of 2.4 mm/s have been defined. Only the modes whose modal coefficient value for majority of five reference are more than this minimum limit are kept in the model and the rest are neglected. For exciting the spatial bump with given pulse width, the seven first modes of the beam are required ($\overline{\varphi}_{1(x)}$ to $\overline{\varphi}_{7(x)}$) as shown in light red region in Fig. 4.22. The rest of the modes ($\overline{\varphi}_{8(x)}$to $\overline{\varphi}_{21(x)}$) are neglected.

Using the modelled modes of ($\overline{\varphi}_{1(x)}$ to $\overline{\varphi}_{7(x)}$), the modal modelled spatial form of bump function have been recreated for to purpose of investigating spatial accuracy of modal. The modal modelled bump pulses $\dot{\boldsymbol{w}}_{M.25.Bump.P1\,(x,T_F)}$, $\dot{\boldsymbol{w}}_{M.25.Bump.P2\,(x,T_F)}$, $\dot{\boldsymbol{w}}_{M.25.Bump.P3\,(x,T_F)}$, $\dot{\boldsymbol{w}}_{M.25.Bump.P4\,(x,T_F)}$ and $\dot{\boldsymbol{w}}_{M.25.Bump.P5\,(x,T_F)}$ are illustrated in Fig. 4.23. left in black color. The reference defined bump pulse are depicted in the same figure in red color, the modal model spatial bumps (black color) have almost the same form of reference bump for $P2$, $P3$ and $P4$. Except, the modal modelled spatial bump in $P1$ and $P5$ have slight difference than their reference value. This is due to the model reduction and neglecting the contributing modes for regenerating boundary side pulse.

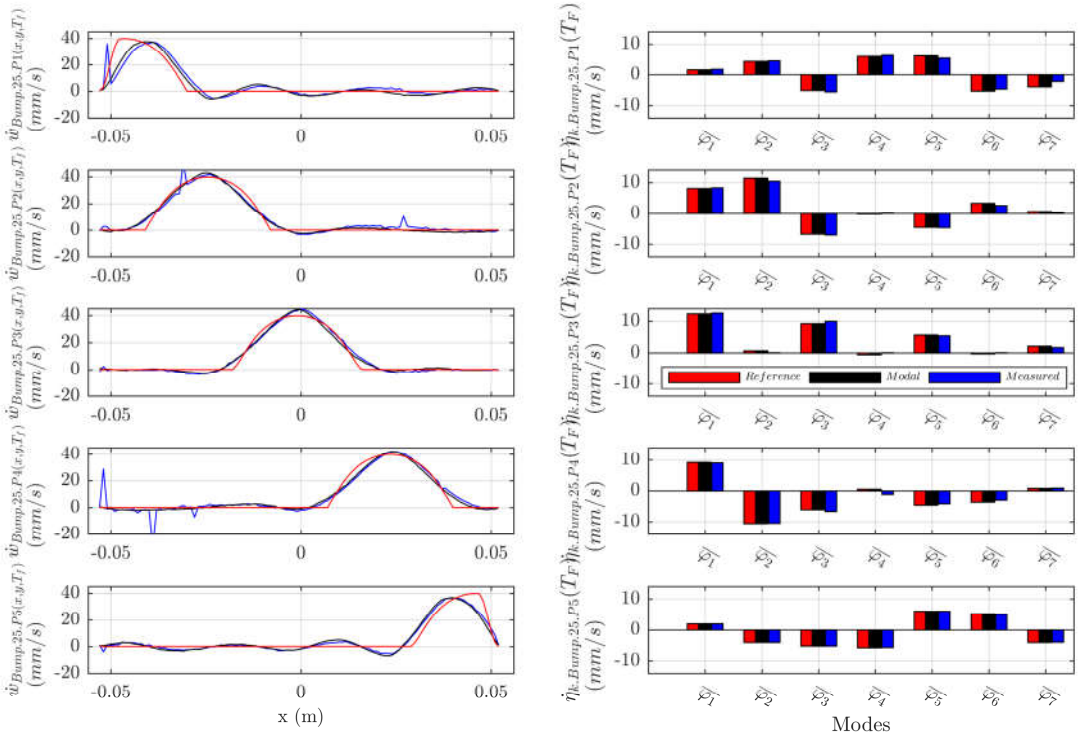

FIGURE 4.23: **Left:** The Reference (red color) $\dot{\boldsymbol{w}}_{R.25.Bump.P_i\,(x,T_F)}$, Modal modelled (black color) $\dot{\boldsymbol{w}}_{M.25.Bump.P_i\,(x,T_F)}$ and experimentally measured (blue color) $\dot{\boldsymbol{w}}_{E.25.Bump.P_i\,(x,T_F)}$ spatial sinc in different location on the beam (from top to below: $P1$, $P2$, ... and $P5$). **Right:** The modal coefficient of Reference spatial form $\dot{\eta}^*_{k.R.25.Bump.P1}$ (red bars), modal coefficient of modal modelled spatial sinc $\dot{\eta}^*_{k.M.25.Bump.P1}$ (black bars) and modal coefficient of experimentally excited spatial form $\dot{\eta}^*_{k.E.25.Bump.P1}$ (blue bars).

Briefly, the reduced modal model is sufficient to regenerate a good approximation of bump form.

The beam have been excited by calculating excitation signals of actuator Eq. 2.34 and the spatial deformation of beam have been obtained for the beam at the end transient $t = T_F$. The obtained experimental result of spatial deformation of beam $\dot{\boldsymbol{w}}_{E.25.Bump.P1\,(x,T_F)}$, $\dot{\boldsymbol{w}}_{E.25.Bump.P2\,(x,T_F)}$, $\dot{\boldsymbol{w}}_{E.25.Bump.P3\,(x,T_F)}$, $\dot{\boldsymbol{w}}_{E.25.Bump.P4\,(x,T_F)}$ and $\dot{\boldsymbol{w}}_{E.25.Bump.P5\,(x,T_F)}$ are depicted with blue line respectively from top to below of Fig. 4.23. left. The experimentally measured spatial form matches the expected modal spatial form (black line), which confirms the feasibility of exciting bump spatial form. The modal value of experimentally obtained spatial field (blue bars in Fig. 4.23. right) shows that the modelled modes are practically excited for the same amplitude of expected value (black bars in Fig. 4.23. right) with a negligible error, as seen in table 4.6.

Pulse center	P_1	P_2	P_3	P_4	P_5
Covariance factor	0.8371	0.9325	1.0057	0.9487	0.9041

TABLE 4.6: Covariance comparing factor of experimental and reference Bump pulse of 25 mm

4.3.5 Square Spatial Pulse Shape

The reference Square pulses, illustrated in Fig.4.15 are decomposed to their modal values of $\dot{\eta}_{k.R.25.Squa.P1}$, $\dot{\eta}_{k.R.25.Squa.P2}$, $\dot{\eta}_{k.R.25.Squa.P3}$, $\dot{\eta}_{k.R.25.Squa.P4}$ and $\dot{\eta}_{k.R.25.Squa.P5}$ using Eq.2.22 and their absolute values are shown in Fig. 4.24. Theoretically, to excite a square pulse infinite number of modes is required. While, we are interested to simplify the number of modes in a way. The aforementioned modal reduction process (20% of maximal coefficient limit) is not valid for square pulse since it simplifies the modal in a way the spatial form is not similar to reference form. Consequently, in this case initially the all twenty five identified modes were used to create modal modelled spatial square pulses of $\dot{\boldsymbol{w}}_{M.25.Squa.P1\,(x,T_F)}$, $\dot{\boldsymbol{w}}_{M.25.Squa.P2\,(x,T_F)}$, $\dot{\boldsymbol{w}}_{M.25.Squa.P3\,(x,T_F)}$, $\dot{\boldsymbol{w}}_{M.25.Squa.P4\,(x,T_F)}$ and $\dot{\boldsymbol{w}}_{M.25.Squa.P5\,(x,T_F)}$. Using try and error method, each time one last mode was eliminated from the model and spatial form of modal modelled square form was compared with reference square forms. Repeating this process, the first sixteen modes were minimum mode numbers that square pulses can be generated. Hence modes $\overline{\varphi}_{1(x)}$ to $\overline{\varphi}_{16(x)}$ are modelled (light pink region in Fig. 4.24) and the other modes are neglected (gray region in Fig. 4.24).

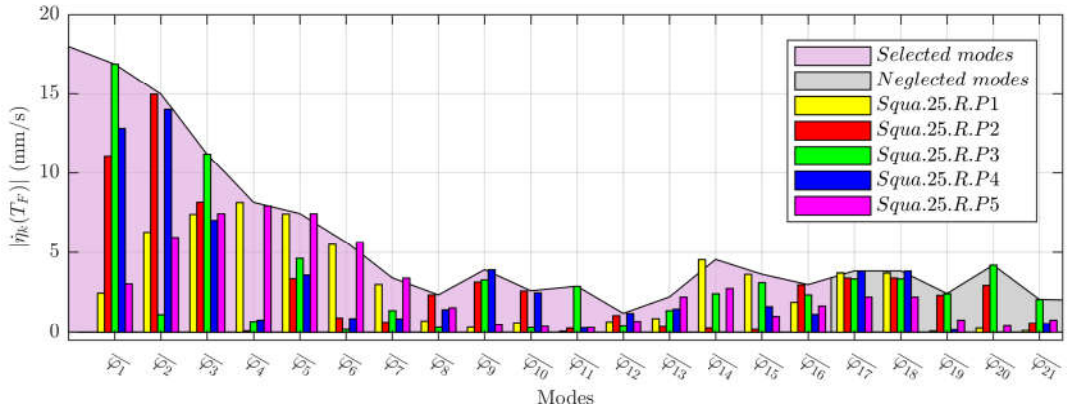

FIGURE 4.24: Absolute value of Modal Coefficients of Square spatial pulse with 25 mm pulse width; Yellow, Red, Green, Blue and purple respectively represents the modal coefficients for pulses with pulse center in P1, P2, P3, P4 and P5, The light orange region shows the modelled modes for experimental excitation and the gray region shows the neglected modes in the experiment.

The excitation signals of actuators were determined in a way that it is capable of exciting spatial square pulses (using Eq.2.34). The experimentally measured spatial vibration field ($\dot{\boldsymbol{w}}_{E.25.Squa.P_i\,(x,T_F)}$) at focusing time $t = T_F$ are depicted with reference spatial square pulses ($\dot{\boldsymbol{w}}_{R.25.Squa.P_i\,(x,T_F)}$) and modal modelled forms ($\dot{\boldsymbol{w}}_{M.25.Squa.P_i\,(x,T_F)}$) in Fig. 4.25.left with blue, red and black colors respectively. Regarding to spatial forms in Fig.4.25.left, the experimental result of $\dot{\boldsymbol{w}}_{E.25.Squa.P1\,(x,T_F)}$, $\dot{\boldsymbol{w}}_{E.25.Squa.P4\,(x,T_F)}$ and $\dot{\boldsymbol{w}}_{E.25.Squa.P5\,(x,T_F)}$ are acceptable approximation of their expected spatial form $\dot{\boldsymbol{w}}_{M.25.Squa.P1\,(x,T_F)}$, $\dot{\boldsymbol{w}}_{M.25.Squa.P4\,(x,T_F)}$ and $\dot{\boldsymbol{w}}_{M.25.Squa.P5\,(x,T_F)}$. In the modal space however, it is clear that the highest mode are not so satisfactorily excited (just as it was the case for 10 mm Sinc pulses). This is also confirmed by criterion Table 4.7. These errors between experimental and expected form can be due to the cross talk between the modes, which will be studied later in this chapter.

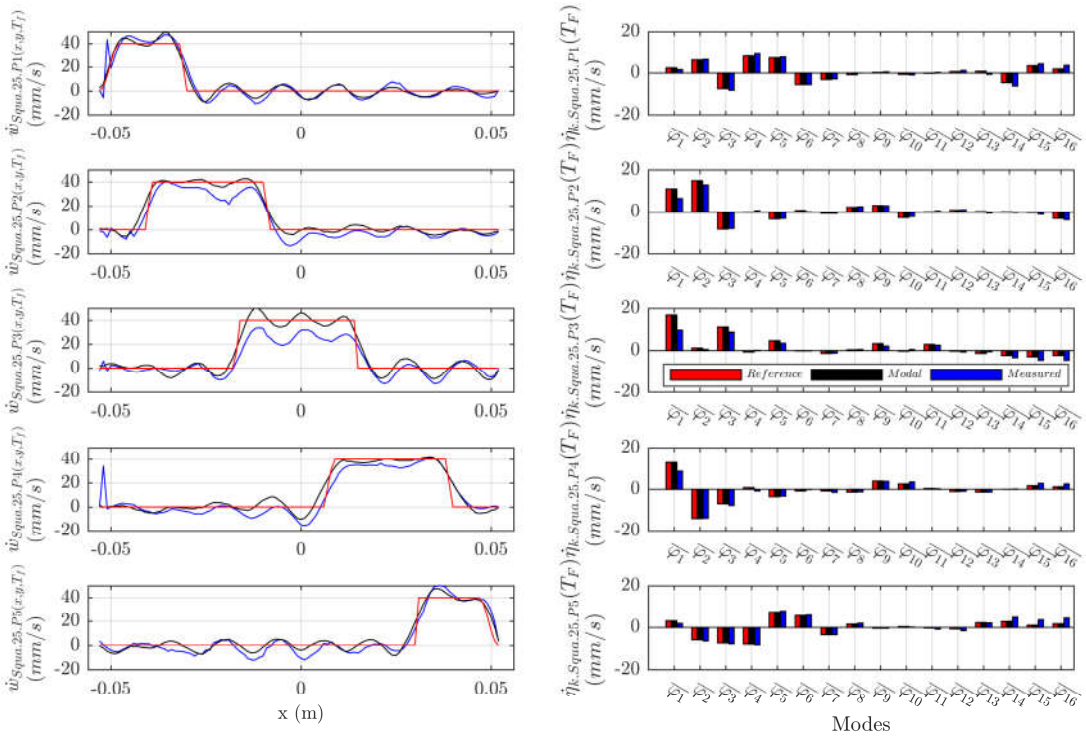

FIGURE 4.25: **Left:** The Reference (red color) $\dot{\boldsymbol{w}}_{R.25.Squa.P_i\,(x,T_F)}$, Modal modelled (black color) $\dot{\boldsymbol{w}}_{M.25.Squa.P_i\,(x,T_F)}$ and experimentally measured (blue color) $\dot{\boldsymbol{w}}_{E.25.Squa.P_i\,(x,T_F)}$ spatial sinc in different location on the beam (from top to below: $P1$, $P2$, ... and $P5$). **Right:** The modal coefficient of Reference spatial form $\dot{\eta}^*_{k.R.25.Squa.P1}$ (red bars), modal coefficient of modal modelled spatial sinc $\dot{\eta}^*_{k.M.25.Squa.P1}$ (black bars) and modal coefficient of experimentally excited spatial form $\dot{\eta}^*_{k.E.25.Squa.P1}$ (blue bars).

Pulse center	P_1	P_2	P_3	P_4	P_5
Covariance factor	0.9656	0.8106	0.6508	0.8946	1.0054

TABLE 4.7: Covariance comparing factor of experimental and reference Square pulse of 25 mm

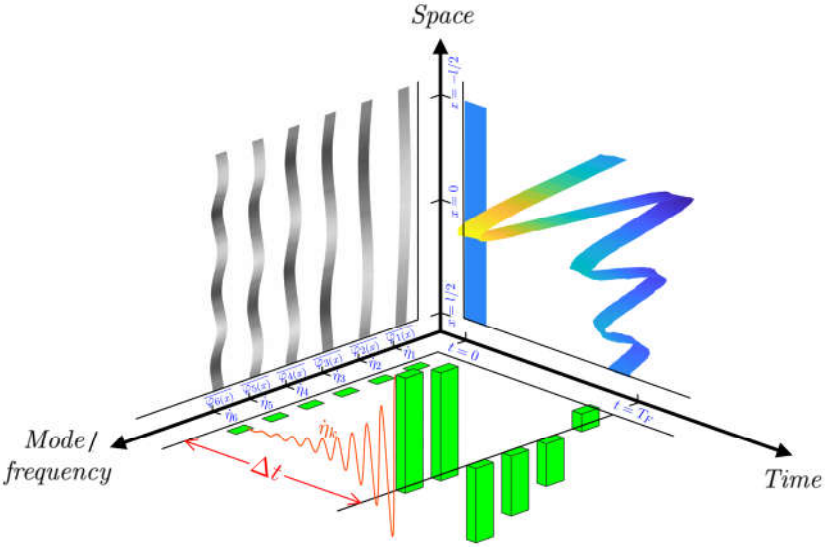

FIGURE 4.26: Spatio-Tempral-Modal diagram of desired vibration; initial spatial from of vibration (blue) with its corresponding modal coefficients at $t = 0$ (green bars), final spatial form of sinc pulse at $t = T_F$ and the corresponding modal coefficients (green bars at $t = T_F$), and the transient duration indicated with Δt in red color

4.4 Temporal Dynamics in Local Vibration Generation

In previous sections the feasibility of exciting any arbitrary spatial form using modal decomposition has been discussed. However only the results at the focusing moment have been presented, while their transient was not discussed.

In this part the haptic display is supposed to be at rest initially. For haptic applications, the passage from rest point to the final desired spatial form should be instantaneous. In Fig. 4.26, for instance the initial spatial form vibration is zero and the objective is to arrive the final spatial form as a sinc pulse created on the side of the beam and ideally this should happen instantaneously. This, of course, is not realistic and in this part we will discuss the way and the reason to control the transients of the modes. As it is depicted in Fig. 4.26 the problem will be addressed directly in the modal space, by specifying and possibly accelerating the transient for each modes.

Rather than achieving directly the transient of spatial form, this section will tackle this problem via transient of the modes (meaning that, initially the transient of each mode

will be studied and determined to its final value using an experiment case). Afterward, explanation will be given about how to determine excitation voltage signals to the actuators. At last the transient of vibration of the beam will be discussed.

4.4.1 Setting the Raising of Mode

Here we discuss the specification of the dynamic of the modes in more detail. This problem which has already been evocated in chapter 2 is that it requires to define the voltage applied to the actuators. We want to impose the $\dot{\eta}_k(t) = \dot{\eta}^*_{kR} cos(\omega_k t) e^{\kappa\zeta_k\omega_k t}$, whose Laplace transform is:

$$\dot{\eta}_k(s) = \frac{\dot{\eta}^*_{kR}(s - \kappa\zeta_k\omega_k)}{s((s - \kappa\zeta_k\omega_k)^2 + \omega_k^2)} \tag{4.5}$$

By taking into account the transfer function of the mode, presented in the second chapter Eq. 2.23 :

$$v_{kp}(s) = \frac{s^2 + 2\zeta_k\omega_k + \omega_k^2}{\alpha_k}\eta_k(s) \tag{4.6}$$

substituting Eq.4.5 into Eq.4.6, and applying inverse Laplace transform yields the voltage to apply to the actuator:

$$v_{kp}(t) = \frac{\dot{\eta}^*_{kR}\omega_k}{\alpha_k(\kappa\zeta_k + i)}((\kappa^2 + 2\kappa)\zeta_k^2 + 2(n+1)\zeta_k i)e^{(\kappa\zeta_k\omega_k + \omega_k i)t} cos(\zeta_k\omega_k t) \tag{4.7}$$

In practice, $\zeta_k \ll 1$, so we applied the simplified expression:

$$v_{kp}(t) \simeq \frac{\dot{\eta}^*_{kR}\omega_k}{\alpha_k(\kappa\zeta_k + i)}((2(n+1)\zeta_k i)e^{(\kappa\zeta_k\omega_k + \omega_k i)t} cos(\zeta_k\omega_k t) \tag{4.8}$$

Afterward, the excitation phase will be stopped and the mode will decay naturally. To be more precise, each mode will experience two transient; the first one is the excitation phase (forced oscillation) for $0 \leq t < T_F$, and the second is when mode experiencing natural damping (free oscillation) in absence of external force $T_F \leq t < \infty$. In this study, these two stages are respectively called **transient** and the **post-transient**. The important moment T_F when the mode arrives to its target value (and the spatial form will be created) will be called **end-transient** or **focusing moment**. The dynamic of all modes are defined whereby each mode arrives to its final modal value at time $t = T_F$.

Suppose that reference spectrum of Fig. 4.26 must be obtained, then the transient of each mode according to the developpment above and represented on Fig. 4.27 in the

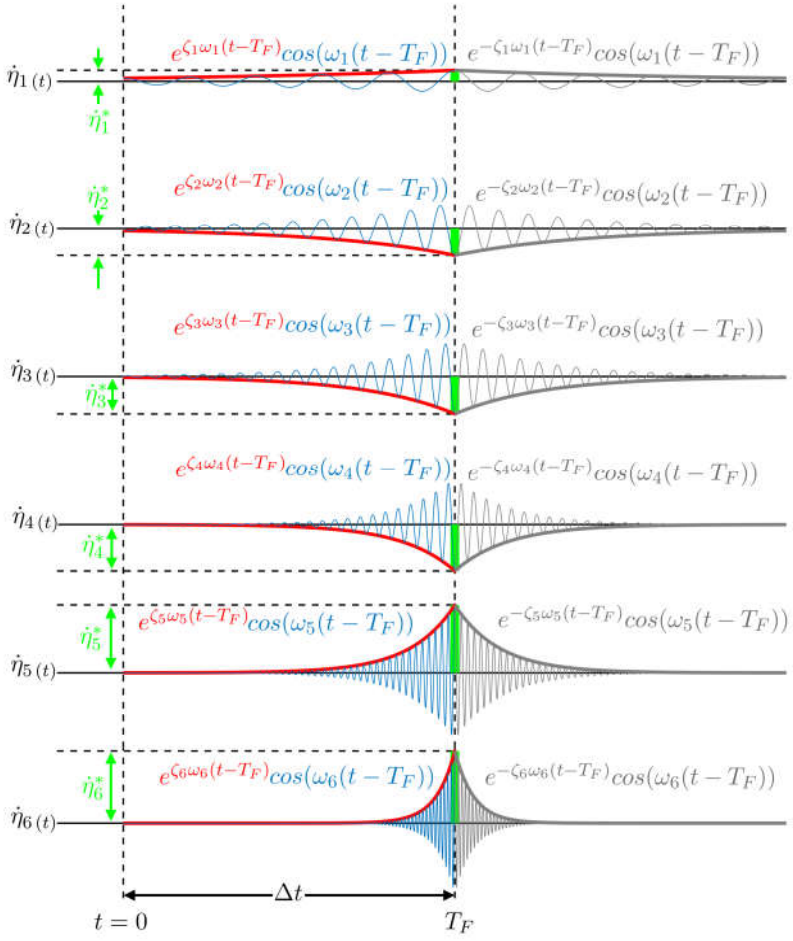

FIGURE 4.27: Transient of modes; this figure shows how to determine the temporal behavior of mode. The red line is exponential envelope during excitation, light blue is the excitation sinusoidal function of each mode (at its resonance frequency), the green is the desired modal coefficient value and gray is the natural decay of the mode at post-transient

case κ (natural ascend speed of the free modes).

Secondly, in this study we have considered that the modes are excited at their resonance frequency ω_k, hence, cosinusoidal signal is defined for each mode whereby it has the zero angular value at $t = T_F$, resonance angular frequency of each mode ω_k and the modal amplitude of $\dot{\eta}^*_{k.R}$ at $t = T_F$ (there are highlighted in light blue color in Fig. 4.27). For the amplitude of the oscillation of mode, we have inspired from natural behavior of each mode, meaning that an exponential function of $e^{\zeta_k\omega_k(t-T_F)}$ are defined in a way that in $t = T_F$ it arrives to unity amplitude (illustrated by red envelope in Fig. 4.27). By this definition, it is obvious that the transient time of overall vibration evaluation to arrive desired spatial form (Δt) will be dominated with the mode which has longer rise time (for this example case is first mode). According to above mentioned explanation, the

dynamic of each mode $\dot{\eta}_{k.R.25.Squa.P5}(t)$ is illustrated with the cosinusoidal at resonance (blue curves), with exponential envelope (red envelopes) and the final modal coefficient amplitude (green bars).

After, exciting of beam at transient phase, all the modes will decay according to their natural behavior in free oscillation to arrive to their equilibrium point. Meaning that they will be damped with exponential amplitude of $e^{-\zeta_k \omega_k (t-T_F)}$ and keeping the same frequency as in the excitation. The decaying part of the modes are shown in gray color in Fig. 4.27. It should be highlighted again this post-transient of modes is due to natural behavior not any excitation is done on any of beams.

4.4.2 Transient of modes for an experimental case

Following the aforementioned explanation to determine transient of modes, the transient of modelled modes for exciting spatial sinc pulse at $P5$ location (pulse center in $x_{Csp} = +46mm$) are determined whereby they arrive to their final value ($\dot{\eta}^*_{k.R.25.Sinc.P5}$) at $T_F = 25\ msec.$ The light blue plots in Fig. 4.28 illustrated the dynamic of mode during transient. The decay of the modes for post transient is expected as gray lines in the same figure.

Measured experimental value of the vibration field $\dot{\boldsymbol{w}}_{E.25.Squa.P5\,(x,t)}$, has been decomposed to the modes using the Eq. 2.22 and the experimental temporal evolution of the modes have been obtained for six modes of $\dot{\eta}_{1.E.25.Sinc.P5}(t)$, $\dot{\eta}_{2.E.25.Sinc.P5}(t)$, $\dot{\eta}_{3.E.25.Sinc.P5}(t)$, $\dot{\eta}_{4.E.25.Sinc.P5}(t)$, $\dot{\eta}_{5.E.25.Sinc.P5}(t)$ and $\dot{\eta}_{6.E.25.Sinc.P5}(t)$. These experimental values are depicted in dot dashed green lines in Fig. 4.28. The determined and experimental evaluation of the modes are comparable in this figure. For both transient and post-transient all the modes are following the resonance frequency and they are well in phase with the expected mode dynamic. The measured modes are following the same exponential envelope both during excitation ($0 \leq t < T_F$) and expected decaying duration. The most important is the modal coefficient value at end-transient $t = T_F$, which all the modes arrive the final value in phase with their reference value and aligned in $t = T_F$. To sum up, the experiment follows the expected theoretic values using the modal excitation technique.

To more investigate the transient dynamic of the mode, the vibration field of $\dot{\boldsymbol{w}}_{E.25.Squa.P5\,(x,t)}$ has been considered in its pulse peak position of $x = x_{Csp} = +46\ mm$, short-time fourier transformation has been applied to the temporal evaluation of $\dot{\boldsymbol{w}}_{E.25.Squa.P5\,(0.046,t)}$ at

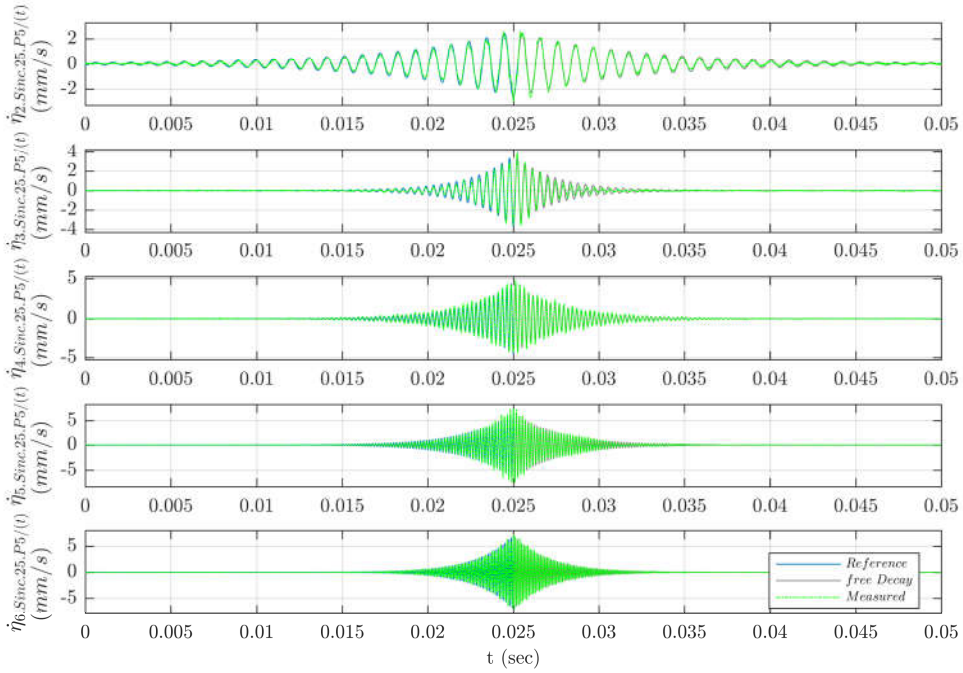

FIGURE 4.28: Temporal behavior of modes during exciting $\dot{\boldsymbol{w}}_{E.25.Squa.P5\,(x,t)}$; light blue is predetermined value for dynamic of modes, gray is the expected free decay of the modes and the green is the experimental values $\dot{\eta}_{k.E.25.Squa.P5}(t)$

this point. The result is depicted for duration of $t = 0 - 50\ msec$ and frequency band of $f = 0 - 10\ kHz$ in Fig. 4.29. This figure, shows the modal coefficient dynamic $\dot{\eta}_{k.E.25.Squa.P5}(t)$ multiplied to the mode shape value at $x = +46\ mm$ ($\overline{\varphi}_{k(x=46\ mm)}$). As is seen, the six frequency of $0.368\ kHz$, $0.963\ kHz$, $2.253\ kHz$, $3.907\ kHz$, $5.719\ kHz$ and $8.166\ kHz$ are related to mode coefficients $\dot{\eta}_{1.E.25.Squa.P5(t)}\overline{\varphi}_{1(x=46\ mm)}$, $\dot{\eta}_{2.E.25.Squa.P5(t)}$ $\overline{\varphi}_{2(x=46\ mm)}$, $\dot{\eta}_{3.E.25.Squa.P5(t)}\overline{\varphi}_{3(x=46\ mm)}$, $\dot{\eta}_{4.E.25.Squa.P5(t)}\overline{\varphi}_{4(x=46\ mm)}$, $\dot{\eta}_{5.E.25.Squa.P5(t)}\overline{\varphi}_{5(x=46\ mm)}$ and $\dot{\eta}_{6.E.25.Squa.P5(t)}\overline{\varphi}_{6(x=46\ mm)}$. At $t = T_F$ all modes arrive to their maximal values. In temporal domain, all six modes are raising during transient $0 \leq t < T_F$, and they decay with the same slope in past transient $T_F \leq t < 50\ m$.

4.4.3 Transient of Vibration

At this point, it has been demonstrated that the transient in the modal space are efficiently imposed. This is the result of the insight offered by the modal projection. On the other hand, the vibration dynamics on the actual transient of the structure is not exactly known. The vibration field at middle line of the beam was measured and it is represented as a surface showing the vibration velocity as a function of space and time

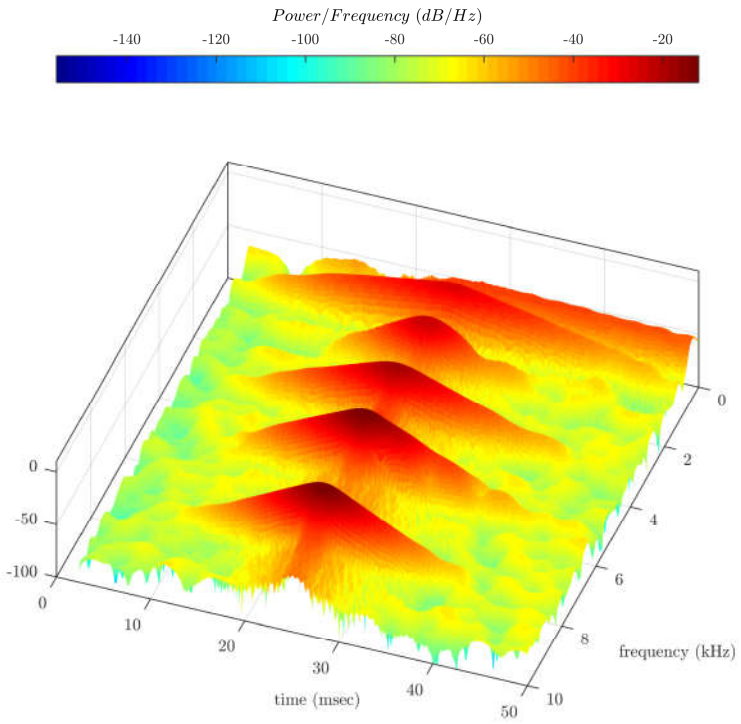

FIGURE 4.29: The short-time Fourier transform of $\dot{\boldsymbol{w}}_{E.25.Squa.P5\,(x=+46\ mm,t)}$

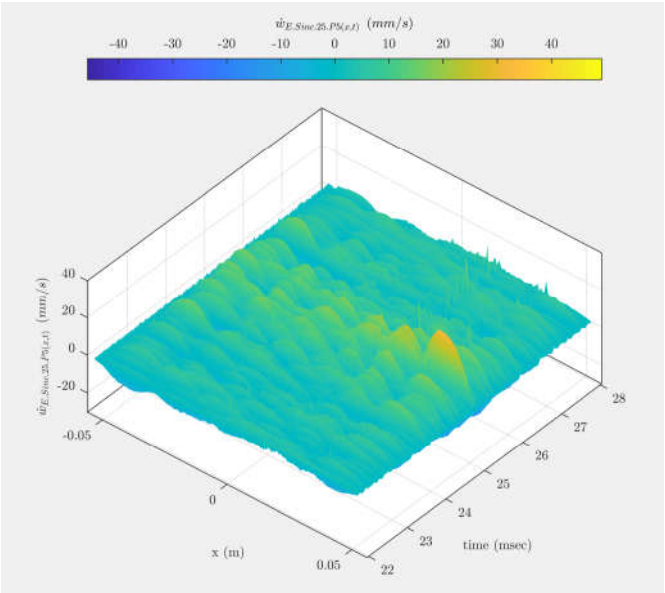

FIGURE 4.30: Spatio-Temporal evaluation of vibration field of the beam for generating spatial sinc pulse with pulse center at $x_{Csp} = 0.046\ m$

coordinates in Fig. 4.30. In this figure, the x axis is the length axis of the beam which is limited between $-l/2$ and $l/2$ the boundaries of the beam. The time axis (y axis) is limited between 22 ms – 28 ms since the high amplitude vibration occurs in this time

range. The z axis shows the vibration velocity amplitude in mm/s. The first remark in this figure is the comparatively high amplitude of the vibration at $x = 46\ mm$ on the space which confirms the focusing of the mechanical waves at end-transient in desired point. Second remark is that vibration amplitude of the other points during transient and post-transient are not negligable and might influence the detection by the finger. This is the topic of the study of the next chapter.

4.5 Discussion

According to the focusing result of the first prototype which is presented in Fig. 4.7, by implementing modal synthesis of vibration it is possible to focus vibration on different location of structure. Meanwhile, the experimental results obtained for different spatial form (shown in Fig. 4.17, Fig. 4.23 and Fig. 4.25) confirms that any kind of spatial form can be rendered using modal decomposition and modal excitation of vibration. Although, theoretically infinite number of modes is required to well excite a precise vibration field, by a well-defined reduced modal model, an acceptable approximation of the spatial form can be generated. The square spatial pulse is a good example of rendering complex spatial form using modal synthesis, the form requires infinite number of modes to be excited, while in study it has been excited with reduced modal model whose form is shown in Fig. 4.25.

Meanwhile, the feasibility of controlling spatial pulse center or, in another term, possibility of focusing vibration field in different zone of the beam have been proven by experimental results (which is illustrated in Fig. 4.17, Fig. 4.23 and Fig. 4.25). Additionally, spatial pulses with different pulse width can be generated as shown in experimental results. However cross-talk of nearly placed modes can some time afflict the quality spatial form, it can be avoided using re-orthogonalized modes as explained in section 3.11. Based on the observation from the experiment some important remarks can be discussed which are presented in following sub-sections.

4.5.1 Pulse Width and Modal Model Size

Regarding to the measured spatial sinc pulses, any pulse width of sinc function can be rendered by modal synthesis of vibration. The question is that, what is the costs of

exciting very narrow (spatial Dirac) spatial sinc pulse? To answer, we have look for the modelled modes for three different pulse width of Sinc with 25 mm, 18 mm and 10 mm pulse width whose modelled modes are illustrated in Fig. 4.16, Fig. 4.18 and Fig. 4.20.

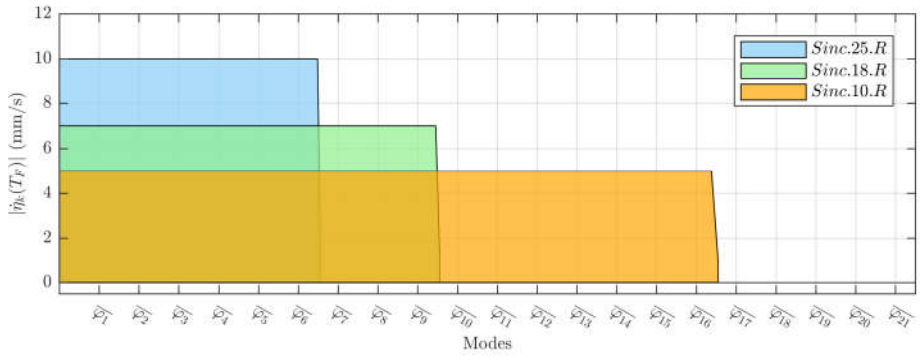

FIGURE 4.31: Relationship between spatial pulse width and required modes

Reproducing the three reduced modal model figures in Fig. 4.31, the relationship between pulse width and modes can be well explained. In This figure, the light blue region is the required modes with their required amplitude for exciting sinc pulse with 25 mm, the light green region is required modes region and their amplitude for exciting 18 mm width spatial Sinc and light orange is the regions of modes and their amplitude in order to render 10 mm Sinc pulse. Regarding to this figure, the more narrower the pulse width then the more number of modes are required to be excited. Additionally, for exciting the same amplitude of vibration, the more pulse width get narrower the less amplitude of participation of mode is required. As example, for exciting 10 mm and 25 mm sinc pulse, the 10 mm sinc required wider mode number to be synthesis comparing to 25 mm sinc, adversely it require less excitation amplitude of each independent mode comparing to 25 mm sinc. Since mode shapes of experimented beam is approximately sinusoidal (similar to eigenfunctions of Fourier series), This is analogous to Fourier transform of temporal sinc function whose band width grows by reducing the pulse width while spectrum amplitude declines.

4.5.2 Pulse Form and Modal Model Size

It would be interesting to investigate the influence of pulse form on the modal model. Lets consider the pulses with pulse width of 25 mm with forms of Sinc, Bump and Square. The reduced modal model of exciting these form have been shown in Fig. 4.24, Fig. 4.22 and Fig. 4.24. By re-plotting all of them in the same figure, Fig. 4.32 is

obtained. In this figure, the light blue is require modal model region of sinc pulse, the region in light red is for modal region of bump pulse and require modal model region of square pulse is shown in light purple color.

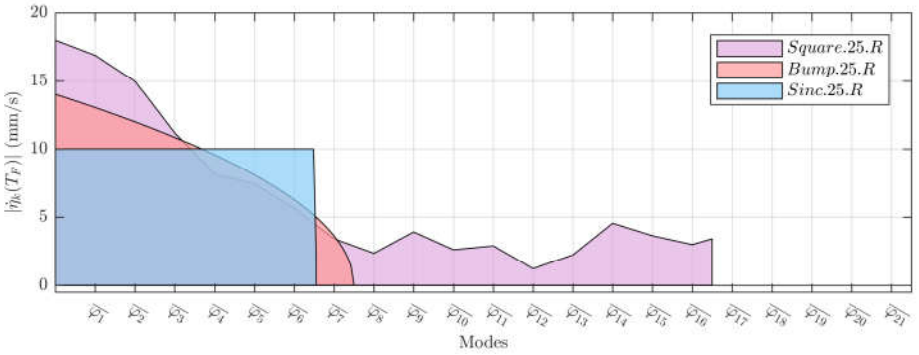

FIGURE 4.32: Relationship between spatial pulse form and required modes

For exciting the same pulse width, sinc requires less number of modes and less amplitude of mode for low frequency modes. The bump pulse requires a little bit more number of modes (one more mode comparing to sinc) in comparison of sinc pulse at the same time for low frequency modes it requires higher amplitude of vibration. Despite, bump require more number of modes and more amplitude in lower frequency modes in comparison to sinc pulse, the bump pulses have smoother spatial form in the focusing moment compared to the sinc pulses. In order to excite square spatial pulse even more number of modes are required (for this case is sixteen modes) and higher amplitude of modes is needed in low frequency modes. Briefly, for exciting sharper edge or spatially complex form the higher number of modes are needed. Regarding to the experimental results obtained for square pulse generation in Fig. 4.25, there are significant error between square pulse spatial form determined by modal model and its experimental measured value. It can be due to the cross-talk of the modes, hence an improvement will be proposed to this issue in next subsection.

4.6 Improvements

4.6.1 Spatial Precision with Orthogonalization of Mode Shapes

Regarding to the square pulse generated in center of beam $\dot{\boldsymbol{w}}_{E.25.Squa.P3\,(x,T_F)}$ in Fig. 4.25. left third figure from top and comparing to its expected value $\dot{\boldsymbol{w}}_{M.25.Squa.P3\,(x,T_F)}$,

a significant difference between two spatial form is detected. The reason of this error is nonorthogonality of identified modal base and a solution of this spatial error is investigated with orthogonalization of experimentally obtained modes and creating a new orthogonal bases.

The main reason for such spatial error would be due to the cross talk of the modes. Meaning, when a mode is excited in practice some neighbour modes are also excited due to the bandwidth sharing with each other. To investigate this issue, all the normalized identified mode which were used for exciting square spatial pulse ($\overline{\varphi}_{1(x)}$ to $\overline{\varphi}_{16(x)}$) were projected on themselves and the result which a 17×17 square matrix is depicted in Fig.3.11. left. This figure shows that the identified modes are not completely decoupled, in another term, the identified modes are not completely orthogonal. For instance, mode $\overline{\varphi}_{13(x)}$ and mode $\overline{\varphi}_{14(x)}$ have a coupling factor of around 0.5, ideally this value should be zero (See chapter 3 Eq. 3.17a Orthogonality property).

To solve this issue, a set of orthogonalized modal base ($\overline{\varphi^{\dagger}_{1(x)}}$ to $\overline{\varphi^{\dagger}_{17(x)}}$) has been recreated using Gram-Schmidt method presented in section 3.17a. For the purpose of checking cross talk of these orthogonalized mode, they were projected to each other and the resulted cross talk matrix is illustrated in Fig. 3.11. right. This figure shows that the constructed orthogonalized modal base is completely orthogonal.

Using the orthogonalized modal base the reference square spatial pulse in the center of the beam have been projected to the orthogonalized modes. Using orthogonalized modes ($\overline{\varphi^{\dagger}_{1(x)}}$ to $\overline{\varphi^{\dagger}_{16(x)}}$) the excitation signal of actuator have been determined and the structure have been excited. The measured spatial deformation of vibration $\dot{\boldsymbol{w}}_{E.25.Squa.P3.Orth\,(x,T_F)}$ at $t = T_F$ obtained as it is shown in Fig. 4.33 green color. The obtained spatial form is more similar to the reference spatial sinc in the center (red plot in the same figure). Comparing this square spatial pulse obtain with orthogonalized modes ($\dot{\boldsymbol{w}}_{E.25.Squa.P3.Orth\,(x,T_F)}$) and identified modes ($\dot{\boldsymbol{w}}_{E.25.Squa.P3\,(x,T_F)}$ shown in with blue color in Fig. 4.33 the spatial improvement of pulse form is obvious.

Pulse center	P_1	P_2	P_3	P_4	P_5
Covariance factor			0.9017		

TABLE 4.8: Covariance comparing factor of experimental and reference Square pulse of 25 mm obtained by orthogonalized modes

4.6.2 Accelerated Mode Dynamics

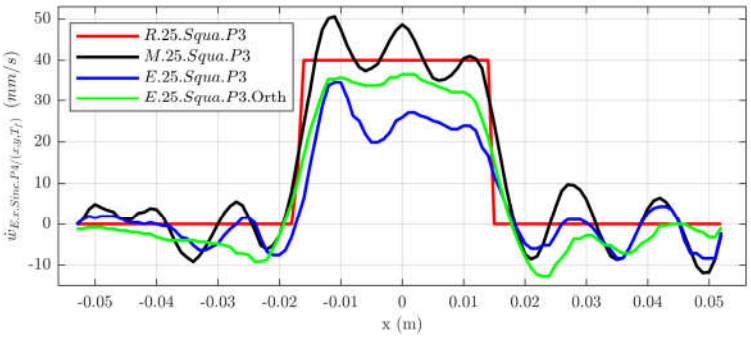

FIGURE 4.33: Spatial Square Pulse in center of beam: red is reference spatial form $\dot{\boldsymbol{w}}_{R.25.Squa.P3\,(x,T_F)}$, black is modal modelled spatial form $\dot{\boldsymbol{w}}_{M.25.Squa.P3\,(x,T_F)}$, blue is experimental spatial form obtained with identified modes $\dot{\boldsymbol{w}}_{E.25.Squa.P3\,(x,T_F)}$ and green is experimental spatial form obtained by orthogonalized modes $\dot{\boldsymbol{w}}_{E.25.Squa.P3.Orth\,(x,T_F)}$

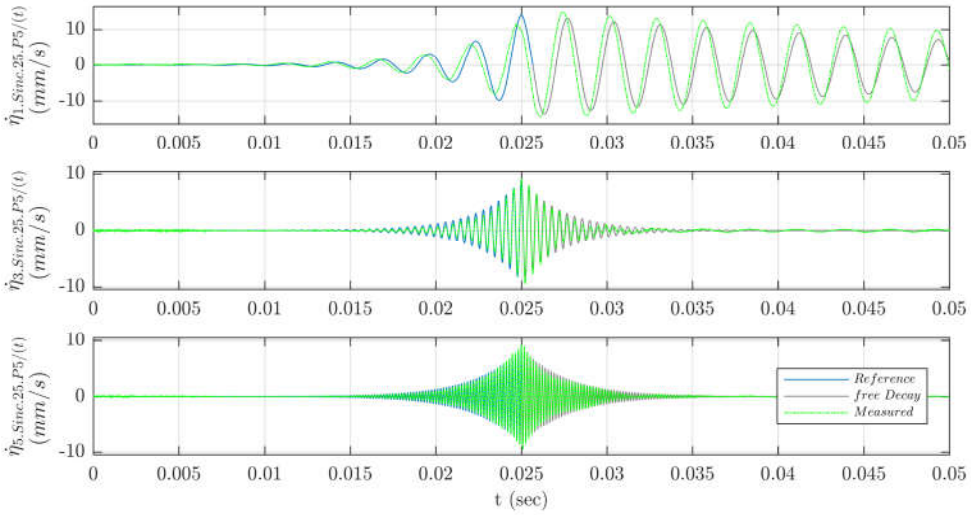

FIGURE 4.34: Dynamic of modes; for three excited modes for exciting $\dot{\boldsymbol{w}}_{E.25.Squa.P3\,(x,t)}$, blue lines are determined vibration in excitation duration, gray lines are natural decay of modes and the dot-dashed green lines are the measured transient of modes

In some cases, some modes have very long rise time which cause that the transient of vibration Δt to be so long. This is not desirable due to two reason; firstly as it was mentioned early for a haptic interface application a fast response of the structure is required secondly for this study case it makes the measurement so long that I have saturated the memory of measurement equipments.

To solve this problem, these modes are excited in faster exponential function. Meaning that, instead of exciting modes with an exponential envelop of $e^{\zeta_k \omega_k (t-T_F)}$, it is excited with faster exponent coefficient as $e^{n\zeta_k \omega_k (t-T_F)}$ where $n > 1$. One example for application of this mode excitaion acceleration is for exciting sinc pulse in center of beam

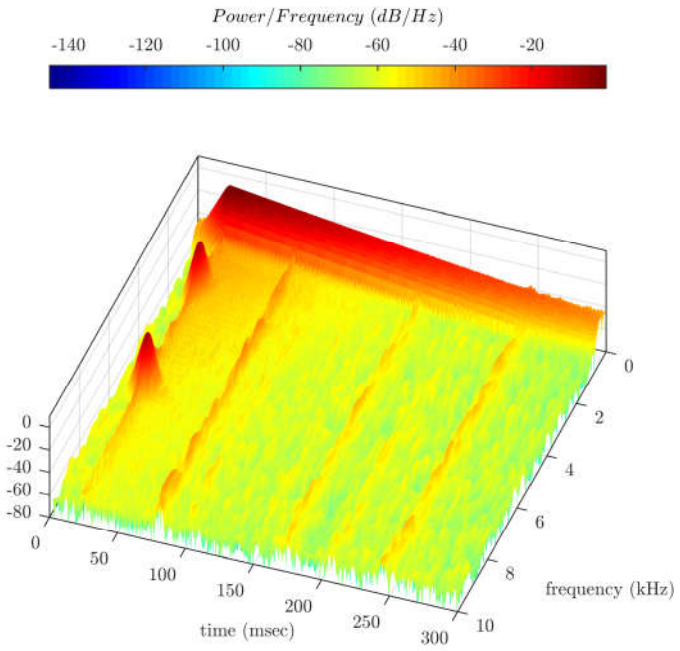

FIGURE 4.35: Short-time fourier transform of $\dot{\boldsymbol{w}}_{E.25.Squa.P3\,(x=0,t)}$

$\dot{\boldsymbol{w}}_{E.25.Squa.P3\,(x,t)}$ for the first mode. For given spatial form, the first mode has significantly high amplitude(10 mm/s) and since its rise time is far longer than other modes (around 200 $msec$) as a result an exponential envelope has been defined with n=1 time faster than its natural exponential factor (shown in light blue color in the same Fig. 4.34). It is evident that the first mode (Top plot in Fig. 4.34) has more rapid passage from equilibrium to final value at $t = T_F$, while its decay which is based on its natural decay speed take too long which does not fit inside 50 ms.

This issue can be seen from another view. The vibration velocity of the center of beam $x = 0$ where spatial pulse is expected to have its peak there has been taken into account $\dot{\boldsymbol{w}}_{E.25.Squa.P3\,(x=0,t)}$. The short-time Fourier transform have been applied to this signal and its result is depicted in Fig. 4.35. According to this spectrogram three modes have been excited.The high power signals at 0.963 kHz and 2.253 kHz are corresponding to the modes $\overline{\varphi}_2$ and $\overline{\varphi}_3$ respectively. These two modes have the same slope in excitation and decaying. While mode one is excited with faster slope and decay with slower slope(look around 0.368 kHz) which does not arrive to equilibrium even at 300 $msec$. Of course exciting a mode with acceleration has costs. For this case the draw back of exciting a mode in accelerated requires a higher amplitude of the excitation voltage for correspond mode. The excitation voltage signal of first channel for exciting the spatial sinc $\dot{\boldsymbol{w}}_{E.25.Squa.P3\,(x=0,t)}$ with normal excitation of first mode and accelerated

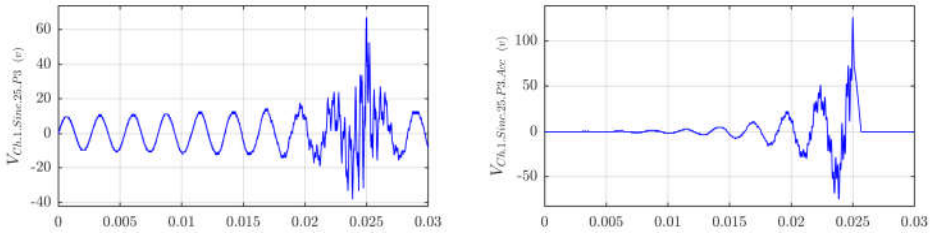

FIGURE 4.36: Excitation voltage signal of first actuator set for exciting $\dot{\boldsymbol{w}}_{E.25.Squa.P3}(x,t)$;**Left**. normal excitation of all modes **Right** accelerated excitation of first mode and two other modes excited normally

excitation of first mode are shown in Fig. 4.36 left and right respectively. Regarding to this figure for accelerating excitation only the first mode the voltage amplitude margin grows almost double times.

4.6.3 Conclusion

This chapter was dedicated to the validation of the proposed strategy to realize a given velocity distribution on a structure. First, a simple beam using a single actuator was realized and experiments have confirmed that a single actuator could induced to control several modes by focusing a shape at different location. Then, a set up with more actuator was designed to test different fields of vibration requiring more complex contribution of the modes. A criteria to truncate the number of modes and to compare the performance of the strategy for different modal spectrum has been proposed. Overall, the possibility of addressing variety of velocity fields has been confirmed as long as the spectrum is not high. As discussed, an orthogonalization of modal base can mitigate this limitation. Finally, the possibility to control the transient has been demonstrated. In the next chapter, we present some haptic evaluation of the focalization.

Chapter 5

Psychophysical evaluation

The behavior of the vibration of haptic display was investigated in two independent domain of time and space in previous chapters. While the vibration dynamic is a temporal evolution of the spatial forms in the space, it has been shown with experimental study that at a given time $t = T_f$, the spatial vibration form can be modulated in a way that the vibration peak focuses in a certain location on the haptic display achieving the control of the pulse center. But what is happening during the transient and post transient (time before $t = T_f$ and after $t = T_f$) was not investigated. In this chapter, we optimize the vibration profile of the modes in such way that the evolution of the vibration form is more focused around time $t = T_f$. Then, we present the result of a psychophysical study which illustrates from the point of view of user the performance of the device.

5.1 Optimized vibration profile

5.1.1 Spatio-Temporal evolution of vibration with an non-optimized profile

In order to illustrate the transient of the vibration before and after the time of focusing T_f, the evolution of the vibration of the central line of the beam is depicted in Fig. 5.1. In this figure, the x axis shows the space domain in length direction of the beam: $x = -0.052$ is the left boundary and $x = 0.052$ is the right boundary. The axis t is the time domain, limited between 21 ms and 29 ms. For this try, we synthesized a Sinc

function form with a pulse center at $P4$ with a pulse width of 18 mm (Fig. 4.12 in page 74). To interpret this figure, we chose a single point x_0 on x axis and we look at its evolution along the t axis. We obtain then the evolution of the velocity at $x = x_0$ in the time domain. If now we chose a certain time $t = t_0$ and if we look at the evolution along the x axis, then we will have the spatial vibration form of the beam at $t = t_0$.

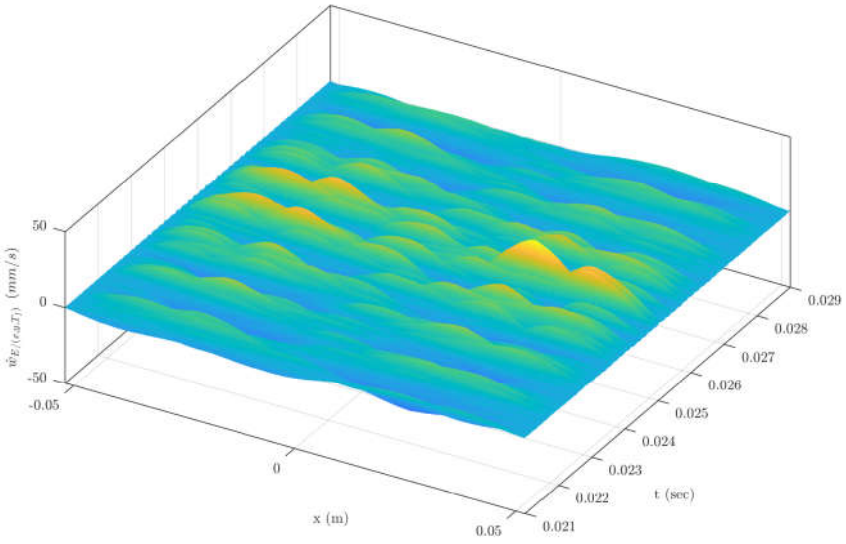

FIGURE 5.1: Spatio-Temporal evolution of vibration on the beam for exciting $Sinc.18.P4$

In this example, there is a peak of vibration at $t = 25\ ms$ in accordance with the spatial form synthesised. However, a time a bit before and bit later (transient and post-transient)there are significant vibration peaks in zones which are not targeted and located at the left side of the beam. If we project the figure 5.1 on the vertical plan $(x, \dot{w}_E)$, the temporal evolution of the vibration will be set back to back as depicted in Fig. 5.2.

This figure illustrates what a finger experiences as haptic feeling during the exciting of the beam during transient and post transient. It shows that a finger located at $x = 24\ mm$ will experience a high level of vibration amplitude velocity according to the vibration form. But it shows that a second finger located at $x = -24\ mm$ will also experience vibration peak with approximately the same amplitude, but in a different time, the delay between the two peak is less than one millisecond. Therefore, the perception would be a global or multi-local haptic feeling rather than single point local feeling. This explanation clarifies the transient problem of the vibration when using the modal decomposition with no precaution. In the following section, we are going to find a solution in order to reduce the vibration amplitude of non targeted zones during transient and post transient.

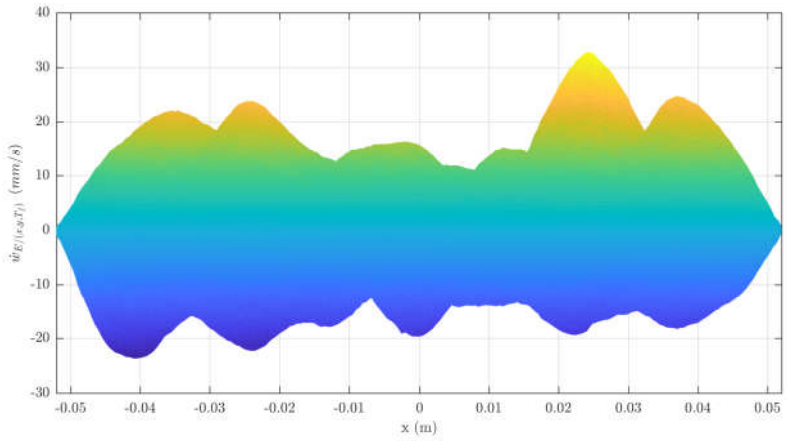

FIGURE 5.2: Evaluation of vibration velocity of $Sinc.18.P4$ for the time between 21 ms to 29 ms

5.1.2 Optimized vibration profile

In order to reduce the vibration amplitude in the non-targeted zones, we add a temporal description of the vibration to the spatial description of the vibration. We specify that, the vibration amplitude of the non targeted zones during the transient and post transient should not pass a certain level. This criterium is called *the transient vibration amplitude margin* and for the aforementioned example, we define the transient vibration margin equal to 50%. It means that the vibration at the non-targeted zones should not exceed 50 % of the peak value during the focusing.

The vibration velocity field of the beam is then analyzed to the light of this new criterium, and we detect the time when the vibration field exceeds the margin limit of 15 mm/s leading to the Fig. 5.3 .left.

We remark that there are several time as well as several spatial zones which do not meet the criteria of the transient amplitude margin. The detected time on which the vibration field exceed the margin is noted and highlighted with red lines on the mode dynamic, as shown in Fig. 5.3 . Right.

This figure shows the contribution of the modes to excite non-desired peaks on the vibration field. For instance, if we consider $t = 24.5ms$ as an example, among the excited nine modes. The modes coefficients $\dot{\eta}_{2.R.18.Sinc.P4}$ and $\dot{\eta}_{3.R.18.Sinc.P4}$ have the strongest contribution to the spatial form. In order to reduce the vibration field amplitude in this time period we should act on these two modes meanwhile keeping the same amplitude

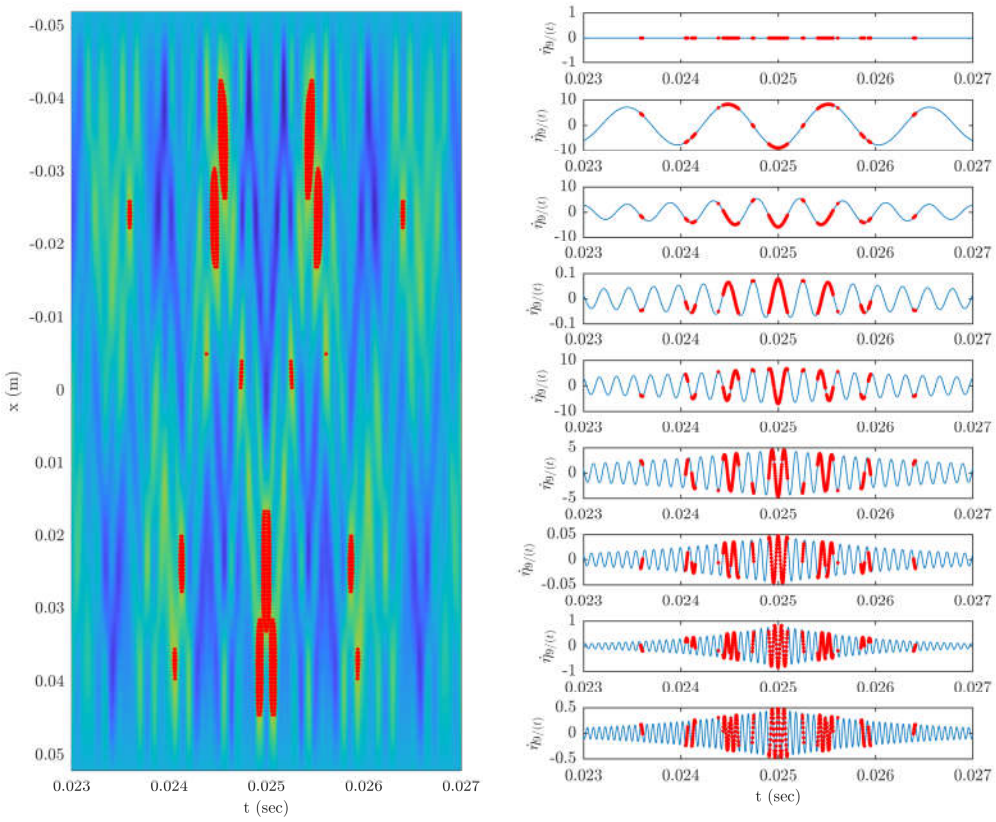

FIGURE 5.3: **Left**. Spatio-Temporal evaluation of vibration with highlighting the location and times where vibration velocity exceed the transient vibration margin limit (highlighted in red color). **Right**. The dynamic of the excited mode for *Sinc*.18.*P*4 the red color shows the time period in which vibration amplitude of structure exceed transient vibration margin

of the modal coefficient at $t = 25\ ms$. To realize this, rather than exciting these two modes with their natural exponential coefficient $e^{\zeta_k \omega_k (t-T_F)}$, we will excite them with an accelerated exponential excitation as $e^{\kappa \zeta_k \omega_k (t-T_F)}$ as already presented in equation 2.33 in page 37. In this excitation $\kappa > 1$, so that the mode will arrive to the same final value at $t = T_f$ but with an exponential modulation faster than $\kappa = 1$. As a result the modal coefficients of the modes have lower values at $t = 24.5$. This means that we can excite the same desired spatial form at $t = T_f = 25\ ms$ and avoid the undesired vibration peak at the left side of the beam at $t = 24.5\ ms$.

The same process can be applied to reduce vibration peaks at $t = 24.9\ ms$ and $t = 25.1\ ms$ by accelerating the excitations of the modes 5 and 6. The four modes (2, 3 , 5 and 6) have been excited with accelerated excitation as $e^{7\zeta_2 \omega_2 (t-T_F)}$, $e^{3\zeta_3 \omega_3 (t-T_F)}$, $e^{5\zeta_5 \omega_5 (t-T_F)}$ and $e^{3\zeta_6 \omega_6 (t-T_F)}$. The acceleration coefficient of each mode κ has been

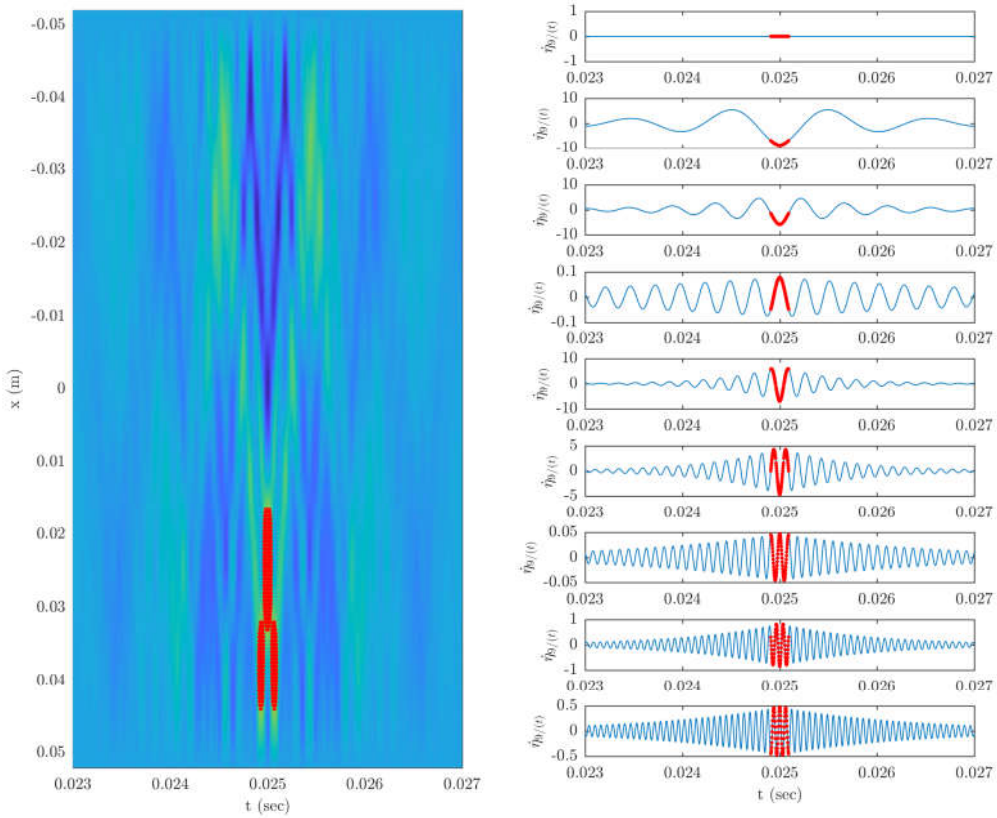

FIGURE 5.4: **Left**. Spatio-Temporal evaluation of vibration with highlighting the location and times where vibration velocity exceed the transient vibration margin limit (highlighted in red color) **after applying accelerated excitation to the modes 2, 3, 5 and 6. Right**. The dynamic of the excited mode for *Sinc*.18.*P*4 the red color shows the time period in which vibration amplitude of structure exceed transient vibration margin **after applying accelerated excitation to the modes 2, 3, 5 and 6**

obtained by try and error method.

The resulting vibration field of the beam is plotted Fig. 5.4. left. The transient vibration margin of 50% has been also applied to this vibration field and depicted in red color. As it is observable in this figure, the non desired vibration peaks have been eliminated. There are three period when the vibration velocity amplitude exceeds the margin; At $t = 25\ ms$ when the desired spatial form is obtained and in two time periods before and after the focusing moment. In order to eliminate them there are two solutions, either more accelerate the corresponding modes or include more modes to reduce the non desired form. The cost of the first solution is higher amplitude of excitation voltage and the cost of second chose is the complexity of the hardware (modalmodel).

The spatio-temporal figure of the obtained vibration form is depicted in Fig. 5.5. left.

It is clear that the application of the accelerated excitation of the modes have reduced the vibration amplitude in the non-targeted zones significantly and that the vibration velocity at $x = 25\ mm$ is a peak both in space and time.

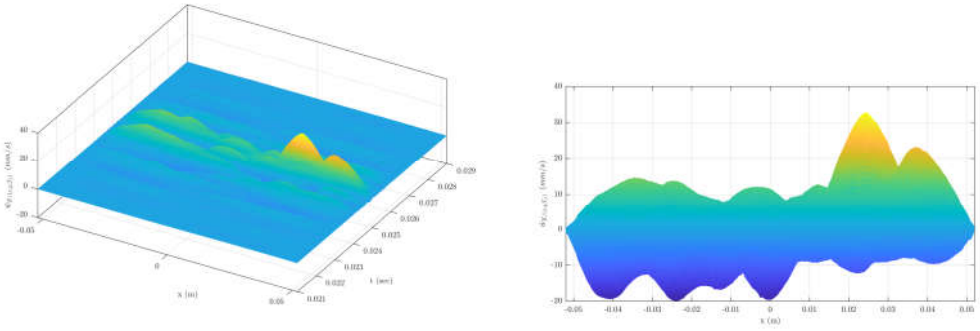

FIGURE 5.5: Left: Spatio-Temporal evolution of vibration on the beam for exciting $Sinc.18.P4$ with accelerated excitation of modes, Right: Evolution of vibration velocity of $Sinc.18.P4$ for the time between 21 ms to 29 ms with accelerated excitation of modes

Finally, the modal coefficient of exciting $Sinc.18.P4$ with accelerated and non accelerated form are depicted in solid blue and dashed red colors respectively in Fig. 5.6.

In this section, we have optimized the transient of chosen modes in order to reduce the vibration outside the location of the focused vibration. The solution found was to accelerate the transient of four modes still with an exponential profile. By this way, we guarantee that a finger located outside the target zone would not be affected by unwanted vibrations. This work pave the way to the psychophysical evaluation of the device.

5.2 Psychophysical assessment of vibration synthesis

5.2.1 Scope of the study

The idea is to evaluate the effect of the velocity field on a multi-fingers interaction by contrast with a located interaction with a single finger as in [36]. The point is that, at this stage, the rise time of the two lowest frequencies modes are prominent as can be seen from the spectrogram of fig. 5.7. Thus, using one finger to explore the beam one detects everywhere brief impulses at the frequency of the repetition of the focusing evocating tiny shocks.

By contrast, the effect is striking when two fingers or more are in contact with the vibrating surface. In this case, the vibrating sensation ceases in the finger in contact

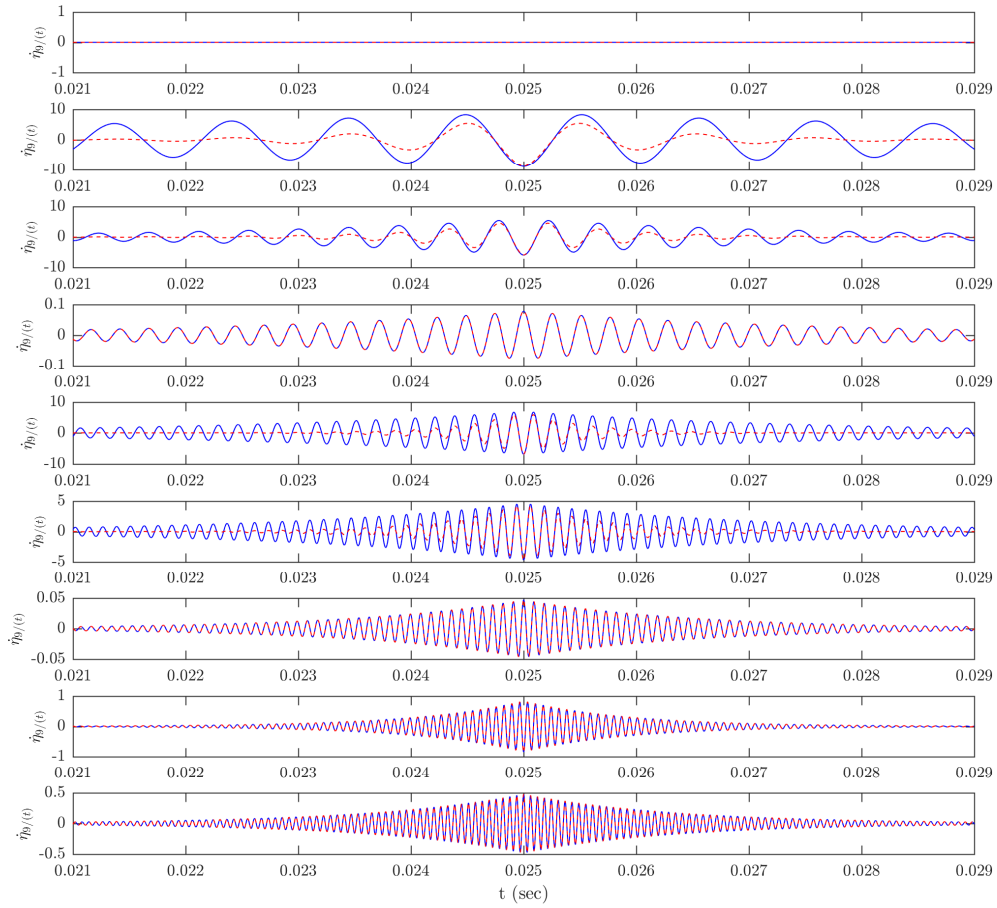

FIGURE 5.6: Comparing modal beneficent of for both normal excitation (blue) and accelerated excitation (red dashed)

with the lowest level of velocity, while the second finger still detects the so-called repeated "shocks". To confirm this, the following experiment was set.

5.2.2 Prototype; Beam with Free-Free Boundary Condition

An aluminium beam of $100 \times 6\ mm^2$ and $2\ mm$ of thickness with free-free condition was manufactured [83]. Six piezoelectric actuators have been laminated below of the beam as it is seen in Fig. 5.8. A modal test has been conducted and the modal parameter and

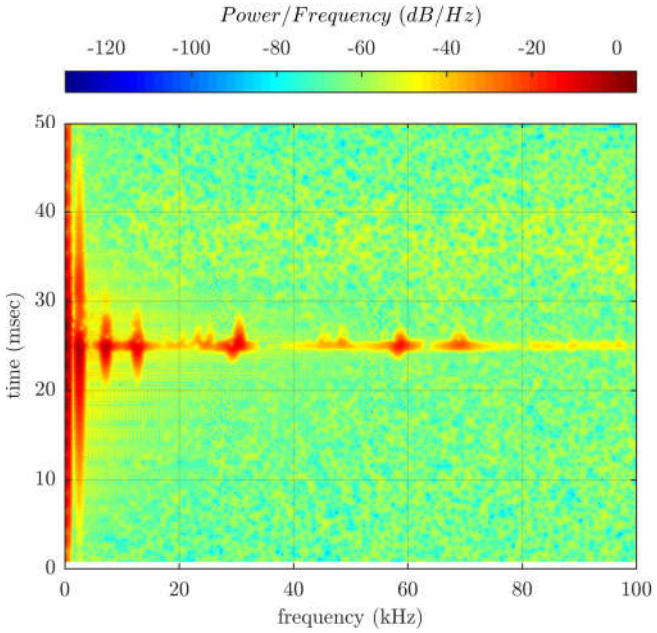

FIGURE 5.7: Sprectrogram of the vibration velocity at the center during a focusing. We see that the two lowest mode prominent from 0 to 50 ms.

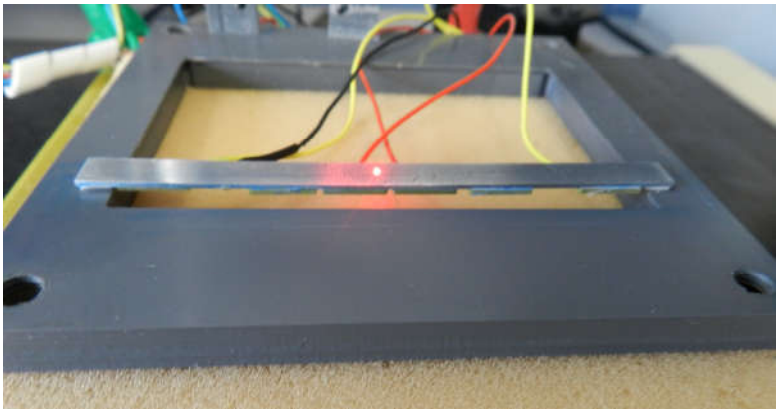

FIGURE 5.8: Prototype of aluminium beam with free-free boundary condition

mode shapes of beam have been identified between $100Hz - 100kHz$. The table of the modelled modal parameters and mode shapes of this beam is presented in Appendix B.

We use trapezoidal pulse in the center of the beam, as a tactile stimulation which is the wanted vibration form. As a result, the objective vibration field is defined as black mesh in Fig. 5.9. The modal approximation of this reference spatial form using modelled modes is shown in Fig. 5.9.

After determining the excitation voltage signals of the actuators, the beam has been excited and a cartography has been done. The experimentally measured vibration field at the time $t = T_F$ is depicted in Fig. 5.10. The experimental measured vibration field

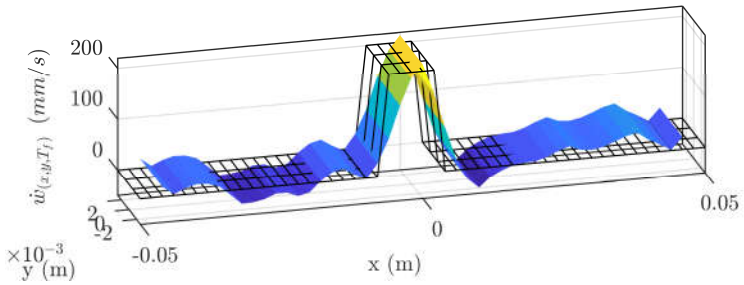

FIGURE 5.9: Reference spatial deformation of beam (black mesh grid) and its modal approximated form using modes —- to — (colored surf)

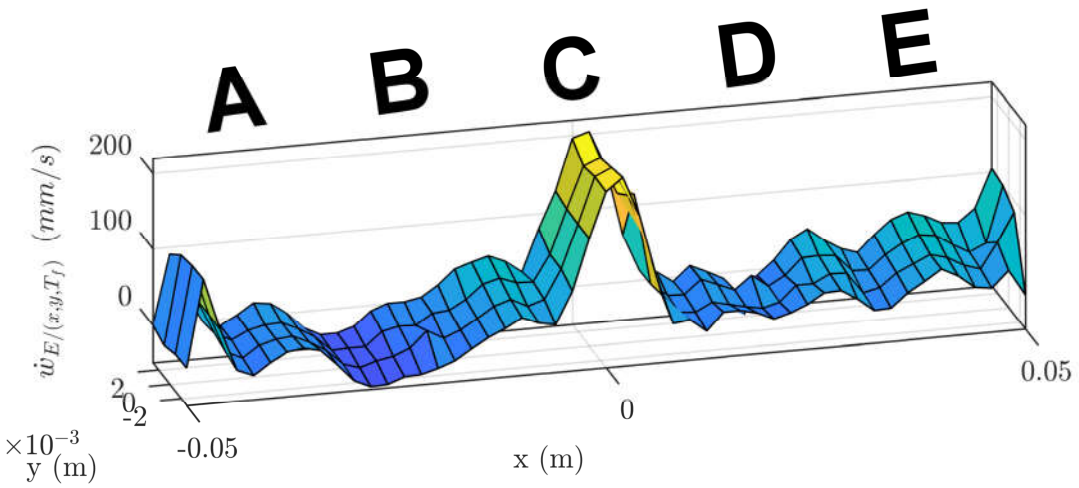

FIGURE 5.10: Experimental carthography of spatial form generation in $t = T_F$

is a good approximation of the expected spatial vibration

5.2.3 Protocol

The surface of the beam has been divided into five equal zones, named 'A', 'B', 'C', 'D' and 'E' as shown in Fig. 5.12. During the psychophysical test, the users were asked to use two fingers simultaneously, each of them being located on two different zones without moving. The combination imposed were (A,C), (B,D) and (C,E) (in the latter they will be denoted respectively I, II, III), in order to reduce the mechanical cross talk between two fingers. The users were asked to test one of the combination randomly, while the voltage were set to obtain various maximum speeds $80\,\mathrm{mm\,s^{-1}}$, $100\,\mathrm{mm\,s^{-1}}$, $150\,\mathrm{mm\,s^{-1}}$ and $200\,\mathrm{mm\,s^{-1}}$ in random order. The stimuli for a given setting and location were repeated at a frequency of 7 Hz. For each run, the participants were asked to locate where they detected an event. The answers were categorized as "right", "left" or "both".

Ten participants, 3 women and 7 men aged between 22 and 38 years old, have repeated

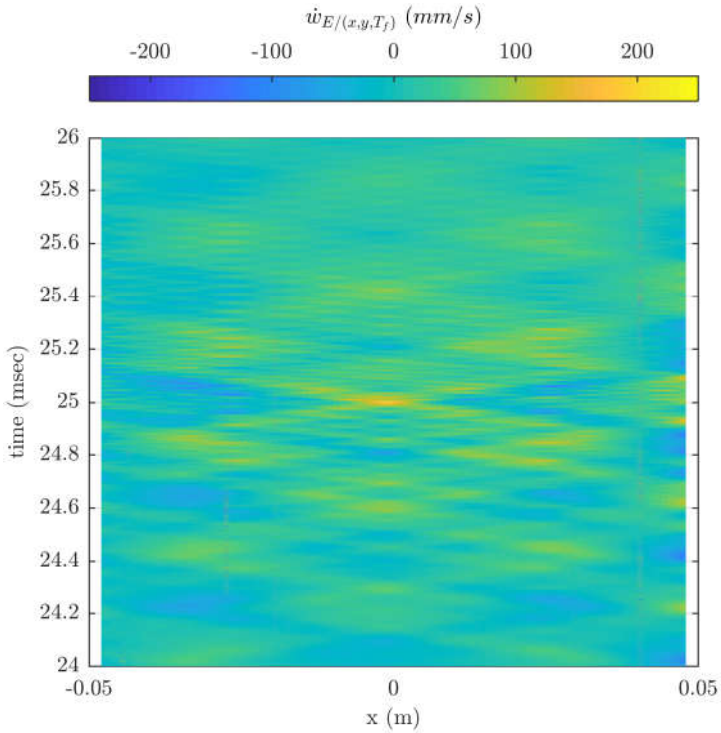

FIGURE 5.11: spatio-temporal evolution near the focusing time. Vertically : time from 24 ms to 26 ms (expected focusing time is 25 ms), horizontally : position along the central line of beam.

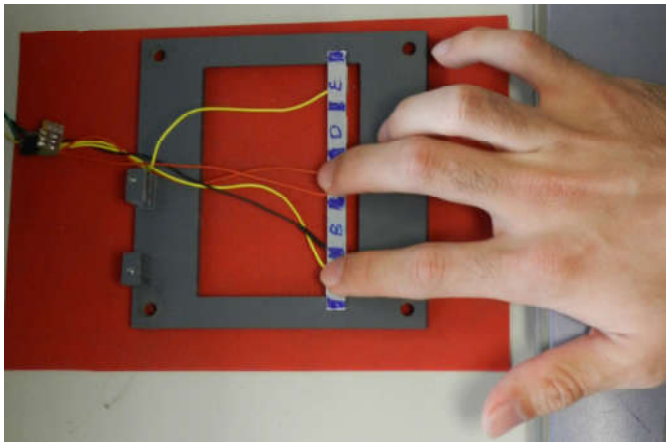

FIGURE 5.12: The scheme of beam which is divided to five spots of ('A', 'B', 'C', 'D' and 'E'), the participant is touching spot 'A' by index finger and spot 'C' by middle finger in photo.

this procedure for two sets of psychophysical experiments. In one experiment, the participants were asked to put index and middle finger of one hand on the sets of locations (A,C), (B,D) and (C,E) and compare the sensations under the index and middle fingers of the same hand (test 1). In the second experiment, participants put the index fingers of both hands simultaneously on the same sets of location and answered the same question (test 2).

5.2.4 Results and discussion

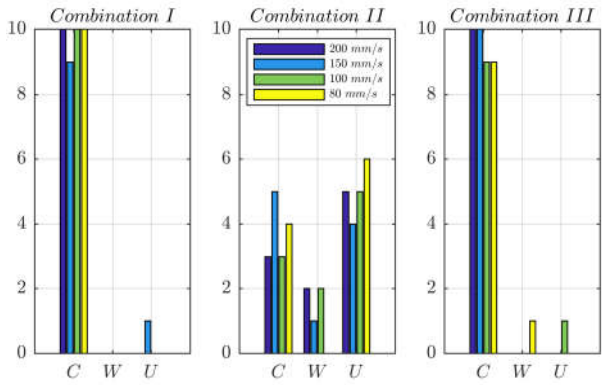

FIGURE 5.13: The perception results of index and middle fingers of ten participants, left subplot is comparison of (A,C) spots, center subplot is for (B,D) and right subplot is comparison (C,E) spots. 'C' represents Correct response, 'W' represents Wrong response and 'U' is Undetermined response.

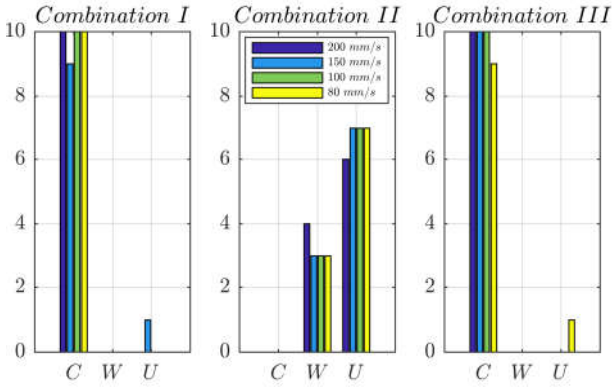

FIGURE 5.14: The perception results of right hand index and left hand index fingers of ten participants, left subplot is comparison of (A,C) spots, center subplot is for (B,D) and right subplot is comparison (C,E) spots. 'C' represents Correct response, 'W' represents Wrong response and 'U' is Undetermined response.

During the tests, if the location of the focusing is correctly detected, a right handed user should feel it on the middle finger for combination I, and on the index in configuration III. In configuration II, as the focusing will be between the two fingers, the answer is likely to be undetermined. Of course, a left handed users will be reversed. Therefore, to cover all the cases, we classified the answers as 'correct', 'wrong' and 'undetermined'. Fig. 5.13 sums up the result of test 1. In this figure, the answer for one location (as shown in Fig. 5.12) and various maximum speed at localization are summed up. The 'C', 'W' and 'U' stand for 'correct', 'wrong' and 'undetermined'. It clearly shows that, as expected, the participants dominantly detected that the focusing is located at 'C' near the center regardless of the vibration amplitude. They declared to have no feeling on the finger where the velocity field is smaller. Only one participant had a similar feeling

under the two fingers at $150\,\mathrm{mm\,s^{-1}}$. For the configuration III Fig. 5.13 illustrates that the participants correctly locate the focusing point in a similar proportion, that is in almost any case. Again, only one participant could not differentiate the sensation, and one answer was wrong. This happened for the lowest velocity levels $80\,\mathrm{mm\,s^{-1}}$ and $100\,\mathrm{mm\,s^{-1}}$.

For location II, the velocities are fairly equal under each finger, although it is slightly larger in zone 'B' due to some discrepancies in the boundary conditions imposed by the tape. Therefore we consider answers in favor of 'B' as correct. Some participants felt a stronger vibration on the spot 'B', while only one chose 'D' (considered as wrong). Actually, most participants concluded that both fingers were stimulated which explains the majority of 'B & D' (classified as undetermined).

In fact, although the velocity in 'C' (fig. 5.10) dominates, looking at the temporal evolution of the vibration on Fig. 5.11 shows that during transient spots 'B' and 'C' (located in the vicinity of $-0.025\,\mathrm{m}$ and $0.025\,\mathrm{m}$ on the horizontal 'x' axis) present symmetrical speed extrema before and after the focusing (roughly at 24.8 ms and 25.2 ms) although the amplitudes represent roughly half of the central speed at focusing. That is the whole focusing process influences the haptic feeling experience of the users. Actually, it seems that the user "filters out" the vibration as if, in the process, the dominant speed was the only one perceived. Indeed, the 'A & C' and 'C & E' combination present the highest speed contrast, as opposed to 'B & D' where the speeds are almost equal. In the two first cases, the participants decide for the correct location, while for the last they cannot decide, and actually describe the experience as "shocks between the fingers". The second experience was designed to confirm that this ability to feel only the dominant side was not induced by some mechanical coupling induced by the hand : if the whole hand is vibrated at the lowest vibration amplitude, it makes sense that we feel only the difference of speed. Hence, a similar psychophysical experiment was repeated by the participants using both index as it is very unlikely that the path between the hands through the body can propagate the vibration. The results are repeated and follow the pattern observed in the previous test (depicted in Fig. 5.14). This suggests that this differentiation of the speed, and the tendency to obliterate the feeling on the finger subjected to the lowest velocity is confirmed, and not due to the hand itself.

5.3 Conclusion

In this chapter, we studied the capability of the modal projection to focus the vibration at specific location in order to realize haptic stimulation. For that purpose, we first optimized the modal amplitude profile in order to avoid unwanted vibrations. Then, we conducted a psychophysical study on a specific device. According to the psychophysical experiment results, the participants experience a differentiated haptic stimulation when using two fingers of the same hand or two different hands. Moreover, they can localize correctly the peak of the velocity field at the center of beam ('C' spot). The first observations indicate that the sensation results from the difference of the vibration speed under each finger so that only the finger exposed to the largest amplitude feels the stimulation.

Conclusions

Results

This work has studied the feasibility of a new focusing technic for tactile haptic interactions. The approach proposed is to use elastic wave, which can be implemented easily on an existing screen for instance. Typically, piezoelectric ceramics are used because they can easily be glued in dead zone of the screen a technic which has already been extensively tested in many research works, and especially in the group, to realize friction modulation devices.
Such devices use a standing wave, a mode shape that is excited at or near resonance, to take advantage of the amplification and thus limit the voltage to be applied. The screen is entirely vibrating, so the user can experience the friction reduction on the whole display. In some cases however, a differentiated stimuli in desired, in order to convey different information at different location, for instance in the scenario of several users collaborating on a screen.
Focusing technics such as time reversal and phased array have been successfully applied in this field but they have some shortcoming as explained in the first chapter. The approach that was investigated is different in order to address:

- The control over the focusing pattern and its location;
- the robustness;
- The transient.

The idea proposed in this work is to take advantage of the property of the resonance and their associated mode shapes. This approach has already been applied in the thesis of Sofiane Ghenna, to realize travelling waves in a finite beam. The principle was to combine two specific mode shapes which resonant frequencies were close to the working frequency of two Langevin resonator. A control strategy was proposed to impose both the amplitude and their relative phase, in order to obtain the resulting traveling wave and minimize the standing wave. This result proved that modes could be separately controlled.

In Chapter 2, the dynamic of elastic media have been presented in a simple case to explain the background needed for this work. The orthogonality of the mode shapes is the main result that is used throughout because it provides a method to specify a velocity field. The mode shapes are indeed a basis for the kinematically acceptable shapes of the elastic structure, so, in a manner similar to Fourier transform, it can be described by its modal coordinates –the amplitude of each mode involved to realize the shape– and therefore, the spatial dependence of the problem can be eliminated.
The theory supposes that a infinite number of mode shapes are superimposed. In practice, the number of mode must be limited. To address, this a distortion criterion is proposed in order to select the relevant modes. The method is used in this application only to fix the so-called desired shape, namely a contrasted velocity field that must be obtained at a given time, named focusing time.
Hence, the next step is to specify the transients for each mode that have been selected. Since, the goal of this work is to verify that the method was suited for the application, the voltages to be applied in open loop must be calculated. The issue here is to excite several modes simultaneously while limiting the voltage to the values that the ceramics can withstand. Therefore, the approach proposed is for each mode to modulate a transient envelop at its resonant frequency, in order to limit cross talk between neighbouring modes, a frequency criterion is explained for the transient. In the case of several ceramics, a procedure to optimize the voltage dispatching amongst them is also presented.

The strategy suppose to have a good knowledge of modes : their shapes and their dynamic parameters. Therefore, chapter 3 is dealing with the identification procedure that was used throughout the thesis. The difficulty here is that a large number of modes must be identified. A simple method of peak picking in the frequency domain is implemented. The method is known to be fairly usable as long as the modes are lightly damped and

with well separated resonant frequencies. This assumption is verified for most of the mode of the test geometries. Tests have demonstrated this point, and to recover the orthogonality condition that can be lost due to measurement errors and the spatial sampling a re-orthogonalization procedure has been proposed and validated.

The fourth chapter has presented an experimental study on a more realistic structure. The identification procedure has been applied, and a modal basis was built following the procedure. The methodology has then been tested on a velocity field with limited spatial spectrum. Various test regarding the control of the focus width, the location, and the rise time of different modes have been performed. The results are convincing, and it was observed that the focusing is satisfactory despite the open loop operation which is difficult to apply for high frequency modes.
Various velocity fields have been realized on an example requiring a large number of modes. High frequency modes have shorter wavelength, and plate modes become prominent, so the modeling errors resulting from the unperfect identification are larger, but they can be handled thanks to the re-orthogonalization.
The control of modes transient to enhance the focusing time was also validated in this part.

The transient of vibration has been studied for the purpose of haptic interaction in the chapter 2. The problem of local vibration on non-targeted zone and its perturbation on haptic perception has been discussed. A solution has been proposed by acting on the dynamic of modes and accelerating the mode excitation. A set of psychophysics test has been performed on the a haptic display developed based on the thesis principle. The psychophysics evolutions confirms the perceivability of generated spatial deformation in multi-touch interaction of the users. This means that when users touch the haptic display with two fingers, they can distinguish the zones of haptic display with higher amplitude of the vibration velocity.

Outlook

The work presented in this thesis is a proof of concept, and obviously there are many issues that remain to be solved.

- **identification:** The identification is currently done offline. The main drawback of this if that the resonant frequencies are sensitive to environmental factors such as temperature. Even if this can be handled by the control, a fair knowledge is required for the algorithms at start-up. Accordingly, there is a need for an online identification of the resonance. The mode shapes are more stable but still a preliminary procedure such as the one used in this work is not practical. Future works would be on an on-line –or at least automated– modal shape calibration, using the reversibility of the piezoelectric ceramics and either an simplified embedded or an external structural model.

- **control:** the modal decomposition reduces the problem of the control of the whole structure to the control of the modal coordinates with respect to time. The difficulty here is to follow time varying references because the problem is to control the transient. Currently, it has been established that the control of individual modes vibration is possible, but here the synchronized control of several modes is required. A hierarchical structure is thus probably necessary. At a high level the control must generate the references and synchronize low level controllers that only address the transient control of individual modes. The planning of the references is a difficult problem because the velocity field must remain beneath a pattern before the focusing to avoid parasitic stimuli.

- **haptic:** So far the interaction between the stimuli and the focusing remains blurry. In this work for instance the choice to impose a velocity field is based on the result of some authors that have identify the mechanical impedance of the finger and concluded that it is similar to a damper. However, this work addressed sinusoidal vibrations, and the validity for transient remains uncertain. Therefore, there is a critical need for a better knowledge of the relevant factors that influence the detection by the finger. Only then some guidelines to plan the trajectories can be defined.

Appendix A

The Modal parameters of Rython beam

The Modal parameters of Rython beam;

A.1 dynamic parameter

Mode N.	f_S kHz	f_E kHz	Damping	Gain (mm/(sV))
1	0.32			0
2	1.27	1.29	210.67 $\times 10^{-}3$	0.9
3	2.82	2.77	144.14 $\times 10^{-}3$	0.13
4	4.92	4.76	94.44 $\times 10^{-}3$	0.32
5	7.49	7.19	83.39 $\times 10^{-}3$	0.65
6	10.47	10.02	124.69 $\times 10^{-}3$	1.05
7	13.8	13.11	134.73 $\times 10^{-}3$	2.1
8	17.4	16.62	60.15 $\times 10^{-}3$	1.65
9	21.23	19.98	54.69 $\times 10^{-}3$	1.9
10	25.22	23.79	81.97 $\times 10^{-}3$	1.32
11	29.35	27.57	63.47 $\times 10^{-}3$	0.84
12	33.57	32.06	67.06 $\times 10^{-}3$	0.36
13	37.84	36.17	33.17 $\times 10^{-}3$	0.57
14	42.14	41.04	75.54 $\times 10^{-}3$	1.8
15	46.47	45.95	59.84 $\times 10^{-}3$	3.4
16	50.82	50.97	34.33 $\times 10^{-}3$	3.5
17	55.2	56.02	84.78 $\times 10^{-}3$	3.3
18	59.62	61.31	58.72 $\times 10^{-}3$	3.95
19	64.1	66.54	69.88 $\times 10^{-}3$	4.1
20	68.65	72.22	77.54 $\times 10^{-}3$	5.5
21	73.26	77.4	147.29 $\times 10^{-}3$	4.2
22	77.93	82.79	108.71 $\times 10^{-}3$	3.9
23	82.64	87.2	92.89 $\times 10^{-}3$	3.4
24	87.39	94.4	118.11 $\times 10^{-}3$	4.57
25	92.15	100.19	94.81 $\times 10^{-}3$	6.2
26	96.92	104.33	86.26 $\times 10^{-}3$	4.5
27	101.67	110.18	68.07 $\times 10^{-}3$	4
28	106.39	115.47	69.28 $\times 10^{-}3$	3.9
29	111.03	126.49	126.49 $\times 10^{-}3$	1.69
30	115.52	130.14	99.89 $\times 10^{-}3$	3
31	119.48	136.46	190.52 $\times 10^{-}3$	4.9

A.2 Mode shapes

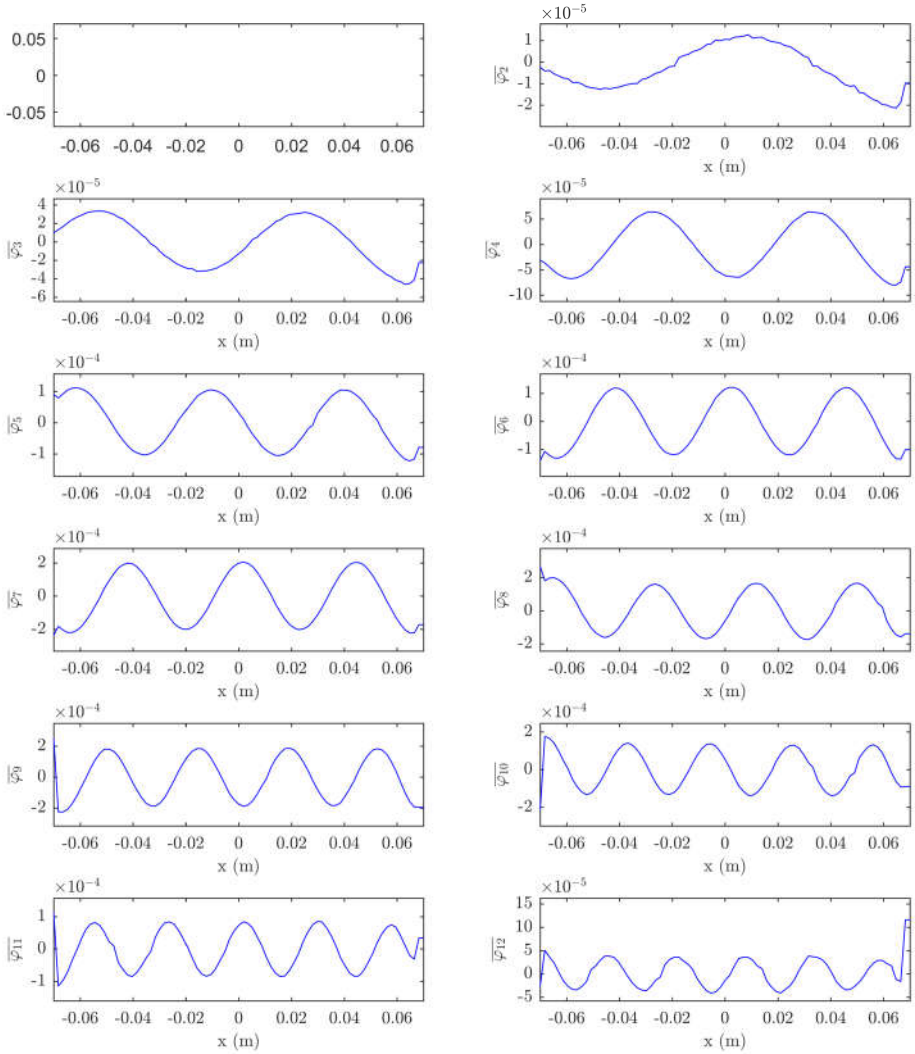

FIGURE A.1: Mode shape of Rython beam obtained by identification

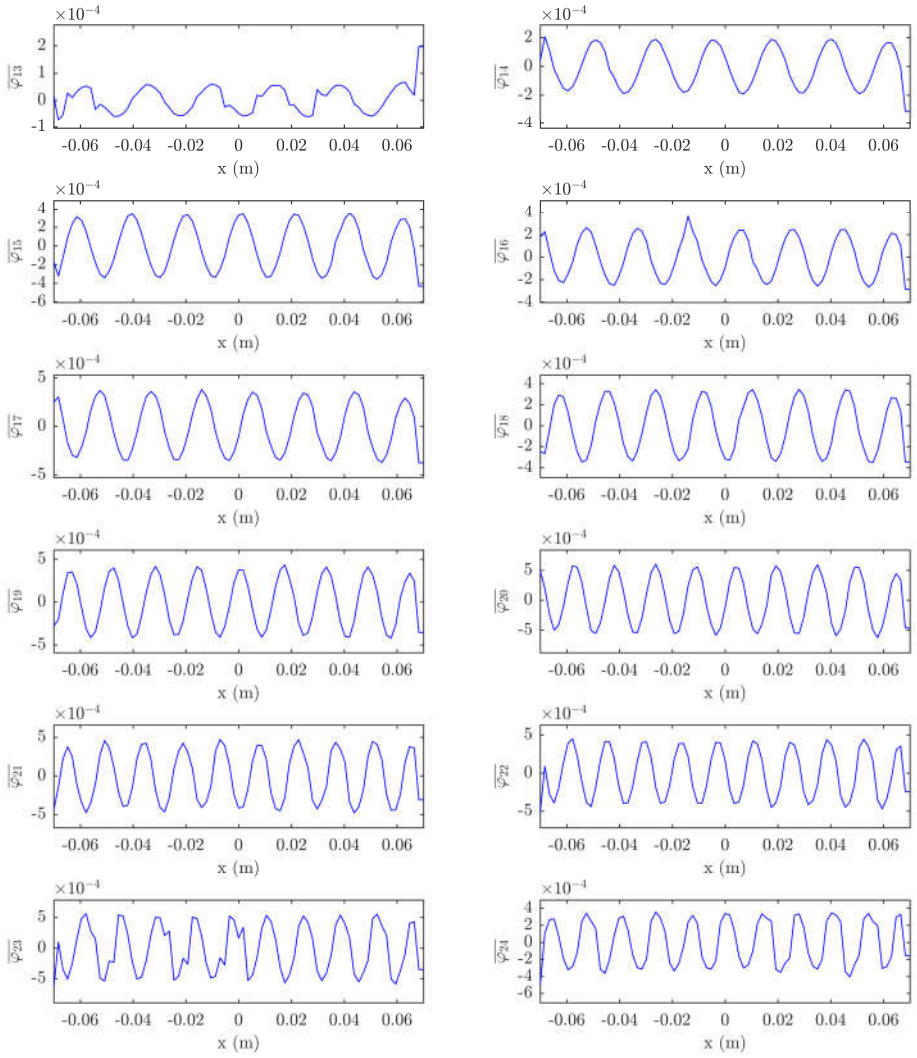

FIGURE A.2: Mode shape of Rython beam obtained by identification

Appendix B

The Modal parameters of Aluminum beam

The Modal parameters of Aluminium beam with free-free boundary condition;

B.1 dynamic parameter

TABLE B.1: Identified modal parameters

Mode	$f_k\ (Hz)$	ξ_k	$G_k(mm/(sV))$
$\overline{\varphi}_1$	229	0.0437	+114
$\overline{\varphi}_3$	2553	0.0165	+654
$\overline{\varphi}_5$	7137	0.0265	+6500
$\overline{\varphi}_7$	12701	0.0168	-8346
$\overline{\varphi}_9$	22810	0.0112	+10414
$\overline{\varphi}_{11}$	29390	0.0166	-6285
$\overline{\varphi}_{13}$	58303	0.0101	-41448
$\overline{\varphi}_{15}$	68543	0.0176	-166030
$\overline{\varphi}_{17}$	87855	0.0147	+134615

B.2 Mode shapes

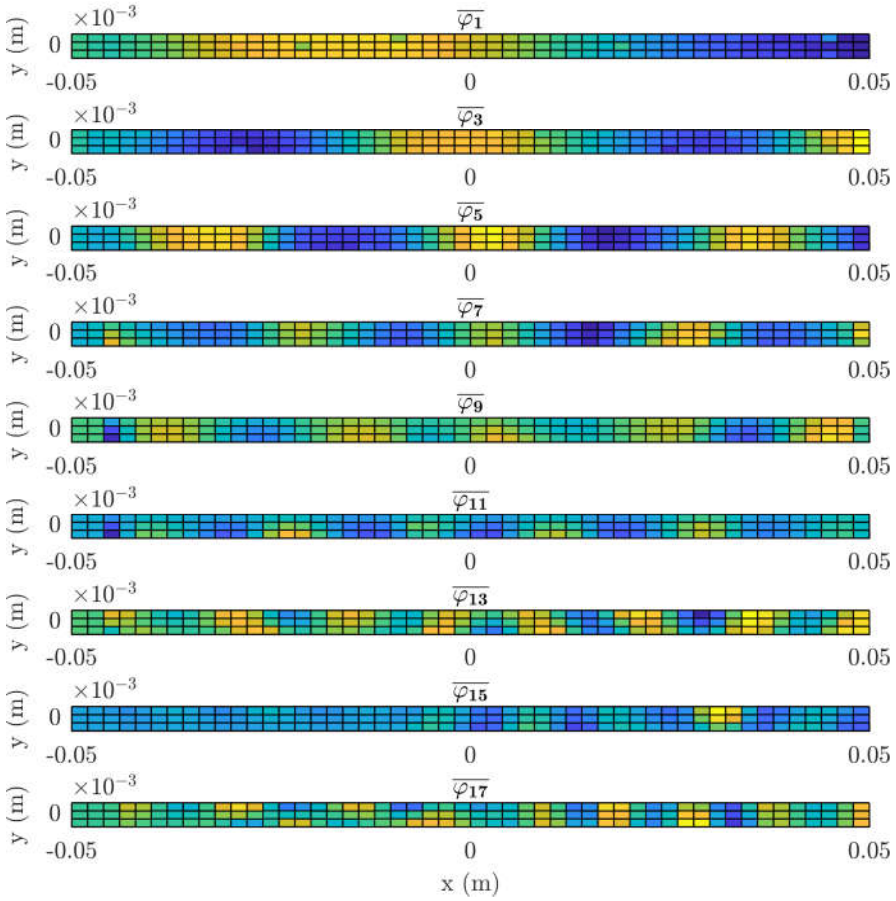

FIGURE B.1: Identified mode shapes ($\varphi_k(x, y)$) for nine modelled modes of beam.

Bibliography

[1] El Saddik. The Potential of Haptics Technologies. *IEEE Instrumentation Measurement Magazine*, 10(1):10–17, February 2007.

[2] M. A. Srinivasan and R. Zimmer. Machine Haptics. In Larry R. Squire, editor, *Encyclopedia of Neuroscience*, pages 589–595. Academic Press, Oxford, 2009.

[3] M. Sreelakshmi and T.D. Subash. Haptic technology: A comprehensive review on its applications and future prospects. *Materials Today: Proceedings*, 4(2, Part B):4182 – 4187, 2017. International Conference on Computing, Communication, Nanophotonics, Nanoscience, Nanomaterials and Nanotechnology.

[4] T. Hermann and J. G. Neuhoff A. Hunt, editors. *The Sonification Handbook*. Logos Publishing House, Berlin, 2011.

[5] R. S. Dahiya, G. Metta, M. Valle, and G. Sandini. Tactile sensingfrom humans to humanoids. *IEEE Transactions on Robotics*, 26(1):1–20, Feb 2010.

[6] Kenneth O Johnson. The roles and functions of cutaneous mechanoreceptors. *Current Opinion in Neurobiology*, 11(4):455–461, August 2001.

[7] *(Merkel Cells*, (accessed 2018/07/18). https://en.wikipedia.org/wiki/Merkel_cell.

[8] F. J. Looft. Response of monkey glabrous skin mechanoreceptors to random noise sequences: III. Spectral analysis. *Somatosensory & Motor Research*, 13(3-4):235–244, 1996.

[9] *Ruffini Corpuscles*, (accessed 2018/07/18). https://en.wikipedia.org/wiki/Bulbous_corpuscle.

[10] *Meissner Corpuscle*, (accessed 2018/07/18). https://en.wikipedia.org/wiki/Tactile_corpuscle.

[11] *Pacinian corpuscles*, (accessed 2018/07/18). https://en.wikipedia.org/wiki/Lamellar_corpuscle.

[12] Hiroki Ishizuka and Norihisa Miki. MEMS-based tactile displays. *Displays*, 37:25–32, April 2015.

[13] Hiroki Ishizuka and Norihisa Miki. Mems-based tactile displays. *Displays*, 37:25 – 32, 2015. Advanced MEMS technologies and Displays.

[14] V. G. Chouvardas, A. N. Miliou, and M. K. Hatalis. Tactile displays: Overview and recent advances. *Displays*, 29(3):185–194, July 2008.

[15] S. Choi and K. J. Kuchenbecker. Vibrotactile display: Perception, technology, and applications. *Proceedings of the IEEE*, 101(9):2093–2104, Sept 2013.

[16] M. Wiertlewski, J. Lozada, and V. Hayward. The Spatial Spectrum of Tangential Skin Displacement Can Encode Tactual Texture. *IEEE Transactions on Robotics*, 27(3):461–472, June 2011.

[17] T. Watanabe and S. Fukui. A method for controlling tactile sensation of surface roughness using ultrasonic vibration. In *, 1995 IEEE International Conference on Robotics and Automation, 1995. Proceedings*, volume 1, pages 1134–1139 vol.1, May 1995.

[18] M. Biet, F. Giraud, and B. Lemaire-Semail. Squeeze film effect for the design of an ultrasonic tactile plate. *IEEE Transactions on Ultrasonics, Ferroelectrics, and Frequency Control*, 54(12):2678–2688, December 2007.

[19] Michel Amberg, Frédéric Giraud, Betty Semail, Paolo Olivo, Géry Casiez, and Nicolas Roussel. STIMTAC: A Tactile Input Device with Programmable Friction. In *Proceedings of the 24th Annual ACM Symposium Adjunct on User Interface Software and Technology*, UIST '11 Adjunct, pages 7–8, New York, NY, USA, 2011. ACM.

[20] E. Vezzoli, W. Ben Messaoud, M. Amberg, F. Giraud, B. Lemaire-Semail, and M.-A. Bueno. Physical and Perceptual Independence of Ultrasonic Vibration and Electrovibration for Friction Modulation. *IEEE Transactions on Haptics*, 8(2):235–239, April 2015.

[21] S. GHENNA, E. Vezzoli, C. Giraud-Audine, F. Giraud, M. Amberg, and B. Lemaire-Semail. Enhancing variable friction tactile display using an ultrasonic travelling wave. PP(99):1–1.

[22] S. Ghenna, F. Giraud, C. Giraud-Audine, M. Amberg, and B. Lemaire-Semail. Preliminary design of a multi-touch ultrasonic tactile stimulator. In *2015 IEEE World Haptics Conference (WHC)*, pages 31–36.

[23] L. Santos-Carreras, K. Leuenberger, P. Retornaz, R. Gassert, and H. Bleuler. Design and psychophysical evaluation of a tactile pulse display for teleoperated artery palpation. In *2010 IEEE/RSJ International Conference on Intelligent Robots and Systems (IROS)*, pages 5060–5066, Oct 2010.

[24] R. Vitushinsky, Sam Schmitz, and A. Ludwig. Bistable Thin-Film Shape Memory Actuators for Applications in Tactile Displays. *Journal of Microelectromechanical Systems*, 18(1):186–194, February 2009.

[25] M. Tomozawa, K. Okutsu, Hee Young Kim, and Shuichi Miyazaki. Characterization of High-Speed Microactuator Utilizing Shape Memory Alloy Thin Films. *Materials Science Forum*, 475-479:2037–2042, January 2005.

[26] Hyung Seok Lee, Hoa Phung, Dong-Hyuk Lee, Ui Kyum Kim, Canh Toan Nguyen, Hyungpil Moon, Ja Choon Koo, Jae-do Nam, and Hyouk Ryeol Choi. Design analysis and fabrication of arrayed tactile display based on dielectric elastomer actuator. *Sensors and Actuators A: Physical*, 205:191–198, January 2014.

[27] Hoa Phung, Canh Toan Nguyen, Tien Dat Nguyen, Choonghan Lee, Uikyum Kim, Donghyouk Lee, Jae-do Nam, Hyungpil Moon, Ja Choon Koo, and Hyouk Ryeol Choi. Tactile display with rigid coupling based on soft actuator. *Meccanica*, 50(11):2825–2837, October 2015.

[28] Jeremy Streque, Abdelkrim Talbi, Philippe Pernod, and Vladimir Preobrazhensky. Electromagnetic Actuation Based on MEMS Technology for Tactile Display. pages 437–446. Springer Berlin Heidelberg, June 2008.

[29] J. Streque, A. Talbi, P. Pernod, and V. Preobrazhensky. New Magnetic Microactuator Design Based on PDMS Elastomer and MEMS Technologies for Tactile Display. *IEEE Transactions on Haptics*, 3(2):88–97, April 2010.

[30] T. Hoshi, M. Takahashi, T. Iwamoto, and H. Shinoda. Noncontact Tactile Display Based on Radiation Pressure of Airborne Ultrasound. *IEEE Transactions on Haptics*, 3(3):155–165, July 2010.

[31] K. Hasegawa and H. Shinoda. Aerial display of vibrotactile sensation with high spatial-temporal resolution using large-aperture airborne ultrasound phased array. In *2013 World Haptics Conference (WHC)*, pages 31–36, April 2013.

[32] Tom Carter, Sue Ann Seah, Benjamin Long, Bruce Drinkwater, and Sriram Subramanian. Ultrahaptics: Multi-point mid-air haptic feedback for touch surfaces. In *Proceedings of the 26th Annual ACM Symposium on User Interface Software and Technology*, UIST '13, pages 505–514, New York, NY, USA, 2013. ACM.

[33] L. R. Gavrilov and E. M. Tsirulnikov. Mechanisms of stimulation effects of focused ultrasound on neural structures: Role of nonlinear effects. 2003.

[34] L. R. Gavrilov and E. M. Tsirulnikov. Focused ultrasound as a tool to input sensory information to humans (review). *Acoustical Physics*, 58(1):1–21, Jan 2012.

[35] Jung-Han Woo and Jeong-Guon Ih. Vibration rendering on a thin plate with actuator array at the periphery. *Journal of Sound and Vibration*, 349:150–162, 2015.

[36] C. Hudin, J. Lozada, and V. Hayward. Localized Tactile Feedback on a Transparent Surface through Time-Reversal Wave Focusing. *IEEE Transactions on Haptics*, 8(2):188–198, April 2015.

[37] Charles Hudin and Sabrina Paneels. Localisation of vibrotactile stimuli with spatio-temporal inverse filtering. Pise, Itanly, June 2018-08. Eurohaptics international conference on haptics and touch enabled computer applications.

[38] S.-H. Chen, Z.-D. Wang, and X.-H. Liu. Active vibration control and suppression for intelligent structures. *Journal of Sound and Vibration*, 200(2):167 – 177, 1997.

[39] Daniel J. Inman. Active modal control for smart structures. *Philosophical Transactions of the Royal Society of London A: Mathematical, Physical and Engineering Sciences*, 359(1778):205–219, January 2001.

[40] Zheng-Hua Qian and Sohichi Hirose. Theoretical validation on the existence of two transverse surface waves in piezoelectric/elastic layered structures. *Ultrasonics*, 52(3):442–446, March 2012.

[41] M. Abu-Hilal. Forced vibration of eulerbernoulli beams by means of dynamic green functions. *Journal of Sound and Vibration*, 267(2):191 – 207, 2003.

[42] R. G. Curtis and M. Redwood. Transverse surface waves on a piezoelectric material carrying a metal layer of finite thickness. *Journal of Applied Physics*, 44(5):2002–2007, May 1973.

[43] J.D. ACHENBACH. Chapter 2 - the linearized theory of elasticity. In J.D. ACHENBACH, editor, *Wave Propagation in Elastic Solids*, North-Holland Series in Applied Mathematics and Mechanics, pages 46 – 78. Elsevier, Amsterdam, 1975.

[44] A. Labuschagne, N.F.J. van Rensburg, and A.J. van der Merwe. Comparison of linear beam theories. *Mathematical and Computer Modelling*, 49(1):20 – 30, 2009.

[45] K. F. Graff. *Wave motion in elastic solids.* Dover Publications, New York, 1975.

[46] Peter Hagedorn and Anirvan DasGupta. *Vibrations of Beams*, pages 113–178. John Wiley & Sons, Ltd, 2007.

[47] C. Richard Johnson. Adaptive Modal Control of Large Flexible Spacecraft. *Journal of Guidance, Control, and Dynamics*, 3(4):369–375, 1980.

[48] Francesco Braghin, Simone Cinquemani, and Ferruccio Resta. A new approach to the synthesis of modal control laws in active structural vibration control. *Journal of Vibration and Control*, January 2012.

[49] Y. A. KHULIEF. Vibration suppression in using active modal control. *Journal of Sound and Vibration*, 242(4):681–699, May 2001.

[50] S. Hurlebaus, U. Stobener, and L. Gaul. Vibration reduction of curved panels by active modal control. *Computers & Structures*, 86(3):251–257, 2008.

[51] Xavier Falourd, Herve Lissek, and Pierre-Jean Rene. Active low-frequency modal noise cancellation for room acoustics: an experimental study. *Proceedings of the 16th International Congress on Sound and Vibration*, 2009.

[52] Francesco Braghin, Simone Cinquemani, and Ferruccio Resta. Vibrations control in cruise ships using magnetostrictive actuators. In Tom Proulx, editor, *Structural Dynamics, Volume 3*, Conference Proceedings of the Society for Experimental Mechanics Series, pages 1207–1214. Springer New York, 2011. DOI: 10.1007/978-1-4419-9834-7_106.

[53] H. Rosenbrock. Distinctive problems of process control. *Chemical Enginnering Progress*, 58:43–50, 1962.

[54] B. Porter and R. Crossley. *Modal control theory and applications.* Taylor and Francis, London 1972.

[55] Uwe Stbener and Lothar Gaul. Modal vibration control for PVDF coated plates. *Journal of Intelligent Material Systems and Structures*, 11(4):283–293, 2000.

[56] B Ni and C Hu. Dynamics of the mindlin plate and its modal vibration control. *Journal of Vibration and Control*, 18(13):2039–2049, 2012.

[57] H Tjahyadi, F He, and K Sammut. Multi-mode vibration control of a flexible cantilever beam using adaptive resonant control. *Smart Materials and Structures*, 15(2):270, 2006.

[58] D. J. Ewins. *Modal Testing: Theory, Practice and Application.* Reserach Studies Press LtD, Baldock, Herfordshire, England, 2000.

[59] W. Heylen, S. Lammens, and P. Sas. *Modal analysis theory and testing.* Katholieke Universiteit Leuven, Faculty of Engineering, Belgium, 1998.

[60] Eva A. Czajkowski, Raphael T. Haftka, and Andre Preumont. Spillover stabilization of large space structures. *Journal of Guidance, Control, and Dynamics*, 13(6):1000–1007, 1990.

[61] G. R. Skidmore and W. L. Hallauer. Modal-space active damping of a beam-cable structure: theory and experiment. *Journal of Sound and Vibration*, 101(2):149–160, July 1985.

[62] Björn Richter, Jens Twiefel, and Jörg Wallaschek. *Piezoelectric Equivalent Circuit Models*, pages 107–128. Springer US, Boston, MA, 2009.

[63] Yaowen Yang and Lihua Tang. Equivalent circuit modeling of piezoelectric energy harvesters. *Journal of Intelligent Material Systems and Structures*, 20(18):2223–2235, 2009.

[64] C. Nadal and F. Pigache. Multimodal electromechanical model of piezoelectric transformers by hamilton's principle. *IEEE Transactions on Ultrasonics, Ferroelectrics, and Frequency Control*, 56(11):2530–2543, November 2009.

[65] S.R. Ibrahim. Random decrement technique for modal identification of structures. *Journal of Spacecraft and Rockets*, 14(11):696–700, 1977.

[66] A. Malekjafarian, R. Brincker, M.R. Ashory, and M.M. Khatibi. *Topics on the Dynamics of Civil Structures*, volume 1, chapter Modified Ibrahim Time Domain Method for Identification of Closely Spaced Modes: Experimental Results, pages 443–449. Springer New York, New York, 2012.

[67] Edwin Reynders, Mattias Schevenels, and Guido De Roeck. *MACEC: A MATLAB Toolbox for Experimental and Operational Modal Analysis*, 2014.

[68] W.R. Smith. Least squares time-domain methods for simultaneous identification of vibration parameters from multiple free-response records. *22nd Structures, Structural Dynamics and Materials Conference, Structures, Structural Dynamics, and Materials*, pages 194–201, April 1981.

[69] R. S. JUANG, J.-N.and PAPPA. An eigensystem realization algorithm for modal parameter identification and model reduction. *Journal of Guidance, Control, and Dynamics*, 8(5):620–627, 1985.

[70] R.S. Pappa, K.B. Elliott, and A Schenk. Consistent-mode indicator for the eigensystem realization algorithm. *Journal of Guidance, Control, and Dynamics*, 16(7):852–858, 1993.

[71] T. Zhao-qian and Q. Yang. Modal analysis using the time series analysis method (ar or arma model) and its computer program design. page 559565, Orlando, Florida, Feb 1984. 2nd International Modal Analysis Conference (IMAC).

[72] D. Bonnecase, M. Prevosto, and A. Benveniste. Application of a multidimensional arma model to modal analysis under natural excitation. pages 382–388, Kissimmee, Florida, Feb 1994. 8th International Modal Analysis Conference.

[73] E. Giorcelli, A. Fasana, Garibaldi, L, and A. Riva. Modal analysis and system identifcation using armav models. page 676680, Honolulu,Hawaii, Jan 31Feb 3 1994. 12th International Modal Analysis Conference (IMAC).

[74] L. Ljung. *System Identifcation, theory for the user*. Prentice-Hall, Inc, 1987.

[75] J.P. Norton. *An introduction to Identifcation*. Academic Press, 1986.

[76] G.C. Carne, J.P. Lauffer, and A.J Gomez. Modal testing of a very exible 110m wind turbine structure. International Modal Analysis Conference (IMAC), 1988.

[77] L. HERMANS and H. VAN DER AUWERAER. Modal testing and analysis of structures under operational conditions: Industrial applications. *Mechanical Systems and Signal Processing*, 13(2):193 – 216, 1999.

[78] B. PEETERS and C.E. VENTURA. Comparative study of modal analysis techniques for bridge dynamic characteristics. *Mechanical Systems and Signal Processing*, 17(5):965 – 988, 2003.

[79] CJ. Wilson and DB Bogy. An experimental modal analysis technique for miniature structures. *ASME Journal of Vibration and Acoustics*, 118(1):1–9, 1996.

[80] Goege Dennis. Fast identification and characterization of nonlinearities in experimental modal analysis of large aircraft. *Journal of Aircraft*, 44(2):399–409, 2007.

[81] D. L. Brown, R. J. Allemang, Ray Zimmerman, and M. Mergeay. Parameter estimation techniques for modal analysis. *SAE Transactions*, 88:828–846, 1979.

[82] B.J. Dobson. A straight-line technique for extracting modal properties from frequency response data. *Mechanical Systems and Signal Processing*, 1(1):29 – 40, 1987.

[83] E. Enferad, C. Giraud-Audine, F. Giraud, M. Amberg, and B. Lemaire-Semail. Differentiated haptic stimulation by modal synthesis of vibration field. In *2018 IEEE Haptics Symposium (HAPTICS)*, pages 216–221, March 2018.